Nanofabrication and Engineering of Gene Delivery Vectors

Emma Charlotte Claire Butterworth

Submitted to the Department of Engineering, Queen Mary University of London in partial fulfilment of the requirements for the degree of Doctor of Philosophy

I, Emma Charlotte Claire Butterworth, confirm that the research included within this thesis is my own work or that where it has been carried out in collaboration with, or supported by others, that this is duly acknowledged below and my contribution indicated. Previously published material is also acknowledged below.

I attest that I have exercised reasonable care to ensure that the work is original, and does not to the best of my knowledge break any UK law, infringe any third party's copyright or other Intellectual Property Right, or contain any confidential material.

I accept that the College has the right to use plagiarism detection software to check the electronic version of the thesis.

I confirm that this thesis has not been previously submitted for the award of a degree by this or any other university.

Signature:

Date: 29/11/18

Abstract

Coaxial electrospray is an encapsulation method in use in biomedical research for the encapsulation of drugs and genes. In this thesis, its ability to produce polymer capsules with a core-shell structure was investigated as potential non-viral vector for gene delivery. Three main aspects were considered. 1) The shell polymer was varied between a homopolymer and block copolymer to compare their ability to condense the inner polymer and so produce a smaller particle. 2) DNA is expensive and not cost-effective to use in the large quantities required here. Therefore two different polymers (carboxymethyl cellulose and hyaluronic acid, referred to as CMC and HA respectively) were used for the inner polymer and as potential cost-effective models for DNA due to their similar structures – long-chain polymers with a negative charge. 3) Electrosprayed particles were characterised and compared with bulk-assembled complexes to assess differences in size, structure and zeta potential. For electrospray to be considered as a good method, it must produce particles with characteristics that are at least as good as complexes produced through self-assembly.

It was seen that electrospray was able to produce particles of a similar size to bulk-assembled complexes (110 nm and 106 nm respectively) and core-shell structures were seen with all particles and complexes. The main differences were seen with zeta potential. Complexes using the block copolymer decreased the zeta potential to a large degree, but this decrease was not seen with electrosprayed particles suggesting a difference in shell structure. Particles and complexes containing hyaluronic acid were seen to be less stable than those containing CMC as they underwent aggregation in aqueous phase.

Finally it was seen that the particles produced by electrospray were relatively soft as they underwent deformation when sprayed onto hard substrates.

Acknowledgements

The first thanks must go to my supervisors Professor John Stark and Doctor Julien Gautrot, without whom none of this would have been possible. Your support and advice have been invaluable over the last four years.

Next to my friends and colleagues at QMUL! Thanks for all the delicious lunches and dinners! Special thanks to Hui for keeping me company in the somewhat empty lab during the first year.

Thanks as well to the technicians who helped me over the course of the PhD. Roger Nelson, Russell Bailey and Vicente Araullo-Peters who were always happy to lend a hand.

And finally thank you to my family for supporting me always.

List of Figures and Tables

Figures

in grey, pH 11 in yellow) shown with the spectra of the solid individual polymers for comparison (PDMAEMA light blue, CMC dark blue). In all three cases, the peak around 1600 cm-1 (carbonyl of CMC) can be seen signifying the presence of CMC.

Figure 4.7 Comparison across a range of pH for bulk-assembled complexes showing a) mean peak height and b) mean diameter obtained via AFM (shown with standard error) (n= 27, 43 and 24 for pH 5, 7 and 11 respectively)

Figure 4.8 a) FTIR spectra comparison of identifiable peaks from electrosprayed particles (inner flow rate 0.2mL/h, outer flow rate 0.1 mL/h) and bulk-assembled complexes of CMC-PDMAEMA with a polymer weight ratio of 1:5 (CMC:PDMAEMA) in both cases, b) corresponding ratios to the 1730 cm-1 peak, c) comparison of FTIR spectra from bulk-assembled CMC-PDMAEMA complexes in various ratios (denoted in brackets), and d) calibration curve of ratios of 1365 cm-1 to 1730 cm-1 peak relative to CMC percentage.

Figure 4.9 Comparison of the mean diameter, obtained through AFM, of bulk-assembled complexes (BA, n=54) and electrosprayed CMC-PDMAEMA particles (ES, n=78) (shown with standard error)

Figure 4.10 Comparison between the mean zeta potential of CMC-PDMAEMA electrosprayed particles (ES) and bulk-assembled complexes (BA) (shown with standard deviation)

Figure 4.11 TEM images a) & b) show examples of bulk-assembled complexes of CMC-PDMAEMA, c) & d) show electrosprayed CMC-PDMAEMA particles. The dark spots are assumed to be aggregations of silver which were used to stain the CMC to give a greater contrast with respect to neutral or cationic phases such as PDMAEMA. The outlines of outer shells are highlighted in e) & f).

Figure 5.1 AFM data from electrosprayed CMC-PDMAEMA particles. AFM images using a) Mw 90,000 CMC at 100 µg/mL, b) Mw 90,000 CMC at 100 ng/mL, c) Mw 250,000 at 100 ng/mL, and comparison of mean particles sizes with d) using different molecular weights of CMC (Mw 250,000, n = 96 and Mw 90,000, n = 112) at 100 µg/mL and e) Mw 90,000 CMC at different concentrations (100 µg/mL, n = 78 and 100 ng/mL, n = 112) (shown with standard error). In both d) and e), * indicates a significant difference between the two conditions for $p<0.05$ (unpaired t-test).

Figure 5.2 Comparison of FTIR spectra of single electrosprayed PDMAEMA and PLA-PDMAEMA

Figure 5.3 FTIR spectra of coaxially electrosprayed CMC-PLA-PDMAEMA particles compared with the single electrospray individual polymers (all samples vacuum-dried)

Figure 5.4 AFM images of electrosprayed a) CMC-PDMAEMA particles, b) CMC-PLA-PDMAEMA particles, c) a comparison of the mean peak heights of CMC-PDMAEMA and CMC-PLA-PDMAEMA and d) a comparison of lateral diameter with a correction factor given by Yang et al.22. For c), * indicates significant difference for $p<0.05$ (unpaired t-test). Both c) & d) are shown with standard error.

Figure 5.5 Zeta potential comparison of electrosprayed (blue) and self-assembled (orange) CMC-PDMAEMA and CMC-PLA-PDMAEMA particles (shown with standard deviation)

Figure 5.6 FTIR spectra comparison of solid HA and single electrosprayed HA showing the emergence of additional peaks following the electrospray process which may be due to protonation

Figure 5.7 FTIR spectra of electrosprayed HA-PDMAEMA compared with single electrosprayed PDMAEMA and HA

Figure 5.8 FTIR spectra of electrosprayed HA-PLA-PDMAEMA compared with single electrosprayed PLA-PDMAEMA and HA

Figure 5.9 AFM images of electrosprayed particles a) CMC-PDMAEMA, b) CMC-PLA-PDMAEMA, c) HA-PDMAEMA, d) HA-PLA-PDMAEMA, and a comparison of mean peak heights obtained via AFM (HA-PDMAEMA n = 291, HA-PLA-PDMAEMA n = 170, CMC-PDMAEMA n = 78, CMC-PLA-PDMAEMA n = 81) (shown with standard error). * indicates a significant difference for $p<0.05$ (unpaired t-test).

Figure 5.10 A comparison of zeta potential across different polymer combinations prepared with electrospray (blue) and self-assembly (orange) (shown with standard deviation)

Figure 5.11 TEM images of bulk-assembled complexes a) CMC-PDMAEMA, b) CMC-PLA-PDMAEMA, c) HA-PDMAEMA and d) HA-PLA-PDMAEMA

Figure 5.12 TEM images of electrosprayed particles a) CMC- PDMAEMA, b) CMC-PLA-PDMAEMA, c) HA-PDMAEMA and d) HA-PLA-PDMAEMA

Tables

Nomenclature

AFM	atomic force microscopy
ALA	5-aminovulinic acid
ATR	attenuated total reflectance
CA4	combretastatin A4
CDDP	cisplatin
CMC	carboxymethyl cellulose
DC-Chol	3β-[N-(N',N'-dimethylaminoethane)-carbamoyl] cholesterol
DI H2O	deionised water
DLS	dynamic light scattering
DMAc	dimethylacetamide
DMF	dimethylformamide
DOX	doxorubicin
EE 100-55	Eudragit L 100-55
Egg PC	egg phosphatidylcholine
ERS	Eudragit RS
FTIR	Fourier transform infrared spectroscopy
GF	griseofulvin
GFP	green fluorescent protein
HA	sodium hyaluronate
HCl	hydrochloric acid
ID	inner diameter
L-100	Eudragit L-100
NaCl	sodium chloride
NaOH	sodium hydroxide

OD	outer diameter
PAA	poly(acrylic acid)
PAM	poly(acrylamide)
PMAA	poly(methylacrylic acid)
PBS	phosphate buffer solution
PCL	polycaprolactone
PdI	polydispersity index
PDLLA	poly-DL-lactic acid
PDMAEMA	poly(2-dimethylamino-ethylmethacrylate)
pDNA	plasmid DNA
PEG	polyethylene glycol
PEI	polyethylenimine
PFA	perfluoroalkoxy alkane
pKa	acid dissociation constant
PLA	poly(lactic acid)
PLGA	poly(lactic-c-glycolic acid)
PS	polystyrene
PTFE	polytetrafluoroethylene
PVP	polyvinylpyrrolidone
SEAP	secreted alkaline phosphate
SEM	scanning electron microscopy
siRNA	silencing RNA
TEM	transmission electron microscopy
THF	tetrahydrofuran

Q_0	characteristic flow rate

d_0	characteristic jet diameter
q	charge
I	current
ρ	density
r	distance form cone apex
R	droplet radius
φ	electric potential in spherical coordinates
E_n	electric stress from the field normal to the cone surface
K	electrical conductivity
t_e	electrical relaxation time
Q	flow rate
g	gravity
h	height
δ	inverse of dimensionless flow rate
d_j	jet diameter
φ_{ent}	polymer fraction at chain entanglement
$\varphi_{ch.ov}$	polymer fraction at chain overlap
φ_{ray}	polymer fraction at Raleigh limit
p	pressure
ε_r	relative permittivity
α	semi-angle of cone
γ	surface tension
E_s	tangential electric field on the jet surface
ε_0	vacuum permittivity
μ	viscosity

δ_μ viscous dimensionless parameter

V voltage

Contents

Chapter One

Introduction

1.1 Biomedical Applications of Electrospray

Electrospray has many applications such as an ionization source for mass spectrometry[1], colloid thrusters for use in spacecraft propulsion[2], nanoscale particle deposition[3]. In the biomedical field there is current ongoing research into its ability to produce monodisperse capsules for drug and gene delivery systems[4]. The main attractive features are the ability to produce monodisperse particles[5] and size control based on known electrospray scaling laws[6]. Monodispersity allows for better control of drug or gene dosage volume and a predictable release profile[7], and size is important as the optimum size for efficient cell uptake can vary between cells[8-10].

Another advantage of electrospray is the ability to use organic solvents with delicate therapeutic molecules. For example with coaxial electrospray, where two liquid are electrosprayed simultaneously, if one liquid contains the organic solvent and the other the therapeutic molecule, the exposure of the therapeutic molecule to the solvent is limited and so damage is prevented[11].

Although the throughput of electrospray may be low when producing particles on the nanoscale, the system can be upscaled by using an array of needles rather than a single needle[12, 13]. Overall this makes electrospray a relatively easy, one-step method

for producing drug and gene delivery systems. In the case of gene delivery, it is particularly attractive as a means of producing a non-viral delivery vector[14-16].

1.2 Thesis Aim

The aim of this thesis is to look at the use of coaxial electrospray as a method of preparing core-shell particles for a gene delivery system. This was done by comparing various characteristics of complexes produced through bulk-assembly with particles produced through electrospray.

Additionally two different polymers were compared for the shell and a further two for the core. For the shell polymers, a homopolymer and block copolymer were compared to see their different effects on particle size and structure. For the core polymers, two different long-chain polymers were compared to assess their suitability as a cost-effective model for DNA.

1.3 Thesis Structure

Chapter Two contains a literature review comprised of two sections. The first gives an overview of electrospray including the current understanding of single electrospray scaling laws and their applicability to coaxial electrospray; the effect of solvents and polymers on electrosprayed particle formation and coaxial electrospray liquid combinations. The second section looks at current DNA delivery systems used in research; describes various non-viral self-assembly systems and previous research into electrosprayed DNA vectors.

Chapter Three introduces the experimental methods used in this thesis. The first part looks at the decisions that went into designing the coaxial electrospray set-

up and describes the polymers and solvents used. The second part looks at the methods used to characterise the particles produced by electrospray.

Chapter Four characterises particles for their composition, size and zeta potential and compares them to particles produced by self-assembly, a commonly used method for creating delivery systems.

Chapter Five compares the use of a homopolymer and block copolymer for the particle shell; looks at the influence of different molecular weight of the core polymer; and compares the use of two different long-chain polymers (carboxymethyl cellulose and hyaluronic acid) as potential models for DNA.

Chapter Six presents the overall conclusions to the work in this thesis and directions for future work.

Chapter Two

Literature Review

2.1 Electrospray

2.1.1 Basic Mechanism

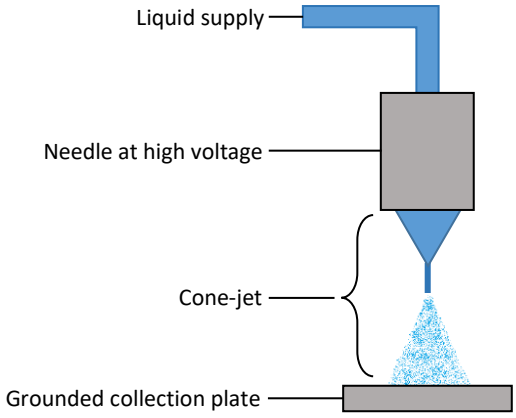

Figure 2.1 Basic electrospray set-up

Electrospray is a method by which an electrified liquid is sprayed through a needle and the resulting wet droplets or dry particles are collected. The liquid is charged by setting up an electric field between the needle and the collection plate, commonly achieved by applying high voltage directly to the needle and grounding the collection plate (Fig. 2.1). The liquid becomes charged as it passes through the needle, electrostatic repulsion overcomes the liquid's surface tension changing the emerging jet into a spray, which is attracted towards the grounded collection plate. In this set-up, an extractor is also often used to help accelerate the droplets from the spray down

towards the collection plate. This is necessary as the droplets all possess a like charge and so will scatter due to electrostatic repulsion.

2.1.2 Spray Modes

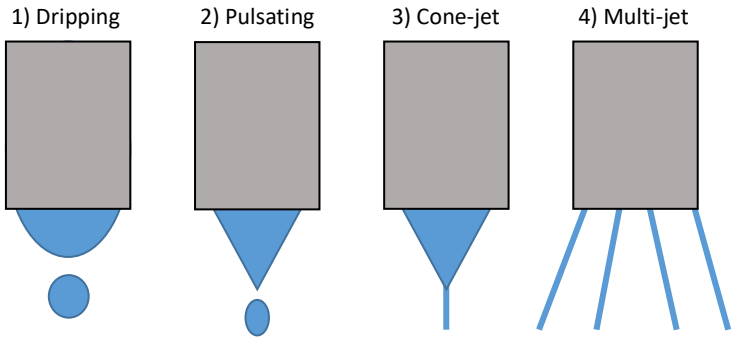

Figure 2.2 Spray modes as applied voltage increases

Depending on the voltage applied, different spray modes are observed (Fig. 2.2), and these can be classified as either dripping or spraying modes[17-19]. As the applied voltage increases, the main observed modes are as follows:

1) Dripping mode - The main forces at play are gravity and surface tension. When gravity overcomes surface tension, a droplet falls from the end of the needle to the collection plate.

2) Pulsation mode - This takes place over four phases: 1) accumulation of liquid, 2) cone formation, 3) liquid jet ejection, and 4) relaxation of the meniscus[20].

3) Cone-jet mode - The liquid meniscus forms a stable cone-shape (the Taylor cone) at the end of the needle and emits a steady jet which breaks up into a spray.

4) Multi-jet mode - Several jets are emitted from the meniscus.

2.1.3 Taylor Cone-jet Spray

When a liquid passes through an electrified needle, over a certain range of applied voltage the meniscus will form a stable, jet-emitting cone at the end of the needle[17]. This stable cone is known as the Taylor cone[21], and the cone-jet spray mode is considered the ideal mode for electrospray due to its stability.

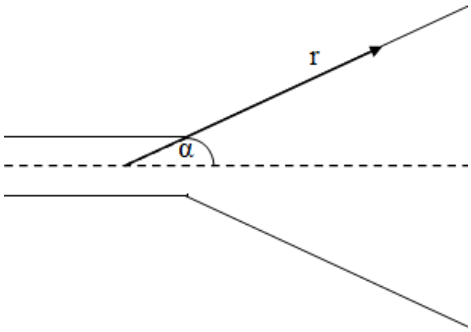

Figure 2.3 Cone-jet diagram, where r is the distance from the cone apex and α is the semi-angle of the cone

Excluding the region very close to the apex, the Taylor cone can be considered hydrostatic. The balance between surface tension (γ) and the electric stress from the field normal to the cone surface (E_n), is what gives the cone its stability[22]. The balance of forces on the surface of an equipotential cone can be described by

$$\frac{\gamma}{rtan\alpha} = \frac{1}{2}\varepsilon_0 E_n^2 \qquad (2.1)$$

where r is distance from the cone apex, α is the semi-angle of the cone (as seen in Fig. 2.3) and ε_0 is the vacuum permittivity.

In spherical coordinates, the electric potential φ is given as

$$\varphi = Ar^{1/2}P_{1/2}(\cos\vartheta) \tag{2.2}$$

where the constant A is

$$\mathrm{A} = \left(\frac{2\gamma}{\varepsilon_0 P'^2_{1/2}(-\cos\alpha)sin^2\alpha\ tan\alpha}\right)^{1/2} \tag{2.3}$$

$P_{1/2}$ is the Legendre function of the order of $1/2$ and $\vartheta = \pi - \alpha$. For the condition of the cone being equipotential, $P_{1/2}cos\vartheta = 0$ which gives α to be 49.29°, known as the Taylor angle[22] (Fig. 2.3).

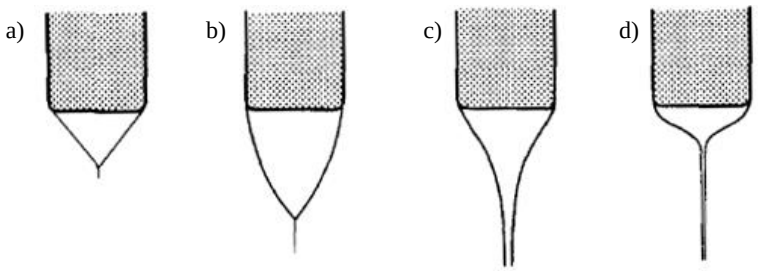

*Figure 2.4 Various possible meniscus shapes of cone-jet sprays: a) Taylor cone, b) meniscus curved away from cone axis, c) & d) meniscus curved towards cone axis. (Cloupeau, M. & Prunetfoch, B. J Electrostat **22**, 135-159 (1989)[17])*

However, the Taylor cone can be observed over a range of angles showing that there are in fact multiple solutions. This is explored by de la Mora[23] who expresses the difference between the surface tension and electric stress as pressure difference Δp, where Δp = 0 gives the 'perfect' Taylor cone, Δp < 0 gives a family of cones with the meniscus curved away from the cone axis, and Δp > 0 gives a family with the

meniscus curved towards the cone axis (Fig. 2.4). These different cone geometries were also observed by Cloupeau et al.[17]; menisci curving away from the cone axis were seen with high conductivity liquids (10^{-1} S/m), and menisci curving towards were seen with low conductivity liquids (10^{-9} S/m).

At the apex of the Taylor cone, the forces become unbalanced leading to the emission of a jet and this gives rise to the characteristic cone-jet spray mode.

2.1.4 Jet Break-up

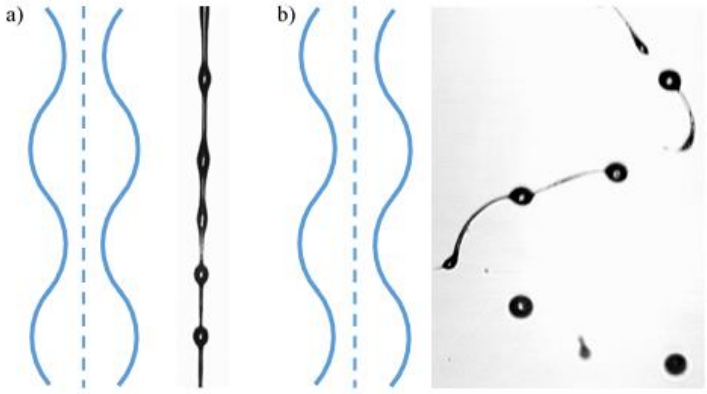

*Figure 2.5 a) axisymmetric instability and b) non-axisymmetric instability in an electrified jet (Adapted from Hartman, R.P.A., Brunner, D.J., Camelot, D.M.A., Marijnissen, J.C.M. & Scarlett, B. J Aerosol Sci **31**, 65-95 (2000)[24])*

There are two modes of jet instability (Fig. 2.5) which lead to jet break-up, axisymmetric (also known as varicose) and non-axisymmetric (also known as whipping or kink)[25] instability. In electrospray, the varicose instability dominates leading to droplet formation, whereas in electrospinning the kink instability dominates[26] leading to fibre production.

Hartman et al.[24] established three varicose break-up regimes: 1) a thread develops between each 'bulge', the lower bulge breaks off to form a droplet, and the thread retracts into the bulge above it, 2) the thread connecting two bulges breaks off at both ends and forms a small secondary droplet, and 3) a secondary droplet develops on the thread and a further thread develops between this secondary droplet and main droplet which then breaks off to form an even smaller droplet. The change between these regimes is related to the current which is in turn dependent on the flow rate. In order to keep a small size distribution, it is necessary to use as low a flow rate as possible in order to stay within the first varicose break-up regime and keep the number of secondary droplets to a minimum.

However, whipping break-up can also be seen in electrospray and this leads to an increase in the droplet size distribution. The tipping point between the two break-up modes is determined by the stress ratio of electric normal stress over the surface tension stress. Hartman et al.[24] showed through experimental data for a variety liquids that this occurs around 0.3. The stress ratio increases with the current through the cone and the current is itself dependent upon the flow rate. To avoid whipping break-up it is therefore necessary to keep to a low flow rate. Hartman et al.[27] also noted that for small diameter needles, the applied voltage had an effect on the current; a 1 mm diameter needle had a current 15% higher than for an 8 mm diameter needle for a cone of the same dimensions relative to the needle diameter. For keeping a low droplet size distribution, it is therefore important to use as low an applied voltage as possible i.e. the onset voltage.

2.1.5 Coulomb Fission

Lord Rayleigh calculated the maximum charge q at which a droplet of radius R can maintain a stable shape[28],

$$q^2 = 64\pi^2\varepsilon_0\gamma R^3 \quad (2.4)$$

where ε_0 = vacuum permittivity, and γ = surface tension. Following its formation through jet break-up, a droplet's radius will shrink due to evaporation as it travels. This decrease in radius causes an increase in surface charge which, when it exceeds the Rayleigh limit q, causes the droplet's shape to destabilise and jets are emitted which rid it of mass and excess charge before it returns once more to a stable shape.

2.2 Single Electrospray

Figure 2.6 Cone-jet mode of single electrospray

The physics of electrospray are complex owing to the many parameters involved and our understanding of their working is incomplete. For the single cone-jet mode (Fig. 2.6), scaling laws demonstrate the relation of current and jet diameter

to flow rate and present an extremely useful guide to controlling the size of droplets produced from the spray.

2.2.1 Current Scaling Laws

The current scaling laws all show current (*I*) as being dependent on a flow rate (*Q*) in the form $I \sim Q^x$, where the power index ranges from $^1/_4$ to $^1/_2$. Most laws also involve a constant that must be derived experimentally.

The earliest scaling law, derived by de la Mora & Loscertales[29], was dependent on flow rate and fluid properties (surface tension, conductivity and dielectric constant) and was very close to $Q^{1/2}$. However, Gañan-Calvo et al.[5] later derived two separate dependencies on flow rate. For liquids with high enough viscosity and conductivity, the scaling law is close to $Q^{1/2}$, but for liquids with low enough viscosity and conductivity it is closer to $Q^{1/4}$. The cut-off between 'high' and 'low' is determined by $\delta_\mu \delta^{1/3}$, where $\delta_\mu = \frac{\rho Q}{\mu d_0} = \left(\frac{\rho \varepsilon_0 \gamma^2}{K \mu^3}\right)^{1/3}$ is the viscous dimensionless parameter and $\delta = \frac{Q_0}{Q} = \frac{\gamma \varepsilon_0}{\rho K Q}$ is the inverse of the dimensionless flow rate (where μ is viscosity, ρ is density, and *K* is conductivity) and both d_0 and Q_0 are characteristics length scales found through the Π-theorem of dimensionless analysis, and are the characteristic jet diameter and flow rate respectively. Liquids with $\delta_\mu \delta^{1/3} \ll 1$ are high viscosity, and liquids with $\delta_\mu \delta^{1/3} \gg 1$ are low viscosity. Agreement with the low viscosity $Q^{1/4}$ scaling law was seen by Yao et al.[30], where the two liquids used both had a value of $\delta_\mu \delta^{1/3}$ much greater than 1.

2.2.2 Jet Diameter Scaling Laws

The jet diameter scaling law can be used to predict the diameter of a droplet formed immediately upon jet break-up[6]. De la Mora & Loscertales[29] found the jet diameter (d_j) scaled with a characteristic length r^*, which is itself proportional to $Q^{1/3}$.

$$d_j = G(\varepsilon) r^* \tag{2.5}$$

$$r^* = \left(\frac{Q\varepsilon\varepsilon_0}{K}\right)^{1/3} \tag{2.6}$$

When tested experimentally however, a variety of function $G(\varepsilon)$ are found[23]. One of the reasons suggested for this is in the way that d_j is measured. If d_j is found by measuring droplet diameter, any evaporation from the droplet before the measurement is taken will affect the diameter. If the jet itself is measured, then the diameter will vary as the jet is not a true cylinder but decreases in diameter as it extends from the Taylor cone[23]. Therefore the choice of where on the jet to measure the diameter will have an effect on $G(\varepsilon)$.

Gañan-Calvo et al.[31] proposed an alternative scaling law based upon the electrical potential decay within the region of transition from cone to jet (small relative to capillary diameter but large relative to jet radius), being of the same order as the kinetic energy flux. The electrical potential decay can be found through $I\Delta V$ where I is

$$I \sim K R^2 E_s \tag{2.7}$$

and ΔV (change in voltage) is

$$\Delta V \sim E_s L \tag{2.8}$$

where E_s (tangential electric field on the jet surface) is calculated from Taylor's solution.

$$E_s \sim \left(\frac{\sigma}{\varepsilon_0 L}\right)^{1/2} \tag{2.9}$$

Therefore, for a jet of radius R, the electrical potential decay is found to be

$$I\Delta V \sim \frac{\sigma}{\varepsilon_0} K R^2 \tag{2.10}$$

Putting this equal to kinetic energy flux $\rho U^2 Q$ (where the characteristic velocity $U \sim Q R^{-2}$) gives

$$R \sim \left(\frac{\rho Q^3 \varepsilon_0}{\sigma K}\right)^{1/6} \tag{2.11}$$

Comparison with published data showed strong agreement with droplet diameter scaling with R at a variety of flow rates both near and far from the minimum flow rate[31, 32]. A comparison was also made between the two competing scaling laws, looking at them in terms of the dimensionless droplet size and Weber number[31] (Fig. 2.7), where clear agreement can be seen with Gañan-Calvo's scaling law for cases where the Weber number is below 20.

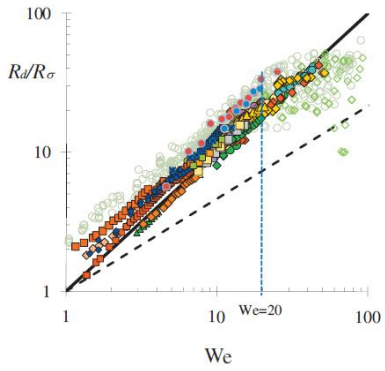

*Figure 2.7 Comparison of experimental data with dimensionless droplet size (R_d/R_σ) as a function of the Weber number. The solid black line represents Gañan-Calvo's scaling law ($R_d/R_\sigma = We$), and the dashed black line represents de la Mora's scaling law ($R_d/R_\sigma = We^{2/3}$). The vertical dotted line represents the limit of the scaling law. (Adapted from Gañan-Calvo, A.M. & Montanero, J.M. Physical Review E **79** (2009)[31])*

However, there is still recent data that does not agree with the Gañan-Calvo scaling law. Park et al.[33] examined electrospray of deionised water and saw good agreement with the de la Mora scaling law of $d_j = G(\varepsilon)r^*$, where $G(\varepsilon) = 0.88$.

2.2.3 Electrospray Parameters

2.2.3.1 Flow Rate

The flow rate is a commonly controlled parameter and, in the case of creating small diameter droplets, a low flow rate is desirable as it is related to jet diameter (seen in section 2.2.2). Chen & Pui[34] found KQ (where K is conductivity and Q is flow rate) to be related linearly to the emitted current, meaning that a higher conductivity allows for a lower flow rate.

The minimum flow rate is of particular interest as it is where droplets with the lowest size distribution will be generated. De la Mora & Loscertales[29] found the minimum flow rate relation $\eta_{min} = \left(\frac{\rho K Q_{min}}{\gamma \varepsilon_r \varepsilon_0}\right)^{1/2}$, where η_{min} is a dimensionless parameter of the order 1.

There have been a variety of other Q_{min} scaling laws derived for specific liquid conditions. Gañan-Calvo et al.[6] agreed with de la Mora's scaling law in the case of a liquid of low viscosity and high conductivity, but in situations where viscous forces stall the jet below Q_{min}, proposed that Q_{min} scales with Q_0/δ_μ. Additionally, Scheideler and Chen[35] put forward another scaling law for viscous liquids of low conductivity, Q_{min} scales with $\gamma D^2/\mu$ where D is the outer diameter of the nozzle. This is the first scaling law to take into account any characteristics of the needle.

2.2.3.2 Voltage

The appropriate applied voltage must be used in order to attain the stable cone-jet spray mode. The voltage at which a stable cone-jet is first established is known as the onset voltage. The cone-jet also displays hysteresis with regard to the voltage[17]. When increasing the voltage, the spray mode will change from dripping mode to cone-jet mode at V_1 and then to multi-jet mode at V_2. However, when decreasing the voltage, a stable cone-jet will still be present below V_1 and will change back to dripping mode at a lower voltage V_0.

The applied voltage can be negative or positive, which can be referred to as spraying in negative-mode or positive-mode respectively. It is easier to achieve a

stable spray in positive-mode than negative-mode as electric discharge from the needle-tip occurs at higher voltages more in the former than the latter[36].

2.2.3.3 Spray Current

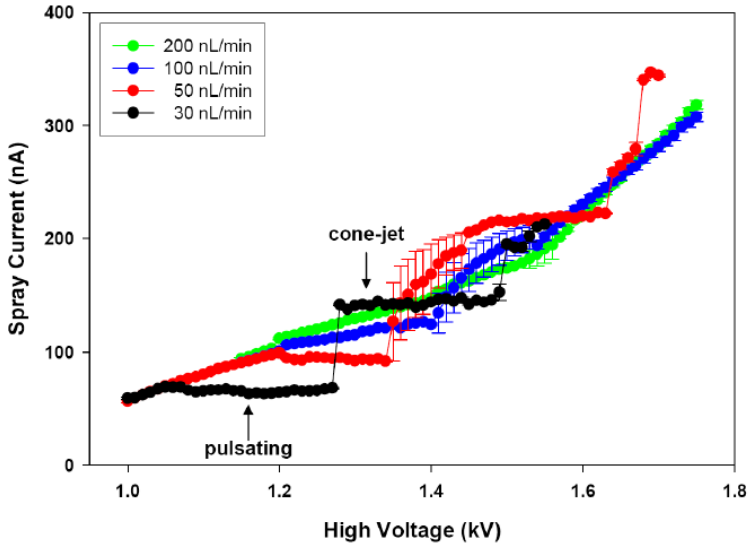

*Figure 2.8 Current collected by an electrode held 2mm from the needle tip. (Marginean, I., Kelly, R.T., Page, J.S., Tang, K. & Smith, R.D. Analytical Chemistry **79**, 8030-8036 (2007)[19])*

The spray current changes with spray mode and a jump in current can be seen between each mode (moving from dripping mode up to multi-jet mode)[19, 37]. As Fig. 2.8 shows, the jump between spray modes is more distinct at lower flow rates in the order of tens of nL/s. While the spray current cannot be controlled independently of other parameters, it gives information about whether the spray is in a stable regime, particularly at low flow rates.

2.3 Coaxial Electrospray

Figure 2.9 Cone-jet mode of coaxial electrospray

The concept of coaxial electrospray (Fig. 2.9) is the same as single electrospray, but uses concentric needles to produce a spray consisting of droplets with a core-shell structure, where most commonly the core is made up of the inner needle liquid and the shell is made up of the outer needle liquid. Alternatively, the inner liquid can swell and engulf the outer liquid. This approach was taken by Hwang et al.[38]. The liquid used in the inner needle was viscoelastic and it expanded as it exited the needle due to a phenomenon known as 'die stress'. When the flow rate of the inner liquid was greater than that of the outer liquid, this expansion was enough for the inner liquid to engulf the outer liquid completely and so droplets were produced with the inner needle liquid as the shell and the outer needle liquid as the core.

2.3.1 Driving Liquid Concept

Lopez-Herrera et al.[39] introduced the concepts of a 'driving liquid' and 'driving character' as a way of describing a situation where the current is carried wholly by the inner or outer liquid. When looking at a coaxial electrospray of ethylene glycol (inner liquid, EG) and Somos (outer liquid, a type of resin), it was seen that the

emitted current changed when the Somos flow rate was altered, and hardly at all when the EG flow rate was altered. Somos was referred to as the driving liquid, as the emitted current was entirely dependent on the Somos flow rate. The 'driving character' of a liquid was determined by seeing which of the two liquids had the lower electrical relaxation time $t_e = \frac{\varepsilon_r \varepsilon_0}{K}$. As can be seen, electrical relaxation time is dependent on a liquid's conductivity and therefore, in a given pair of liquids the driving character can be 'transferred' from one liquid to another by a sufficient increase in the conductivity of the non-driving liquid.

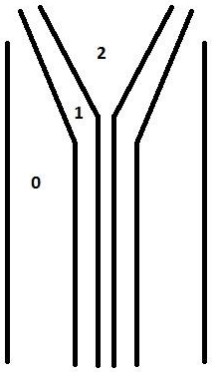

Figure 2.10 Diagram of the cone-jet spray where 0 indicates the medium the electrospray takes place in, 1 indicates the outer liquid and 2 indicates the inner liquid

The driving liquid affects the location of charges within the cone and jet. An outer driving liquid means the charges will be located on the surface between the outer liquid and the medium in which the electrospray takes place. With an inner driving liquid, the charges will be located on the surface between the two liquids. The location of charges has implications for the coaxial scaling laws given by Lopez-Herrera et al.[39], which is reflected in their use of the effective surface tension. When the outer liquid is the driving liquid, $\gamma_{eff} = \gamma_{01}$,where γ_{01} refers to the surface tension between

the outer liquid and the outer medium. In the case of the inner liquid being the driving liquid, when the outer liquid coating is sufficiently thin, the effective surface tension is $\gamma_{eff} = \gamma_{01} + \gamma_{12}$, where γ_{01} is as before, and γ_{12} refers to the surface tension between the outer and inner liquids (Fig. 2.10).

2.3.2 Current Scaling Law

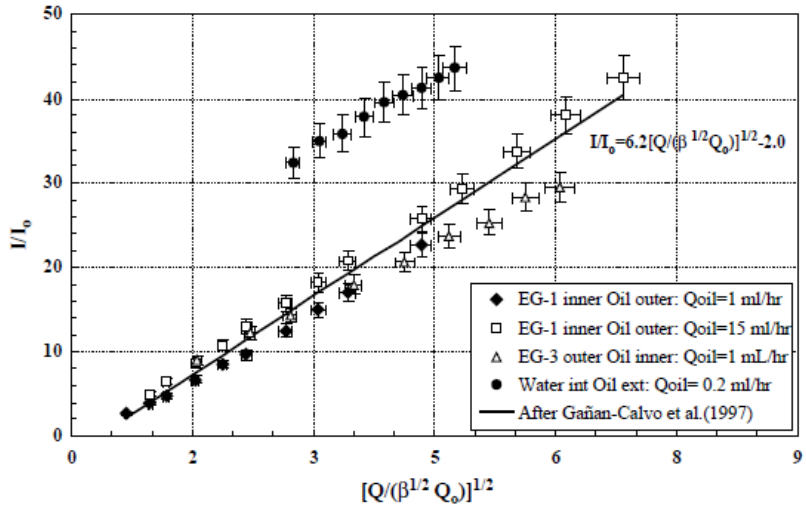

*Figure 2.11 Data obtained for coaxial electrospray compared to Gañan-Calvo's current scaling law. (Lopez-Herrera, J.M., Barrero, A., Lopez, A., Loscertales, I.G. & Marquez, M. J Aerosol Sci **34**, 535-552 (2003)[39])*

When looking at coaxial scaling laws, Lopez-Herrera et al.[39] used various combinations of EG, sunflower oil and water for coaxial electrospray with both inner and outer driving liquids and the data obtained was made dimensionless using the values given by Gañan-Calvo et al.[5] with the addition of β which represents the relative dielectric constant between the two liquids used (Fig. 2.11). Agreement was seen with the single electrospray scaling law which follows the power law $Q^{1/2}$.

However, as can be seen in Fig. 2.10, one set of data (inner driving liquid: deionised water, outer liquid: sunflower oil), while lying parallel to the $Q^{1/2}$ scaling law line, had significantly higher values than expected for the current. This discrepancy seems unrelated to the use of an inner driving liquid as the values found from another inner driven pair of liquids fall around the line of the scaling law. An explanation could not be given for this behaviour when using water, suggesting that it is perhaps related to the properties of deionised water. This indicates that there is still more work to be done on improving the understanding of the current scaling laws for coaxial electrospray for a great variety of liquids.

2.3.3 Jet Diameter Scaling Law

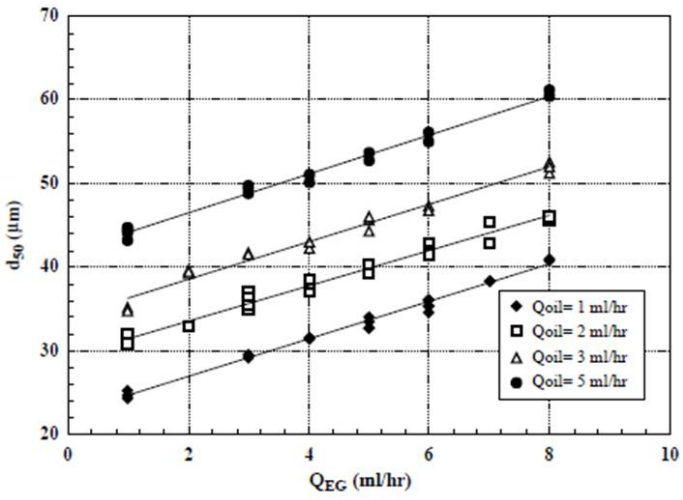

*Figure 2.12 Mean droplet diameter with an outer driving liquid EG with an inner liquid of sunflower oil (Lopez-Herrera, J.M., Barrero, A., Lopez, A., Loscertales, I.G. & Marquez, M. J Aerosol Sci **34**, 535-552 (2003)[39])*

For the jet diameter scaling law, in the outer driving liquid case it has been observed by Lopez-Herrera et al.[39] that when one flow rate is held constant and the

other altered, the droplet diameter increases linearly with flow rate, regardless of whether it is the inner or outer liquid flow rate that is altered as can be seen in Fig. 2.12. This linear increase does not agree with either the de la Mora $Q^{1/3}$ or the Gañan-Calvo $Q^{1/2}$ scaling law for single electrospray.

It is thought this stems from the fact that in single electrospray, the droplet diameter is entirely dependent on the break-up of the electrified jet, but in outer-driven coaxial electrospray, the droplet diameter is dependent on the break-up of the inner liquid. The charged outer liquid is pulling the inner non-charged liquid along with it through viscous stress at the jet's liquid-liquid interface. Therefore the diameter of the jet is a balance between the outer liquid accelerating the jet forward and the inner liquid holding the jet back.

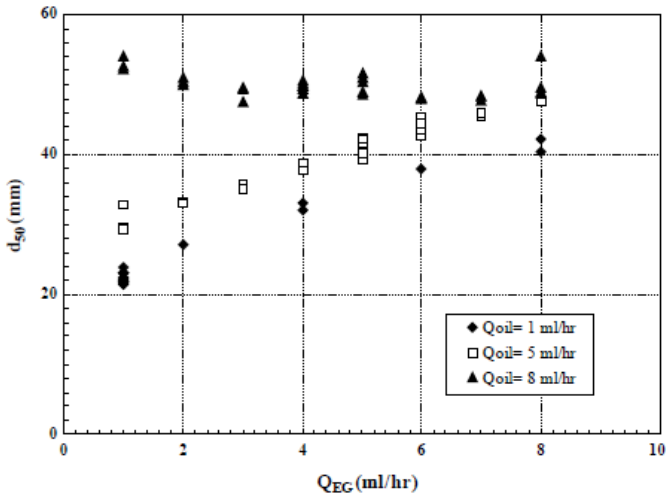

*Figure 2.13 Mean droplet diameter with an inner driving liquid (EG) with an outer liquid of sunflower oil (Lopez-Herrera, J.M., Barrero, A., Lopez, A., Loscertales, I.G. & Marquez, M. J Aerosol Sci **34**, 535-552 (2003)[39])*

When looking at the case of an inner driving liquid, again a linear dependency on the driving flow rate was seen for an outer flow rate of 5 mL/h and 1 mL/h over a range of 1-8 mL/h for the inner liquid (Fig. 2.13). However, at a higher outer flow rate of 8 mL/h, any dependency on the inner flow rate was lost. It was suggested that this is due to the droplet size being dependent on the capillary break-up of the more viscous, uncharged sunflower oil.

While the linear dependency at lower flow rates seems to disagree with the non-linear dependency of single electrospray, when the data is made dimensionless it is difficult to conclusively rule out any agreement with either the $Q^{1/2}$ scaling law of Gañan-Calvo or the $Q^{1/3}$ scaling law of de la Mora and Loscertales.

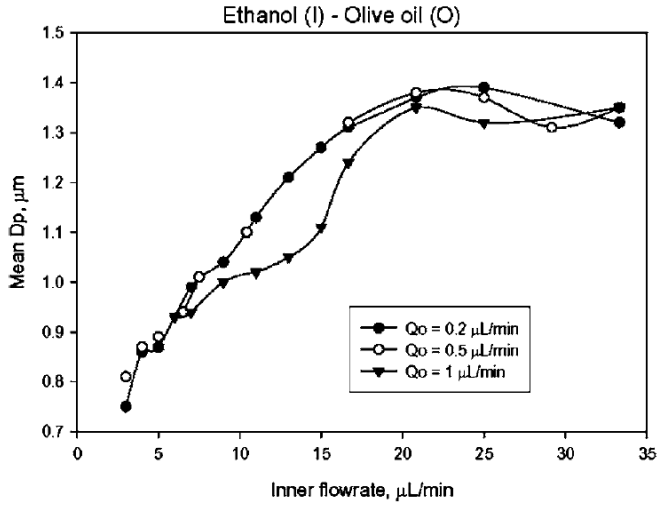

*Figure 2.14 Mean droplet diameter with an inner driving liquid of ethanol and outer liquid of olive oil (Mei, F. & Chen, D.R. Physics of Fluids **19,** 103303 (2007)[40])*

Mei et al.[40] also looked at liquid pairs with an inner driving liquid, but at much lower flow rates and with driving liquids of a lower viscosity than EG (ethanol and

tributyl phosphate were examined) (Fig. 2.14). Although there is not a clear linear dependence as in Fig. 2.13, there is an obvious increase in mean droplet diameter with inner flow rate, up to an inner flow rate of 20 μL/min. This suggests again that there is a limit beyond which the scaling law is not applicable.

2.4 Electrospraying Polymers

Coaxial electrospray presents an excellent method for encapsulation, and is particularly attractive in the biomedical field for its ability to create a delivery system for therapeutic molecules of small size and low polydispersity. It also allows for the use of organic solvents with the shell polymer, which may be damaging to the therapeutic molecules in other circumstances; the organic solvent is in contact with the inner liquid for such a short time before evaporating, that there is negligible negative effect.

2.4.1 Solvent properties

In order to produce dry polymeric particles with a core-shell structure, it is important that the solvent in the outer liquid has completely evaporated by the time the particle reaches the collection plate. The solvent evaporation rate therefore has an effect on the minimum distance needed between needle and collection plate in order to ensure complete evaporation. It also has an effect on when Coulomb fission occurs, which is something to be avoided in order to ensure a small size distribution.

The solvent evaporation rate can also be altered by controlling the environment in which the electrospray takes place, for example by enclosing the system in an airtight chamber and introducing a flow of gas perpendicular to the direction of spray[41-43]. However, the rate of gas flow also affects the motion of the droplets and

this must be accounted for when positioning the collection plate in order to ensure maximum particle collection efficiency[44].

The solvent evaporation rate also has an effect on particle morphology. Zamani et al.[45] used polymer dissolved in various ratios of dichloromethane (DCM) and dimethylformamide (DMF). The mixture of these two solvents was used as DMF has the effect of decreasing the effective solvent vapour pressure[46] and so helps decrease the fast evaporation rate of DCM in order to ensure the polymer chains have time to diffuse through the droplet and form a shell before the solvent evaporates and so reduce porosity[42]. DMF also has the effect of increasing electrical conductivity[47]. However, particle size was seen to decrease with a lower DMF concentration and the mixture of solvents also gave rise to particles with collapsed and non-spherical morphologies. Although the reasons behind this are not addressed by Zamani et al.[45], the presence of fibres attached to the particles was reported which may have been produced through Coulomb fission[13]. The presence of fibres was seen to decrease when DCM alone was used and this could be explained by the lower conductivity, meaning that the Rayleigh limit was not reached before sufficient polymer chain entanglement despite the higher evaporation rate. Park & Lee[48] also noted that in two solvent systems, the differing evaporation rates could lead to phase separation of polymer chain rich and polymer chain poor areas giving rise to porous particles.

As seen in the scaling laws, flow rate is related to the surface tension and decreasing the solvent's surface tension with surfactants can help lower the flow rate.

2.4.2 Polymer properties

The effect of polymer molecular weight on particles was also examined by Zamani et al.[45]. Their findings showed that higher (57.6-91.6 kDa) and lower (31.3-57.6 kDa) molecular weights did not have a significant effect on particle size, but did have significant effect on particle release profiles. Both high and low weight polymers gave similar particle morphologies - spherical with a dimpled surface.

Almería et al.[13] looked at the effect of polymer entanglement on particle morphology, and identified three different scenarios based on the polymer volume fraction of a droplet at the time of Coulomb fission. First they defined three polymer volume fractions: the polymer volume fractions at the Rayleigh limit (φ_{ray}), at chain overlap ($\varphi_{ch.ov.}$) and at entanglement (φ_{ent}).

Scenario 1: $\varphi_{ray} < \varphi_{ch.ov.}$

The droplets undergo Coulomb fission, but following this they are still liquid enough to reform into a spherical shape. Offspring droplets are produced which increases the particle size distribution.

Scenario 2: $\varphi_{ray} > \varphi_{ent}$

If there is sufficient polymer chain entanglement, the polymer shell will prevent any disruption when Coulomb fission occurs. In this situation it is therefore possible that the structure of the shell is formed enough that any offspring droplets will consist of solvent only and so not affect the particle size distribution.

Scenario 3: $\varphi_{ch.ov.} < \varphi_{ray} < \varphi_{ent}$

In this scenario, the polymer chains are sufficiently entangled to prevent the droplet from rupturing at Coulomb fission, but not enough to keep the droplet in a spherical shape. The morphologies of the final particles are therefore 'frozen' at the time of fission, giving rise to elongated particles with long tails.

Coaxial electrospray has been used for biomedical purposes and often use polymers as to create the shell for encapsulation of drugs or DNA. Table 2.1 outlines some liquid combinations used, their spray conditions and the sizes of particles produced. From this, it can be seen that DNA has previously been coaxially sprayed successfully[16, 49]. However, one case looked at lipoplex production[49], and the other case[16], while looking at polyplex production, only used a homopolymer and additionally issues with the spray itself are evident and discussed further in section 3.2.3.

Core	Shell	Needle Dimensions		Flow rates		Concentration		Particle Size	Reference
		Inner	*Outer*	*Inner*	*Outer*	*Inner*	*Outer*		
DNA in OPTI-MEM medium	PEI in OPTI-MEM medium	ID: 0.21 mm	ID: 0.6 mm	6 mL/h	6 mL/h	20 µg/mL	17.2 µg/mL	250 nm	Wu et al. 2010[16]
DNA in 1X PBS	DC-Chol, Egg PC, DSPE-PEG-Mal in ethanol (molar ratio 30:68:2)	ID: 0.21 mm	ID: 0.6 mm	1.2 mL/h	1.2 mL/h	0.5 mg/mL	10 mg/mL	190 nm	Wu et al. 2009[49]
BSA in DI H_2O, PLGA in TFE (1:5)	PLGA in TFE	ID: 0.5 mm	ID: 0.8 mm	0.8 mL/h	0.8 mL/h	39.4 mg/mL	30 mg/mL	2.41 µm	Wang et al. 2013[50]
BSA in DI H_2O	PLGA in DCM	ID: 300 µm OD: 560 µm	ID: 840 um	0.1-0.2 mL/h	1-2 mL/h	10-100 mg/mL	40-60 mg/mL	3-5.5 µm	Zamani at al. 2014[45]
BSA in DI H_2O	PLGA in DCM	ID: 0.41 mm OD: 0.72 mm	ID: 2 mm	0.2-1 mL/h	3-4 mL/h	100-200 mg/mL	50-150 mg/mL	5-10 µm	Xie et al. 2008[51]
PLGA in DMAc	Oestradiol in methanol	ID: 0.9 mm OD: 1.5 mm	ID: 1.9 mm	0.12 mL/h	0.6 mL/hr	100 mg/mL	20-100 mg/mL	100 nm - 2.5 µm	Enayati et al. 2010[52]
Paclitaxel in olive oil	TiO_2 in ethanol, DMF, acetic acid (1:1:1)	—	—	0.8 mL/h	0.4 mL/h	1 g/mL	5 mg/mL	1.5-2 µm	Jing et al. 2011[47]
ALA in ethanol	PLGA in acetone	—	—	1-1.8 (only flow rate ratio given)	2	—	—	0.2-1 µm	Guan et al. 2016[53]
EE 100-55 in ethanol	ERS in DCM	ID: 0.3 mm OD: 0.5 mm	ID: 1.0 mm	0.2 mL/h	0.4-0.8 mL/h	20 mg/mL	20 mg/mL	280 - 440 nm	Hao et al. 2014[54]
Ccurcumin in acetone	PLGA in ethyl acetate	ID: 0.33 mm OD: 0.64 mm	ID: 1.01 mm	0.1-0.5 mL/h	0.1-5 mL/h	20-50 mg/mL	50-100 mg/mL	2-4 µm	Yuan et al. 2015[55]
GF in chloroform	L-100 in ethanol	ID: 0.4 mm	ID: 0.8 mm	0.36 mL/h	0.5 mL/h	10 mg/mL	10 mg/mL	1.86 µm	Zhang et al. 2011[43]

PCL and DOX in acetonitrile, PVP and DOX in ethanol	PLGA and CA4 in THF and acetonitrile (2:8)	—	—	0.2 mL/h	0.8 mL/h	70 mg/mL 50 mg/mL	100 mg/mL	424 nm 455.7 nm	Cao et al. 2014[56]
Budesonide in acetonitrile	PLGA in acetonitrile	—	—	0.048 mL/h	0.3 mL/h	1 mg/mL	2-50 mg/mL	289 nm - 1.2 µm	Lee et al. 2010[57]
CDDP in DMAc	PLGA in DMAc	ID: 0.69 mm OD: 1.07 mm	ID: 1.2 mm	0.12 mL/h	0.24 mL/h	2 mg/mL	20 mg/mL	850 nm	Reardon et al. 2017[58]
PLGA and DOX in DCM	PDLLA in DCM	—	—	0.5-1 mL/h	2.5-7 mL/h	50-200 mg/mL	50-200 mg/mL	30 µm	Xu et al. 2013[59]

Abbreviations: **ID** inner diameter, **OD** outer diameter, **Egg PC** egg phosphatidylcholine, **DC-Chol** 3β-[N-(N',N'-dimethylaminoethane)-carbamoyl] cholesterol, **PBS** phosphate buffer solution, **DI H_2O** deionised water, **ALA** 5-aminovulinic acid, **EE 100-55** Eudragit L 100-55, **ERS** Eudragit RS, **GF** griseofulvin, **L-100** Eudragit L-100, **PCL** polycaprolactone, **PVP** polyvinylpyrrolidone, **DOX** doxorubicin, **CA4** combretastatin A4, **THF** tetrahydrofuran, **CDDP** cisplatin, **DMAc** dimethylacetamide, **PDLLA** poly-DL-lactic acid, **PLGA** poly(lactic-c-glycolic acid)

*Table 2.1 Liquid combinations used in coaxial electrospray for biomedical purposes. (Adapted from Kavadiya, S. & Biswas, P. J Aerosol Sci **125**, 182-207 (2018)[60])*

2.5 Gene Delivery

Gene Therapy	Disease-type	Approving body	Year approved
Luxturna	Retinal disease	FDA, EMA	2018, 2018
YESCARTA	Non-Hodgkin lymphoma	FDA, EMA	2017, 2018
Kymriah	Leukaemia	FDA	2017
Zalmoxis	Stem cell transplantations in high-risk blood cancer	EMA	2016
Strimvelis	ADA-SCID (immuno-deficiency)	EMA	2016
ImLygic	Melanoma	FDA, EMA	2015, 2015

Table 2.2 Currently approved genetic therapies

Gene therapy is the insertion of genes into a patient's cells for medical treatment and is particularly promising with regard to treating genetic disease and cancer. It is a relatively young field of research with clinical trials starting in 1989 and only a handful of therapies currently approved by the US Food and Drug Administration (FDA) and the European Medicines Agency (EMA) (Table 2.2). Luxturma, Strimvelis and ImLygic use viruses as their delivery vehicle (adeno-associated virus, retrovirus and herpes simplex virus 1 respectively), while the other therapies involve genetically modifying a patient's own T-cells (a type of immune cell) before returning them to the body.

Therapeutic genes can be used in various ways, including: 1) replacing a faulty gene with a healthy version, 2) interfering with or preventing the activity of a disease-related gene, or 3) promoting the death of diseased cells such as cancer cells. Gene insertion into a cell requires a method of delivery and these methods can be divided into two main categories - gene delivery of naked DNA directly to the site of interest, and gene delivery which requires a vector.

For successful gene delivery, therapeutic genes must travel to target cells, enter inside and then be expressed. Each of these stage poses a challenge: genes must survive degradation within the body when outside the target cells, they must pass through the cell membrane, and any gene vector must break down to release the genes allowing them to be expressed.

Delivering a gene to a specific cell type requires a cell targeting strategy. A common strategy is to identify a receptor that is overexpressed on the target cell compared to other cells, and functionalise the delivery vector with an appropriate ligand for the target receptor[61, 62]. An alternative strategy is external guidance. Silva et al.[63] incorporated magnetic nanoparticles into macrophage-derived vectors and were able to guide them *in vitro* via an externally applied magnetic field. This strategy has also been used successfully in rats for cardiac regeneration[64], and to suppress ovarian cancer growth in mice[65].

2.5.1 Gene Vectors

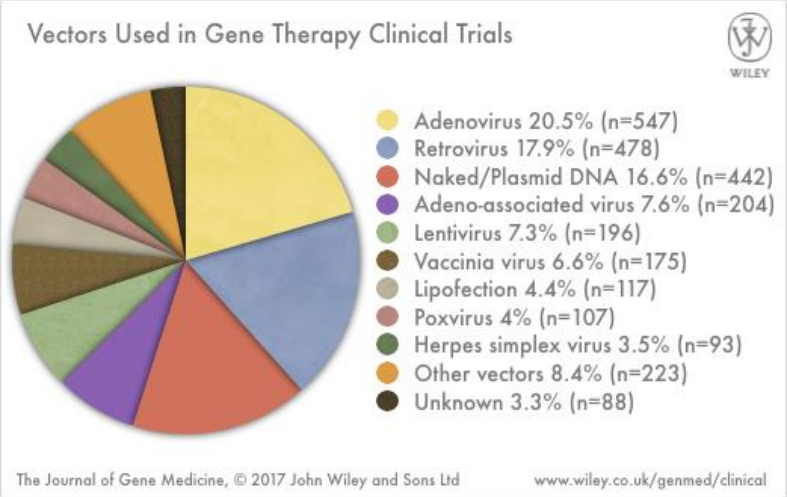

Figure 2.15 Data on vectors used in clinical trials worldwide, compiled by the Journal of Gene Medicine[66]

In the history of gene therapy clinical trials worldwide, so far only 1 out of a total 2,597 has been classified by the Journal of Gene Medicine as using a non-viral vector[66] (Fig. 2.15, a detailed breakdown of vectors used can be found on the website[67]). The vast majority of trials use viral vectors and a small portion use no vector.

2.5.1.1 Viral Vectors

Viral vectors are the most commonly used vectors as they are already optimised to travel through the body, enter cells and release DNA. While viral vectors have differences in structure, the ones most commonly used in clinical trials can be generalised to the following: genetic material encased in a protective shell (capsid) coated with proteins which facilitate entry into the host cell. The main differences are

whether the genetic material is RNA or DNA, whether it is single or double strand, if there is an additional envelope around the capsid and the types of proteins on the outside of the virus.

However, there are several drawbacks to viral vectors. The first is immunogenicity; there can be an immediate immune response upon administration of the viral vectors[68-70], or one can develop following repeat administration[71-73]. The severe effects of immunogenicity were made tragically apparent during a clinical trial involving the death of a patient[74], and other clinical trials where patients went on to develop leukaemia[75, 76].

Additionally, immune responses can vary between animal models, making it hard to predict the immune response in humans. Dicks et al.[77] saw different cellular and humoral immune responses to adeno virus-mediated immunisation between mice and cattle, a clinical trial showed a lack of long-term gene expression in humans due to T cell-mediated immunity, contradicting preclinical trial results which had seen long-term expression in mice and dogs[78]. Li et al.[79] also saw differences in immune response between human and rhesus macaques to adeno-associated virus-mediated gene transfer; long-term gene expression was achieved in macaques but not in humans. In short, differences in immune response are possible between non-primate mammals, primates, and humans which adds an additional layer of difficulty when setting up clinical trials.

A second limitation is that each virus type has a set genome size, and the amount of therapeutic genetic material that can be inserted is dependent on how much of the genome can be safely deleted without compromising the ability of the virus to

perform gene delivery[80]. If the therapeutic payload does not fit in the virus, then non-viral methods must be considered.

2.5.2.2 Naked DNA

Injecting naked DNA can avoid any issues that come about from immune response to capsids or insertational mutagenesis – the occurrence of mutations in the DNA due the insertion of additional base pairs. However, naked DNA has no protection from degradation within the body and it has been shown in mice that the half-life of injected plasmid DNA (pDNA) is around 10 minutes[81]. Therefore the use of naked DNA is not ideal in situations where it cannot be delivered directly to the target site.

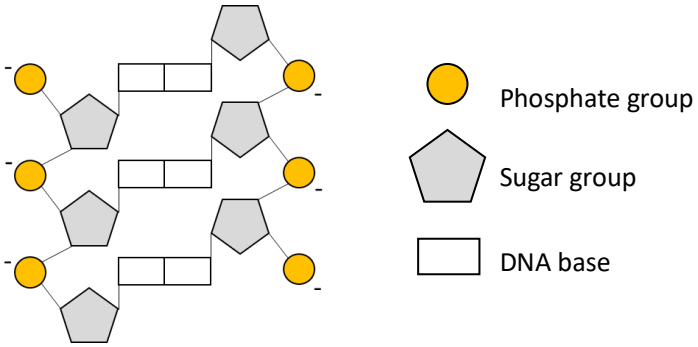

Figure 2.16 DNA structure

DNA molecules are made up of phosphate groups, sugar groups and DNA bases (Fig. 2.16). The DNA bases form the genetic code and are held together by the phosphate and sugar groups – referred to as the sugar-phosphate backbone. It is the negative charge on the phosphate group which gives DNA its negative charge. As the cell membrane is also negatively charged, physical mechanisms such as electroporation[82] and sonoporation[83] (use of electric field and ultrasound respectively

to increase cell membrane permeability) are necessary to allow DNA to penetrate into the cell.

2.2.5.3 Non-viral Vectors

DNA can be encapsulated in biodegradable polymers, creating a non-viral DNA delivery system. Non-viral vectors are of particular interest as they provide a solution to any issues with immunogenicity which are a possible risk when using viral vectors[74]. As DNA has a negative charge, the use of a polycation (a polymer with a positive charge) allows for the DNA to be compacted (known as DNA condensation) thereby leading to a smaller capsule. As previously stated, the membrane of a cell is negatively charged, so another benefit of using a polycation is that it is able to enter a cell through a process called endocytosis[84] (Fig. 2.17). The capsule will then be broken down and so achieve transfection (transfer of DNA into a cell) of the encapsulated DNA.

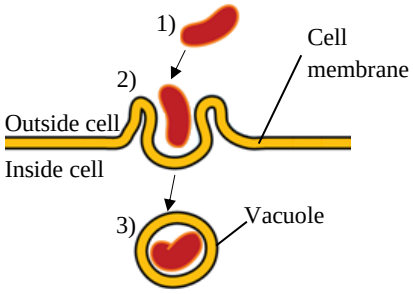

Figure 2.17 The process of endocytosis: 1) a particle approaches the cell membrane, 2) the cell membrane engulfs the particle, 3) the cell membrane pinches off into a capsule (known as a vacuole) and carries the particle into the cell.

Various structures of non-viral vector have been made and the methods by which they are produced can be grouped into three main categories: basic electrostatic interaction, encapsulation, and adsorption.

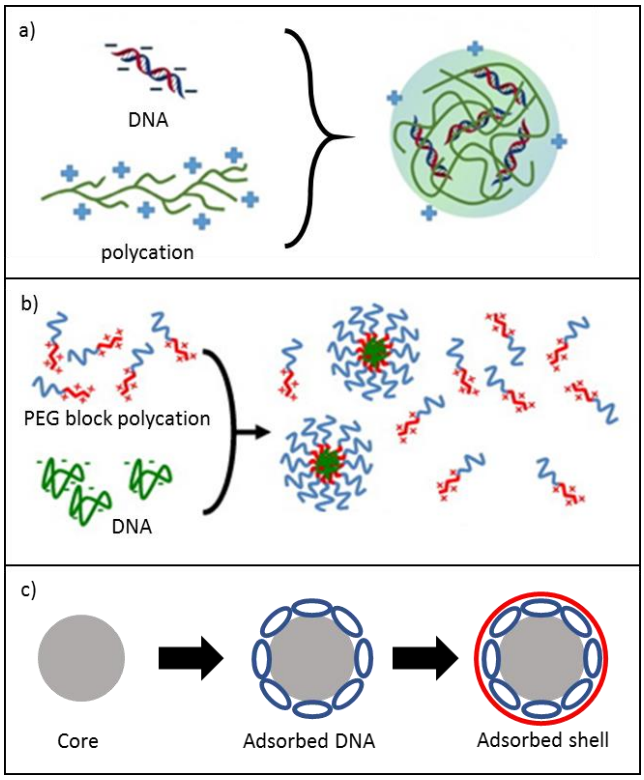

*Figure 2.18 a) electrostatic interaction between DNA and a branched polycation leading to a polyplex, b) a polycation with a PEG (polyethylene glycol) block and plasmid DNA leading to a micelle with DNA complexed with the polycation at the core and a PEG corona, c) DNA adsorbed onto a core, with a shell adsorbed onto the DNA using a layer-by-layer technique (a) adapted from Liao, J.F. et al. Theranostics **7**, 2593-2605 (2017)[85], b) adapted from Uchida, S. et al. Journal of Controlled Release **155**, 296-302 (2011)[86])*

DNA is negatively charged, so polycations are used as they will easily complex with DNA through electrostatic interaction[85, 87] (Fig. 2.18a). The most basic

particle is simply the DNA entangled with a single type of polycation and the only consideration needed is that the resulting polyplexes have an overall positive charge so the main parameter to be controlled is the ratio of polymer to DNA.

DNA can also be encapsulated in a micelle structure through the use of block copolymers, a polycation attached to a hydrophilic block. In aqueous phase the positively charged block of the copolymer will complex with the DNA, with the hydrophilic part of the copolymer forming a shell or corona [86, 88] (Fig. 2.18b) with the polymer molecules aligned radially. The hydrophilic part of the polymer can also be augmented with other components for other beneficial effects. Uchida et al.[86] used the addition of chondroitin sulfate to reduce inflammation at the site of injection, and Dhande et al.[89] were able to design a novel diblock glycopolymer that promoted the uptake of pDNA capsules by liver cells.

Finally adsorption can be used to build up particles with the layer-by-layer technique (Fig. 2.18c). DNA is adsorbed onto a core and further layers can be adsorbed on top[90, 91]. Bishop et al.[92] used five alternating layers of polymer and DNA on gold nanoparticles to codeliver DNA and siRNA (silencing RNA). This method also gives more control over the size of the particle; starting with a smaller core should give a smaller final particle.

As well as structure, size is an important consideration in the production of therapeutic delivery systems as it has an effect on the cell uptake[8], but it is not always the case that smaller is better. He et al.[9] compared cell uptake for three particle diameters (150 nm, 300 nm and 500 nm) for a variety of cell lines and found that in all cases 150 nm had the highest uptake. However, Xu et al.[10] looked at uptake for two cell lines for a range of particle diameters (50 nm – 300 nm) and found that 100 nm

performed best and 50 nm performed worst. Therefore it is important to be able to tune the size of any therapeutic delivery system depending upon the type of cell being treated.

There are various polycations that have been used in research for gene delivery[16, 42, 93, 94]. Polylactic acid (PLA) and poly(lactic-co-glycolic) acid (PLGA) are commonly used[95-98] because they are already approved for use by the FDA as they degrade to carbon dioxide and water[99]. As well as biodegradability and biocompatibility, polycations can also be selected for their intrinsic beneficial properties. Both PLA and PLGA can be used as adjuvants to increase the efficacy of a vaccine[100-103], polyethylenimine (PEI) can be used to increase transfection rates[104, 105], and coating with polyethylene glycol (PEG), known as PEGylation, can help prevent aggregation[106] and prevent capsules from being cleared from the body through phagocytosis by preventing the adsorption of opsonins[107].

It has been shown that DNA can be electrosprayed and maintain the capacity for gene expression[14, 108], making electrospray a good method for DNA encapsulation and subsequently the production of a non-viral gene vector. However, there are very few studies that have used DNA in electrospray.

Chen et al[14] used coaxial electrospray plasmids containing Enhanced Green Fluorescent Protein (eGFP) in the inner liquid, and an outer liquid of deionised water with nitric acid in a 1:50 ratio. The outer liquid was used to control the charge of the generated droplets. Rather than DNA encapsulation, this study looked at the use of electrospray itself as a means of delivering and transfecting DNA – the liquids were sprayed directly at live cells and were able to penetrate the cell membrane due to their high velocity.

Wu et. al.[16] compared self-assembled plasmid DNA/polyethylenimine (PEI) polyplexes with coaxially sprayed capsules of plasmid DNA in PEI. Two types of plasmid were used, one which encoded green fluorescent protein (GFP) and another which encoded secreted alkaline phosphatase (SEAP). First, the plasmids were sprayed in single electrospray and the sprayed plasmids were tested with gel electrophoresis to ensure that they had not degraded. GFP plasmids were sprayed at 6 mL/h and SEAP plasmids in 4, 6 and 8 mL/h. In all cases it was seen that the plasmids were not damaged by the electrospray process.

The plasmids were then coaxially electrosprayed with PEI in the outer needle to produce plasmid DNA/PEI polyplexes and all liquids were sprayed at 6 mL/h. The plasmids and PEI were both suspended in OPTI-MEM medium. These polyplexes were compared with those produced by self-assembly in the same concentrations. The electrosprayed particles were found to be smaller than the self-assembled ones for GFP, but larger for SEAP. However, as particle size in electrospray is related to flow rate, it is possible that using a lower flow rate with SEAP would have been able to produce smaller particles. When looking at SEAP expression in transfected cells, the electrosprayed particles produced by different flow rates were compared so it is possible that the 4 mL/h sprayed particles would have been smaller than the self-assembled ones. A reason for only measuring the size of 6 mL/h sprayed particles is not given.

When looking at cell transfection, the electrosprayed GFP particles showed similar results to the positive control of Lipofectamine 2000 unlike the self-assembled particles which were not as effective at transfection. However, the GFP only allows for a qualitative analysis of transfection so the SEAP transfection was necessary to

allow for a quantitative measure of transfection by measuring the activity level of alkaline phosphate. Once again, it was seen that the electrosprayed particles had a better rate of transfection than the self-assembled ones. However, the reason for this is not established. While the structures of the particles were not compared, it is possible that it is the positively charged PEI shell in the core-shell structure produced by coaxial electrospray gives it an advantage over a self-assembled structure when entering a cell which has a negatively charged surface, allowing the particle to be endocytosed.

The mechanism by which PEI transfects is known as the "proton sponge"[109], although the precise details are still debated[110]. It is thought that PEI is able to escape endosomes within the cell by absorbing protons that are pumped into the endosome. Following the accumulation of protons in the endosome, chloride ions passively enter the endosome which increases the ionic pressure. This leads to water entering the endosome which then swells and bursts, releasing the PEI into the cell.

Chapter Three

Experimental Methods

3.1 Electrospray Methodology

The objective is to use coaxial electrospray to generate capsules of DNA with a polymer coating for use as a non-viral gene delivery system. The important features of these particles are that they have diameters on the nanoscale, demonstrate a core-shell structure and have an overall positive charge for efficient cell uptake (section 2.5.1).

Important parameters to be controlled are of course the flow rate, due to the scaling law dependence of droplet diameter upon it, and the applied voltage to the needle in order to be spraying in the stable cone-jet mode.

It is also important to visualise the liquids as they exit the needle tip to ensure that they are forming a stable cone-jet, and also to monitor the spray current for further confirmation of a stable spray. Fluctuations in spray current could indicate flow rate fluctuations that are not perceptible from simply viewing the cone-jet. Additional parameters to monitor are the ambient temperature and humidity as changes in temperature will affect liquid properties and changes in humidity will affect the solvent evaporation rate.

3.2 Coaxial Electrospray Apparatus

A schematic of the equipment used can be seen in Fig. 3.1, and is as follows: the liquid is supplied with a controlled flow rate by two syringe pumps with glass syringes. These are connected to a stainless steel coaxial needle by perfluoroalkoxy alkane (PFA) tubing with Luer lock fittings. A stainless steel extractor is positioned slightly below the needle and below that is a grounded metal collection plate. Both the needle and extractor are connected to high voltage power supplies.

The current through the needle was measured with a 100 kΩ shunt resistor, and a 1 MΩ resistor was used to protect the system from an unexpected current surge. The cone-jet was imaged with a CCD camera attached to a zoom lens with a ring light source.

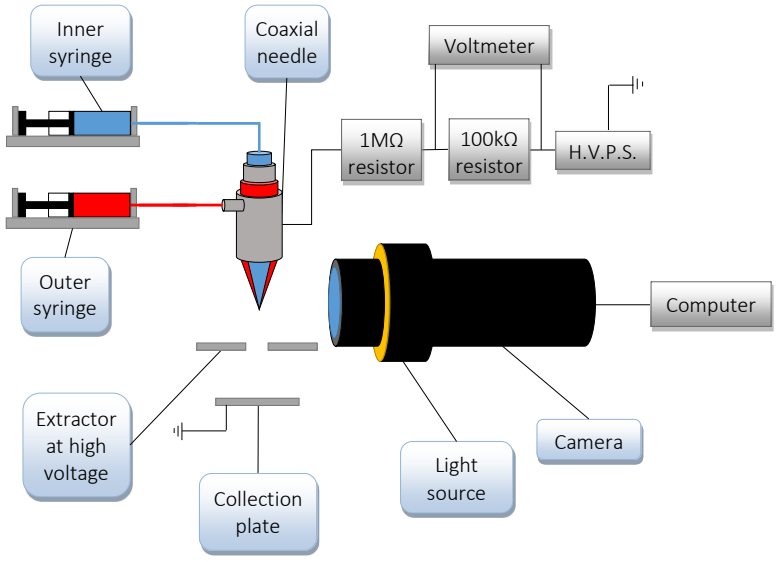

Figure 3.1 Schematic of electrospray set-up used

When setting up the electrospray equipment, there are many options to consider and each has their own advantages and disadvantages and the choices taken in choosing electrospray equipment are often not reported. The following sections will examine the various alternatives available and explain why each piece of equipment was eventually chosen for use.

3.2.1 Liquid Supply

There are two choices for liquid supply, either syringe pumps or pressure head. Using syringe pumps allow for precise control of the flow rate (which is related to particle size), but a disadvantage is that pulsations can occur due to the step motor which drives a syringe pump and can be a factor in the polydispersity seen in particle sizes. Li et al.[111] used a co-flow microfluidic device (Fig. 3.2) to observe these pulsations. In that report, the outer liquid was supplied under gas pressure and the inner liquid supplied by syringe pump, with the inner liquid needle protruding into the flowing outer liquid. The two liquids were chosen to have a low interfacial tension to better visualise at the interface any ripples caused by flow fluctuation.

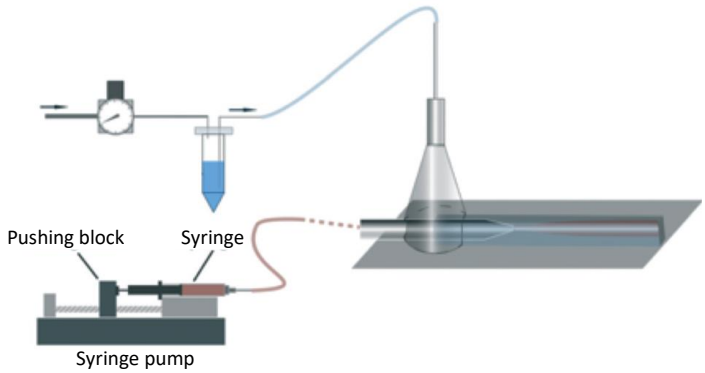

*Figure 3.2 Set-up using both syringe pump and pressure head (Li, Z., Mak, S.Y., Sauret, A. & Shum, H.C. Lab on a Chip **14**, 744-749 (2014)[111])*

The inner liquid formed a jet and ripples were visible at the interface between the two liquids. The frequency of ripples was analysed and seen to relate to the step size of the syringe pump. They estimated that the fluctuations for flow rate would be on the order of 1-2%.

Pressure-head driven electrospray systems remove this fluctuation, but leave the flow rate susceptible to changes in applied voltage. Ryan et al.[37] used gravity pressure head for single electrospray, and saw that in the cone-jet spray regime, flow rate increased approximately linearly with voltage for a variety of liquids. The flow rate in syringe pump driven systems is unaffected by voltage due to high hydraulic impedance.

Syringe pumps are overwhelmingly the most popular choice[30, 42, 45, 50, 51, 56-59, 112-117] with the remainder of papers only stating that the liquid was fed through a needle without stating the method[16, 93]. However, it can be assumed that the popularity of syringe pumps is due to their ease of use when controlling flow rate which is vital for particle diameter control. At the time of writing, coaxial electrospray papers regarding encapsulation using pressure head as a liquid feed method could not be found.

One of the aims of this research was to produce small diameter particles (on the nanoscale) which requires the use of low flow rates. As established by the jet diameter scaling law – jet diameter scales with flow rate and so lower flow rates will produce smaller droplets. However, at low flow rates, fluctuations have a strong effect on cone-jet stability.

Syringe pumps are used as standard for biological encapsulation. They operate using a stepper motor, meaning that rather than moving in a smooth, continuous

motion, the plunger of the syringe is pushed a discrete distance each time the motor turns by one step. When syringe pumps are operating near their minimum flow rate, these steps can be seen through fluctuations in liquid flow.

With this in mind, a gravity-driven pressure-head system was chosen for the initial electrospray set-up. The body of a plastic syringe was punctured so that the liquid inside was open to atmosphere. The pressure-head could then be adjusted by raising or lowering the syringe to alter the height of the liquid meniscus. The liquid flow could be stopped by moving the meniscus to the level of the needle tip. The pressure-head was calculated by $P = \rho g h$, where h was normalised to zero at the level of the needle tip.

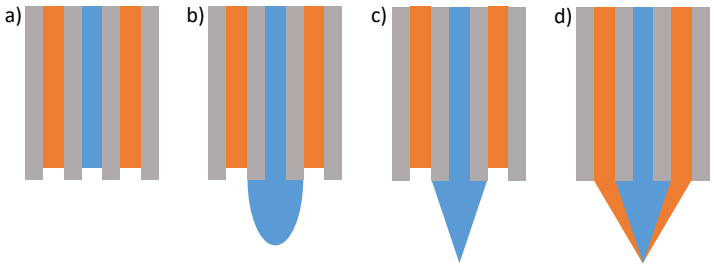

Figure 3.3 a) both liquids partially fill their respective needles, b) inner liquid syringe is raised until a drip of inner liquid can be seen, c) increasing voltage is applied to the needle until cone-jet mode is reached, d) outer liquid syringe is raised until outer liquid emerges from needle and coaxial cone-jet mode is established

Setting up a stable cone-jet spray was fairly quick and easy with this set-up and the process is outlined in Fig. 3.3. Both syringes were filled with liquid and the liquid menisci were kept below the height of the needle tip to prevent them from dripping, and potentially mixing together. The inner liquid syringe was raised until liquid could be seen protruding from the needle tip. Increasing voltage was then

applied to the needle until the onset voltage was reached and a stable cone-jet was formed. In these initial tests, the inner liquid cone-jet was established first as the inner liquid was the driving liquid. The syringe for the outer liquid was then gradually raised until the liquid emerged from the outer needle and formed a coaxial cone-jet.

The reason for establishing the inner cone-jet first was to ensure that the liquids could not mix within the coaxial needle which would lead to instability and also produce particles which lack a core-shell structure.

This method produced a stable cone-jet spray and polymer particles. However, there were some drawbacks to this approach. The first was that the height of the syringe was adjusted by hand and measured against a ruler, so the flow rate was not finely controlled. The second drawback was that the flow rate was not directly known, and this was complicated by the fact that flow rate is affected by changes in applied voltage even while remaining in the same spray mode. A change in flow rates would also lead to a change in the polymer ratios meaning that repeatability could be a problem as the onset voltage was not always the same due to uncontrolled environmental factors such as humidity and temperature. Finally, over the course of electrospray the height of the menisci will of course drop, and so change the pressure-head and flow rate.

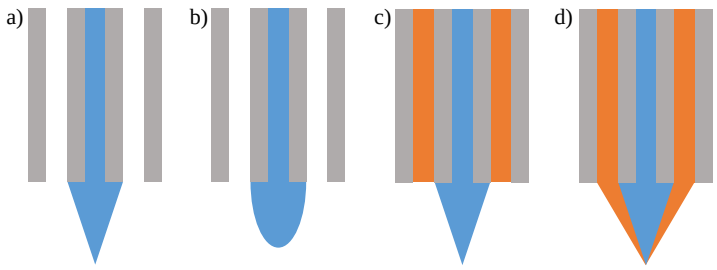

Figure 3.4 a) inner cone-jet is established to find onset voltage, outer needle is empty, b) voltage applied to needle is turned off, extractor voltage kept on, inner flow rate stopped, and outer syringe connected, c) the outer needle is filled, and inner cone-jet re-established, d) outer liquid is drawn over the inner cone-jet forming a coaxial cone-jet

As a result of these difficulties a decision was taken to move to using syringe pumps (PHD 2000 Infusion, Harvard Instruments) to allow for direct and precise control over the flow rates without being affected by the applied voltage. The same coaxial spray set-up sequence was followed; the inner liquid cone-jet was established first before the outer liquid is added. The set-up procedure outlined in Fig. 3.4 however, was slightly more complex. After the inner cone-jet had been established, the flow rate and applied voltage were then stopped while the outer flow rate was connected. The reason for keeping the outer liquid disconnected while setting up the inner flow was to ensure that there was no build-up of polymer on the connecter as the solvent used (chloroform/DMF mixture) was quite volatile.

The inner liquid flow was restarted, voltage applied and the cone-jet was re-established. Then the outer liquid flow was started, filling the outer needle and the outer liquid was drawn over the inner cone-jet forming a coaxial cone-jet.

3.2.2 Syringes

Another important factor in the liquid supply is the choice of syringe and the material used for connectors. Plastic syringes are extremely convenient for use; they are cheap so a new one can be used each time and no cleaning is required. However, they are subject to deformation by pressure which will affect the accuracy of the delivered flow rate, making a glass syringe a better choice. In practice however, the type of syringe used is often unspecified[16, 30, 45, 50, 56-59, 114, 117-119], or a reason for the choice between plastic[113, 115, 116] or glass[42, 93] is not given.

As well as the choice between syringe materials, the compatibility between solvents and all materials that they will come into contact with in the system needs to be considered[120], to prevent degradation of the equipment and contamination of the liquid supply. For the outer liquid, it was determined that stainless steel and polytetrafluoroethylene (PTFE) would be compatible with potential solvents, so a stainless steel Luer lock connector was used to connect the tubing to the coaxial needle, and a syringe with a PTFE Luer lock connector and PTFE tipped plunger (Hamilton Gastight) was chosen. For the inner liquid, again a glass and PTFE syringe (Hamilton Gastight) was used. PFA tubing (inner diameter: 750 μm) was used between the syringes and coaxial needle in both cases.

3.2.3 Coaxial Needle

The most conventional configuration of a coaxial needle is two straight needles, one within the other. The material for the coaxial needle is almost always stainless steel and can be made with[55] or without[49] a method to centre the inner needle within the outer needle (Fig. 3.5a), although without centring the inner needle can be off-centre (Fig. 3.5b).

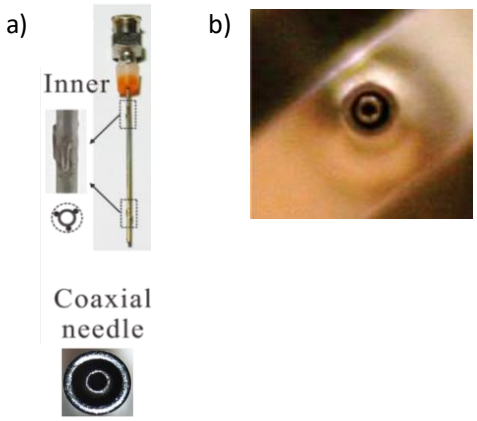

*Figure 3.5 Coaxial needles a) six pieces of wire are welded onto the outside of the inner needle to ensure it is centred within the outer needle[55] b) no centring method is used, leaving the inner needle off-centre[49] (Adapted from Yuan, S. et al. Plos One **10** (2015)[55] and Wu, Y. et al. Molecular Pharmaceutics **6**, 1371-1379 (2009)[49])*

There is an alternative configuration which was used by Hwang et al[38] to electrospray core-shell particles of high concentration polymers. In this set-up (Fig. 3.6), to avoid having to centre the needle, the inner needle was instead bent to be touching the inside of the outer needle in order to create an easily reproducible inner needle position. While this seems counterintuitive to producing core-shell particles, this set-up takes advantage of 'die swell', a process that applies to viscoelastic fluids.

In basic terms, when a viscoelastic fluid passes through a narrow capillary, the fluid will expand upon exiting the capillary[121].

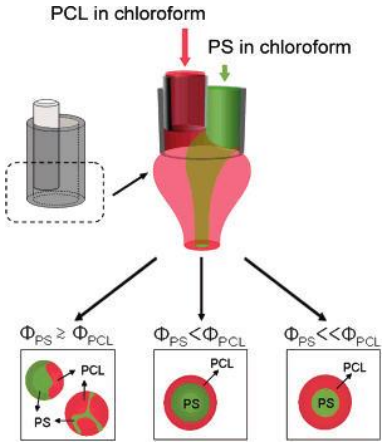

*Figure 3.6 Coaxial needle set-up where the inner needle tip is both recessed within the outer needle and bent to touch the outer needle. The liquid used were high concentrations of polycaprolactone (PCL) and polystyrene (PS) both in chloroform. (Hwang, Y.K., Jeong, U. & Cho, E.C. Langmuir **24**, 2446-2451 (2008)[38])*

In the case of the coaxial electrospray, when the inner liquid exits the tip of the inner needle, it experiences a large increase in volume and expands. As it exits the outer needle it expands again and engulfs the outer liquid, so the inner liquid becomes the shell and the outer liquid becomes the core. With this set-up, provided the inner liquid flow rate was higher than the outer liquid flow rate, it is possible to produce core-shell particles where the thickness of the shell is dependent on the inner flow rate.

However, as this needle configuration requires viscoelastic liquids, this method is not suitable to use with all liquids. Additionally, there is the issue of the needles clogging as high concentration polymer solutions are being used. The sudden swelling of the liquid upon exiting the needle tip promotes wetting of the outside of

the needle, and the fast evaporation of the solvent means that a large precipitate can be left behind. This was seen particularly with polymer solutions with a high glass transition temperature and larger diameter needles were required for stable spraying. Therefore this needle configuration is not suitable for aims of this thesis.

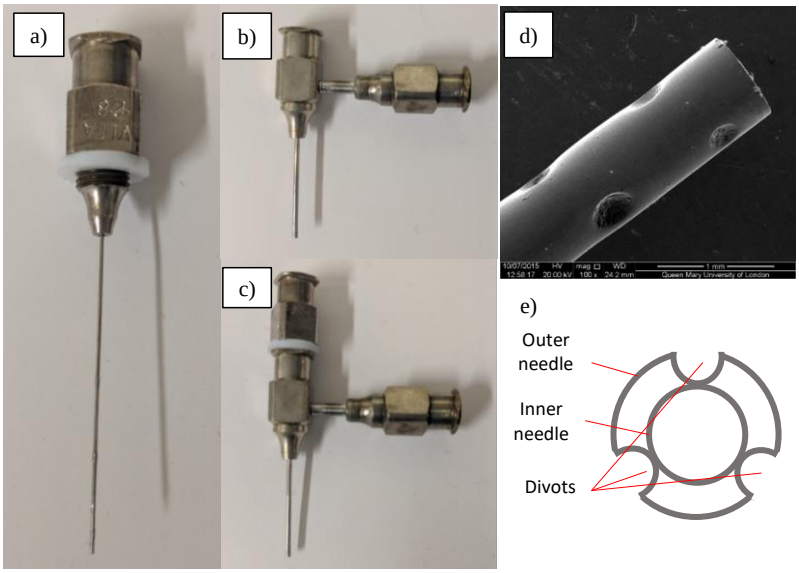

Figure 3.7 a) inner needle (28 gauge), b) outer needle (21 gauge), c) assembled coaxial needle, d) SEM image of needle-tip showing centring divots in outer needle, e) diagram (not to scale) demonstrating a cross-section of the needle's centring system

The stainless steel coaxial needle (ramé-hart instrument co.) centres the inner needle by means of divots pressed in from the outer needle (Fig. 3.7d & e). The centring is important to ensure a symmetrical electric field around the tip of the needle, and to ensure an even flow of the outer liquid in the annular space around the inner needle. Needles with a blunt tip rather than bevelled tip were chosen as a bevelled tip needle has a much thinner wall at the tip and so any degradation would have a far greater effect on the symmetry of the electric field requiring needles to be replaced

more frequently compared with a blunt tip. The inner needle (Fig. 3.7a) was 28 gauge (inner diameter: 0.178 mm, outer diameter: 0.356 mm) as it was the smallest needle offered by ramé-hart instrument co. for a centred coaxial needle that could be dissembled. The outer needle (Fig. 3.7b) was chosen to be 21 gauge (inner diameter: 0.508 mm, outer diameter: 0.810 mm) as this was the lowest sized outer needle that had an inner diameter large enough to fit around the inner needle. The smallest diameter needles possible were chosen in order to be able to produce small, monodisperse particles. While Tang & Gomez saw no effect on droplet diameter with needle gauge when using pure liquids[122], Arya et al. found that mean particle size and polydispersity of electrosprayed chitosan particles reduced with needle size[93].

The primary concern when using the needle is how to prevent wetting; that is how to prevent the liquid from clinging to and travelling up the outside of the individual needles as can be seen in Fig. 3.8. This is necessary because in the case of the inner needle, it can interfere with the flow of the outer liquid and potentially lead to the liquids mixing. In the case of the outer liquid, it can collect on the outside of the needle and then be drawn back down into the cone-jet, leading to a sudden increase in flow rate and destabilisation.

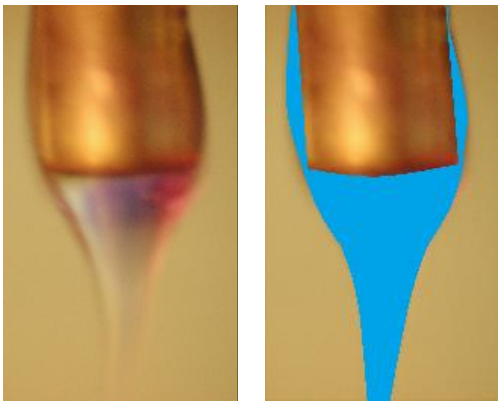

*Figure 3.8 The outer liquid can be seen wetting up the outside of the needle (Adapted from Wu, Y., Fei, Z., Lee, L.J. & Wyslouzil, B.E. Biotechnol Bioeng **105**, 834-841 (2010)[16])*

To avoid wetting, the outside and flat edge of the outer needle were coated in a solution (C2 liquid crystal concentrate v2, GTechniq) which works to form a crystal layer over the outer surface of the outer needle. The coating was achieved by dipping the outer needle into the C2 solution while pushing air through the needle to avoid the inside being coated. It was then left to air-dry. The inner needle was not coated as problems with the inner liquid wetting the outside of the inner needle were not encountered.

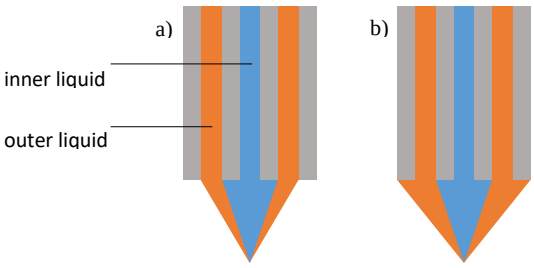

Figure 3.9 a) outer liquid wetting to the inner edge of the outer needle, b) outer liquid wetting to the outer edge of the outer needle

There is also a choice between having the outer liquid attached either to the inner edge of the outer needle (Fig. 3.9a) or wetting to the outer edge (Fig. 3.9b). Even if a stable cone-jet spray is established with the outer liquid wetting to the outer edge of the outer needle, it is still possible for it to begin to wet up the outside of the needle during spraying. Keeping the outer liquid attached to the inner edge of the outer needle reduces the possibility of this happening and so reduces the risk of instability.

With a coaxial needle, there is also a choice between whether to have the inner needle tip recessed, protruding[49, 112] or level with the outer needle tip. Although this is not a parameter generally commented upon, from images and schematics it can be seen that all three configurations are in use[16, 123, 124].

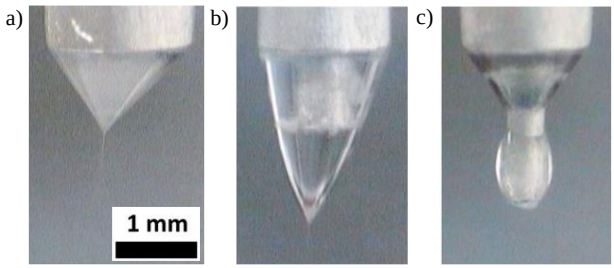

*Figure 3.10 Different levels of protrusion inner needle a) cone-jet mode with inner needle level with outer needle, b) cone-jet mode with 1 mm protrusion, c) dripping mode with 2 mm protrusion (Adapted from Sofokleous, P., Lau, W.K., Edirisinghe, M. & Stride, E. Rsc Advances **6**, 75258-75268 (2016)[125])*

Sofokleous et al[125] compared the three configurations (Fig. 3.10) and found that the inner needle recessed by 2 mm gave the best performance. This was determined by looking at the encapsulation rate and average particle diameter for each inner needle position. The inner needle recessed by 2 mm had the best result in both

cases, and the second-best position was 1 mm protruding. However, when the needle was protruding by 2 mm, a stable cone-jet could not be established. This was determined to be because the vertical distance from the needle tip to the tip of the cone was less than 2 mm and therefore the inner needle tip interfered with the formation of the meniscus of the cone-jet.

Practically speaking, in an inner driving liquid scenario for the start-up sequence used, having the inner needle protruding is the only configuration that allows for visual confirmation that a stable cone-jet has formed without the inner liquid wetting up the outside of the needle. It is also easier to measure the protrusion of the inner needle with the camera and so ensure that the needle configuration is repeated for each experiment, than with a recessed or level inner needle.

The final stabilising factor for the set-up to ensure a stable cone-jet was to place the mount for the needle, extractor and collection plate on a vibration isolation table (Micro 40, Halcyonics).

3.2.4 Extractor

The use of an extractor helps to concentrate the footprint of the electrospray and also encourage the droplets to travel downwards to the collection plate and was kept at around 1-2 kV relative to ground. It was also found that the extractor played a role in pulling the inner liquid down when the extraction potential was progressing the electrospray from dripping mode to cone-jet mode whilst preventing fluid from wetting up the needle. This was important when the inner liquid flow was stopped and the voltage applied to the needle was turned off, as the extractor voltage could be left

on as the inner liquid would otherwise be prone to wetting up the outside of the inner needle.

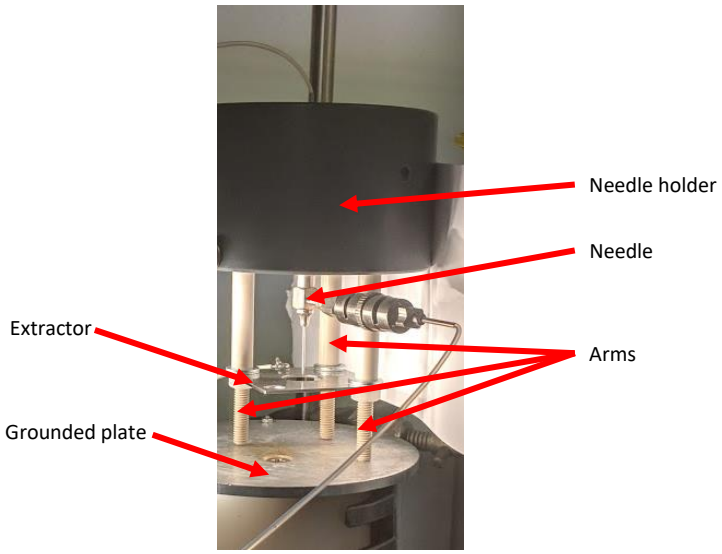

Figure 3.11 Image of needle and extractor holder with grounded plate

With regard to position relative to the needle tip, while wanting the extractor to be close to the tip of the needle, it had to be far enough away that it did not interfere with the view of the cone-jet through the camera. The extractor was therefore fixed a few mm below the needle-tip so that the view of both the cone and jet were not obstructed. The extractor was fixed to arms (indicated in Fig. 3.11) extending downwards from the needle mount and could be moved slightly around the arms before being fixed in place by nylon bolts so that the needle tip could be centred in the extractor aperture.

The aperture of the extractor used was 13 mm in diameter. Initially a smaller diameter was used but problems were encountered where if the cone became biased

towards one side of the needle, the jet could reach the side of the aperture and short circuit.

3.2.5 Applied Voltage

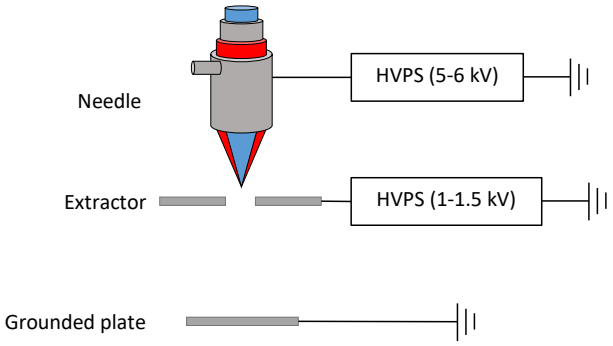

Figure 3.12 Diagram indicating the voltages applied to the needle and extractor relative to ground

Voltage was applied to the needle and extractor by high voltage power supplies (HCL 14-20000, FuG) (Fig. 3.12) via a ring terminal around a screw that screwed into the needle holder to make contact with the needle, and two more ring terminals that were screwed onto the extractor plates ensuring a good connection. The voltage applied to the needle was positive to reduce electrical discharge[36] and the onset voltage was used, generally with the applied voltage to needle around 5-6 kV relative to ground. The extractor was at a lower positive voltage, generally 1-1.5 kV relative to ground and was adjusted based on keeping the inner liquid pulled down and preventing it from wetting up the outside of the inner needle as the applied needle voltage is increased.

3.2.6 Collection Plate

There are two main methods of collection, either wet or dry. Wet collection involves spraying into a liquid such as deionised water or a buffer solution that is held within a grounded container[42, 49, 57]. A magnetic stirrer may also be used to avoid agglomeration of the particles[42].

Dry collection simply involves spraying directly onto a grounded dry substrate, often aluminium foil. In some cases, a heat plate may be used to increase solvent evaporation from the collected particles[112]. However, there needs to be a balance between solvent evaporation rate and polymer diffusion rate. If the solvent evaporates too quickly then there is insufficient time for the polymer to diffuse through the shell while it is still liquid and so a porous structure is formed.

Different types of collection were required for different particle analysis methods and these are outlined in section 3.6.

3.2.7 Working Distance

The distance from the needle-tip to the collection substrate is known as the working distance and can range from short distances of a few centimetres[42, 57], to over 20 cm[50]. This represents the drying time for the particles i.e. the time taken to travel from needle-tip to the collection plate is the time that the solvent has to evaporate and leave behind the polymeric particle.

The spray itself may take place in atmosphere and the solvent evaporate as it travels to the collection substrate, or there may be a gas flow applied to increase

solvent evaporation[42, 57, 112] which can be used to decrease the required working distance.

In order to carry out the experiments for this research, the working distance was determined by collecting dry particles at different working distances and measuring the mean diameter. If a larger working distance shows a smaller mean diameter then it can be assumed that the smaller size is due to solvent evaporation i.e. at the shorter working distance the particles were not fully dry. Particles were collected at 25mm and 50mm working distances and the peaks of the particle distribution function was determined by AFM (atomic force microscopy). No significant difference was found between the mean particle height and so a working distance of 25mm was deemed to be sufficient (use of AFM to measure particle size is discussed in more detail in section 3.6.2). The use of the shorter working distance was also preferable as it reduces the particle spread over the collection substrate, making it easier to image more particles at a time with AFM.

3.3 Monitoring Equipment

3.3.1 Visualising the coaxial cone-jet mode

It is important to image the liquid as it exits the needle-tip in order to determine which mode the electrospray is in as the applied voltage is increased. In addition, viewing the needle-tip will reveal any wetting of the needle or bias in the spray which is undesirable.

The electrospray was lit with a ring light (KL 1500 electronic, Schott) and a USB CCD camera (UI-2230SE-C-HQ, iDS) with a zoom lens (ZOOM 125, Optem) and 10x objective lens (M Plan Apo, Mitutoyo).

The ring light helps produce more diffuse lighting and reduce reflection of light off the liquid. A 20x objective lens (M Plan Apo, Mitutoyo) was also tested in order to get a clearer image of the jet and so enable a more accurate measurement of the jet diameter, but the shortness of the focal length meant that the metal housing of the lens itself biased the direction of the spray and so it was not suitable for use.

Initially, the coaxial system was tested with paraffin oil (inner liquid) and ethylene glycol (outer liquid). Fluorescein (Sigma-Aldrich) was dissolved into the ethylene glycol to give a contrast against the paraffin oil to help visualise the coaxial

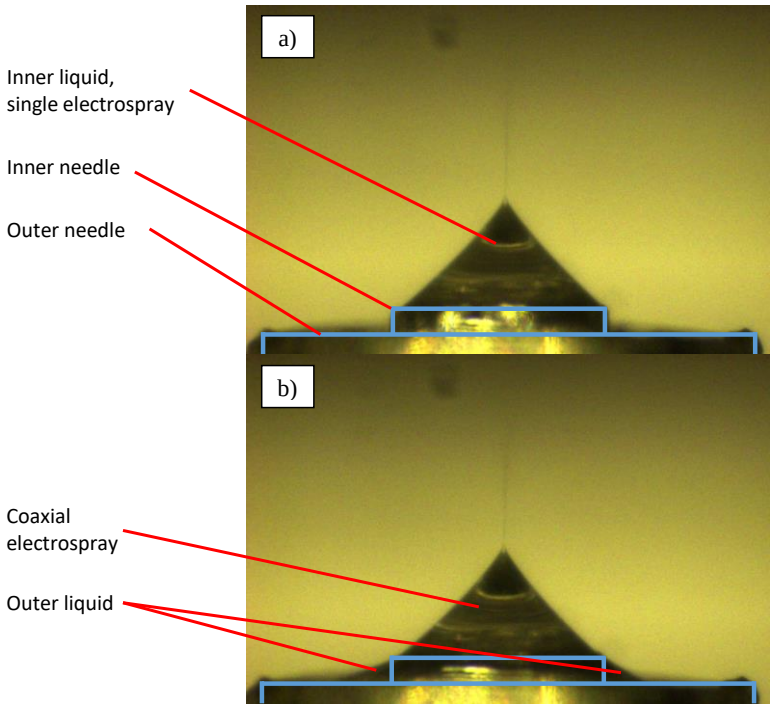

cone-jet. The thickness of the outer liquid in the cone-jet made the interface between the two liquids very easy to identify. However, when the outer liquid was changed to polymer dissolved in a low viscosity solvent, the outer layer became much thinner and the even with fluorescein in the inner liquid, it was not possible to visualise the interface with the camera.

Figure 3.13 a) Start-up with cone-jet of inner liquid only, b) coaxial electrospray where outer liquid can be seen attached to the inner edge of the outer needle

The presence of the coaxial cone-jet was confirmed visually by watching for the single inner cone-jet (Fig. 3.13a) changing to a cone-jet where the outer edge was attached to the inner edge of the outer needle (Fig. 3.13b), after the outer liquid had been introduced into the electrospray system. The jet diameter could also be imaged with the camera to give an idea of the initial wet droplet size prior to solvent evaporation.

3.3.2 Shunt Resistor

A shunt resistor was used to monitor for current fluctuation on the coaxial needle. A 100kΩ resistor was placed in series in the circuit with a voltmeter in parallel. The current could then be calculated by dividing the recorded voltage by 100kΩ. It was used in series with a 1 MΩ resistor to protect the system from any unexpected current surge.

3.3.3 Ambient Conditions

The temperature and humidity are also important factors in electrospray. Changes in temperature can of course affect the properties of any liquids and humidity

also has an effect, particularly on the electrospray of polymers. Moisture in the air reduces solvent evaporation which can have an effect on the working distance requirements and also the morphology of the dried particles. The temperature and relative humidity were both monitored using a temperature and humidity data logger (DT-172, CEM). The temperature could be controlled by the air conditioning in the lab, but the relative humidity could not be – on days of high humidity, it was often difficult to obtain a stable cone-jet. The experiments themselves were all conducted within a fume cupboard (Capitair Flex M391, Erlab).

3.4 Solution Preparation

DNA is a long chain negatively charged polymer which is stable in aqueous phase. However it is not cost-effective to use in the volumes required by this electrospray system purely for characterisation. Therefore it was decided to use carboxymethyl cellulose (CMC) (supplied in its sodium salt form) as a stand-in for DNA. Like DNA, CMC is also a long chain polymer, negatively charged and soluble in water (Fig. 3.14) and far cheaper and available in a greater range of molecular weights compared to other similar negatively charged polymers such as poly(acrylic acid) (PAA)[126], poly(acrylamide) (PAM)[127] or poly(methylacrylic acid) (PMAA)[128].

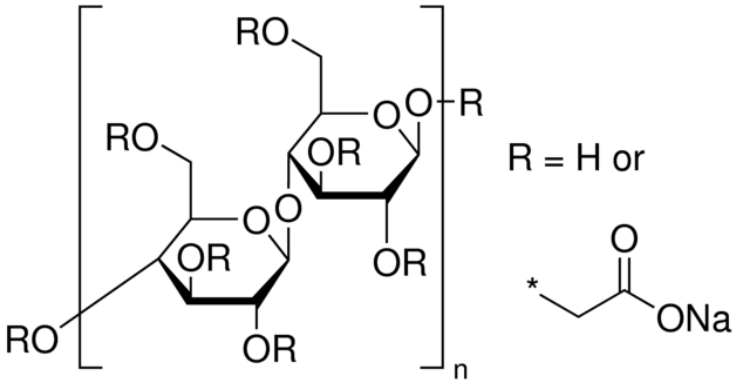

Figure 3.14 Structure of CMC sodium salt

For the block copolymer shell, PLA-PDMAEMA (Fig. 3.15c) was chosen for use and it has been used in previous studies for self-assembled gene delivery systems[129, 130]. PDMAEMA (Fig. 3.15b) is a polycation which has previously been used to complex with DNA[131-134] and is known for its good transfection rate both as a homopolymer[135] and as part of a copolymer[136]. It has previously been used in electrospray as a copolymer but in single electrospray only and not for encapsulation[137]. PLA (Fig. 3.15a) is biodegradable[138, 139] and has been used previously with both single electrospray as a drug carrier[140] and coaxial electrospray for protein encapsulation[141].

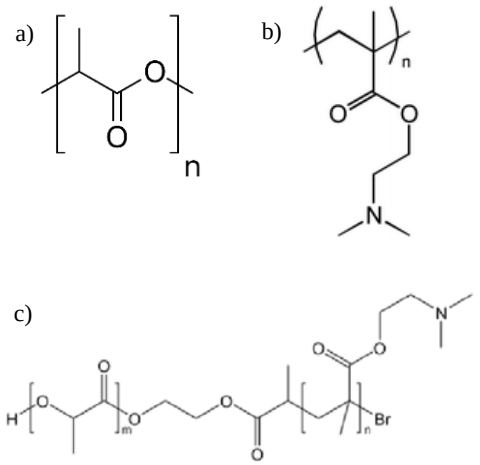

Figure 3.15 a) PLA structure, b) PDMAEMA structure, c) PLA-PDMAEMA structure

The inner liquid was composed of CMC (Mw 90,000, Sigma-Aldrich or Mw 250,000, Aqualon) dissolved at a concentration of 100 µg/mL in a mixture of deionised water (80%) and ethanol (20%). Deionised water is known to be difficult to achieve cone-jet mode with, as its high surface tension means it has a tendency for electrical discharge[142]. Ethanol was therefore added to the inner liquid to reduce the surface tension and so improve the ease of electrospray.

The outer liquid was composed of the outer polymer (either PDMAEMA or PLA13-PDMAEMA22) dissolved in mixture of chloroform (80%) and dimethylformamide (DMF) (20%) at 1 mg/mL. Chloroform has been used previously with polymers for electrospray[143] and has a high solvent evaporation rate. The DMF was used as a cosolvent to induce slight miscibility with the inner liquid in order to prevent the outer polymer from precipitating at the needle-tip[144].

Both liquids were degassed in a sonic bath (FB15051, Fisherbrand) at ambient temperature for 30 min before use.

3.5 Electrospray Experimental Procedure

The liquids were prepared, degassed and loaded into syringes. The inner liquid was pushed manually through the feedline and examined to ensure there were no air bubbles present. The feedline was connected to the coaxial needle, and air was blown through the outer needle while the applied voltage to the extractor was turned on to prevent the possibility of any needle wetting. The inner liquid pump was started and the extractor voltage was increased until the liquid was dripping with the droplets pulled directly down from the needle.

Voltage was applied to the needle until the inner liquid reached cone-jet mode. The flow rate and needle applied voltage were then stopped and the outer liquid connected with the outer feedline filled. The pumps for both liquids were then restarted and the applied voltage to the needle turned on. When the outer liquid had filled the outer needle, it was drawn over the cone-jet of the inner liquid and the coaxial cone-jet was established.

The flow rates used were 0.2 mL/h for the inner liquid and 0.1 mL/h for the outer liquid. The inner flow rate was determined by running the inner liquid in single electrospray and increasing the flow rate until a stable cone-jet for 30 min could be achieved. The outer liquid was then added and the flow rate again increased until a stable coaxial cone-jet could be maintained.

3.6 Particle Characterisation Methods

3.6.1 Particle Composition

The composition of the particles was analysed by Fourier transform infrared spectroscopy (FTIR) using an attenuated total reflectance (ATR) accessory (Fig. 3.16). Samples are analysed by a totally internally reflected infrared beam that passing through a crystal in contact with the sample. An evanescent wave that protrudes slightly (0.5-5um) into the sample, is set up by the total internal reflectance. Changes (attenuations) to the beam, caused by absorption by the sample, are measured by a detector when the beam exits the crystal. This gives an interferogram of the initial beam and attenuated beam which undergoes a Fourier transform to give the infrared spectrum of the sample.

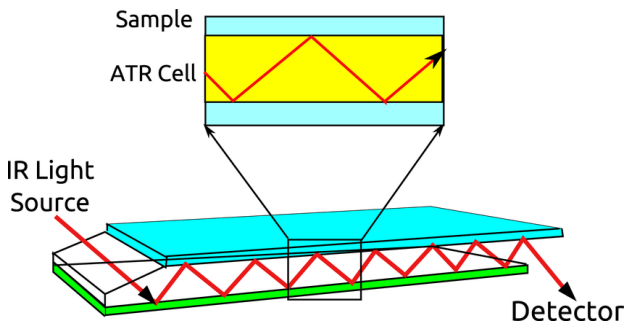

*Figure 3.16 Diagram illustrating the totally internally reflected infrared beam passing through the ATR crystal (Misra, N.N., Sullivan, C. & Cullen, P.J., Current Biochemical Engineering **2**, 4-16 (2015)[145])*

The spectra of individual polymers were analysed first and characteristic peaks were identified that could be used to identify the presence of each polymer in the spectra of

the coaxially electrosprayed particles. Comparison with spectra of self-assembled particles of varying polymer ratio allowed for the creation of a calibration curve. This could be used to calculate the polymer ratio of electrosprayed particles and check if the ratio in which the polymers were electrosprayed had been conserved.

For FTIR analysis the collection method was on aluminium foil wrapped around a glass slide for stability. From a variety of samples with different spray times, a spray time of 20 min was found to give a good spectra.

3.6.2 Particle Size

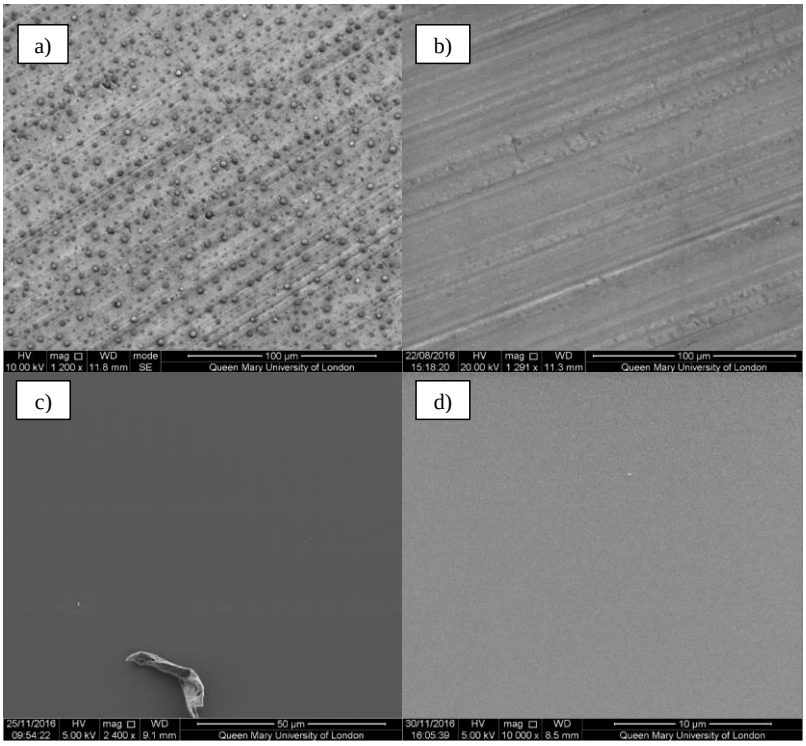

Figure 3.17 a) SEM image of dry collection on aluminium foil, b) SEM images of aluminium foil c) blank gold-coated silicon wafer with smooth appearance, d) blank gold-coated silicon wafer with rough appearance

A number of methods were used to measure particles size as they each have their own drawbacks. Initially scanning electron microscopy (SEM) was used for particle sizing, with dry collection initially on foil (Fig. 3.17a). However, the rough surface of foil (Fig. 3.17b) made image analysis difficult and so the collection substrate was changed to gold-coated silicon wafer. This again presented its own problems as the gold-coating did not always give a smooth surface (Fig. 3.17c & d).

Atomic force microscopy (AFM) was considered next. A piezoelectric crystal is used to oscillate a cantilever near its resonant frequency. When the tip is close to the sample surface, the amplitude of oscillation decreases due to interaction with the sample. When the amplitude changes, the height of the cantilever is automatically adjusted through a feedback loop to return the oscillation to its original amplitude. The movement of cantilever is tracked by a laser which reflects off the back of the cantilever onto a photodiode detector (Fig. 3.18). This allows for the topography of a sample to be imaged.

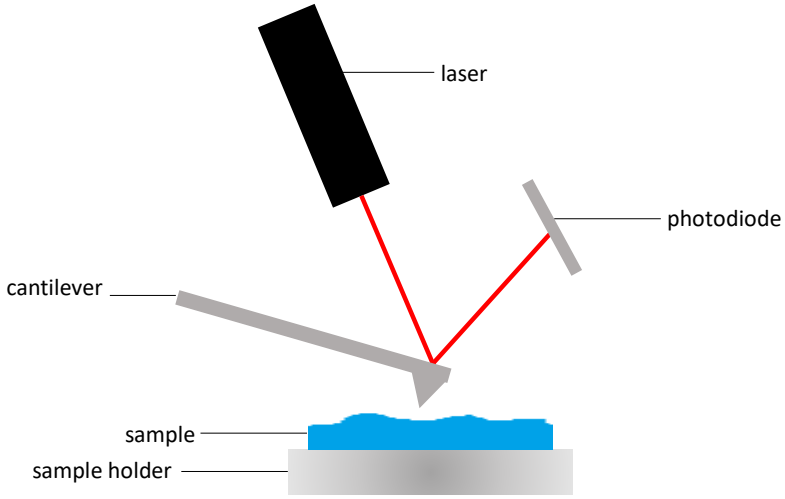

Figure 3.18 Diagram showing the laser which reflects off the cantilever in, allowing the motion to be detected by the photodiode in order to image the topography of the sample

While for SEM, the particle size can be measured from the diameter of imaged particles, for AFM the geometry of the cantilever tip used to determine the topography of the sample can lead to particle diameter being measured as larger than they actually are. As can be seen from Fig. 3.19, while data is collected based upon the position of the cantilever tip, it is in fact the sides of the cantilever tip that contact the particle. Therefore when measuring the diameter of nanoparticles that are assumed to spherical, it is common practice to take the maximum peak height of a particle as the diameter[146, 147].

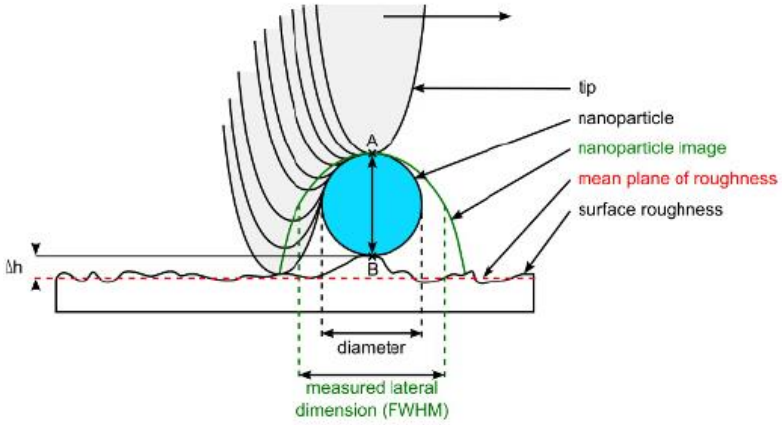

Figure 3.19 Diagram demonstrating how tip geometry leads to a horizontally measured particle diameter that is greater than the actual particle diameter. Measuring the diameter vertically, i.e. via the maximum peak height of a particle, gives a more accurate measurement. (Delvallée, A., Feltin, N., Ducourtieux, S., Trabelsi, M. & Hochepied, J.-F. International Congress of Metrology, 06007 (2013)[146])

Like SEM, AFM requires the use of dry samples. For electrosprayed samples, the particles were sprayed directly onto silicon wafer for 3 min, where the spray time was determined by comparing samples that had been sprayed for 3, 5 and 10 min. The sample density of 3 min was considered to give the best sample density for image

processing. For self-assembly, particles were made up in aqueous phase, the solution was dropped onto silicon wafer and left to dry in ambient conditions.

The zetasizer was also used to size particles in suspension. The zetasizer uses a technique known as dynamic light scattering to calculate the radius of suspended particles based upon their motion which is detected by a laser shone through the sample. Particles suspended in solution undergo random motion known as Brownian motion which can be modelled with the Stokes-Einstein equation. Based upon their motion and other parameters in the equation, the hydrodynamic radius of the particle is calculated - that is the radius of a solid spherical particle that would move in the same way under the same conditions.

For collection, electrosprayed particles were sprayed into a petri dish of grounded deionised water for 30 min, and bulk-assembled complexes were assembled at pH 7 in deionised water.

3.6.3 Particle Structure

Particle structure was analysed by transmission electron microscopy (TEM) (Fig. 3.20). Optical microscopy resolution is limited by the wavelength of light. Electron miscroscopy is able to achieve much higher resolution due to the much smaller wavelength of an electron. TEM generates a beam of electrons which is then

accelerated through an applied voltage and focussed by condensers by means of an applied magnetic field which exerts a force on the electrons.

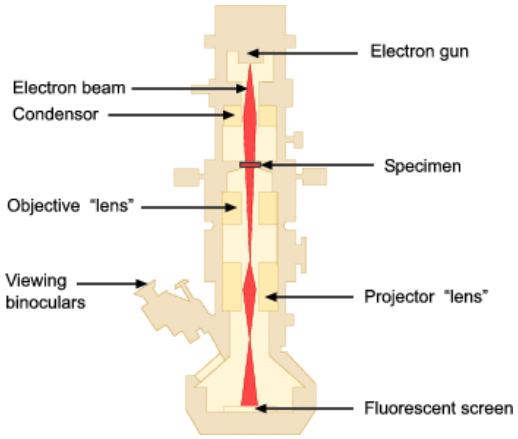

Figure 3.20 Diagram of TEM showing the path of the electron beam through the microscope (Ali, M., (Suez University, 2015)[148])

Images are created by electrons passing through the sample and striking a phosphor screen which is detected by a charged-couple device (CCD). Where more electrons pass through the sample, more light is detected from the phosphor screen leading to contrast in the image. Electron dense parts of the sample appear darker as fewer electrons are able to pass through.

For electrospray sample collection, dry collection of 2 min spray time onto 300 mesh copper TEM grids (Agar Scientific) was used. For bulk-assembled samples, particles were assembled in aqueous phase, dropped onto TEM grids and left to dry overnight in ambient conditions. In both cases, the inner phase was stained with silver ions to increase electron density and so provide better contrast against the shell polymer. For electrosprayed particles, to prepare the inner liquid, 100 µg/ml of CMC

was incubated for 1 h with 25 µg/ml of silver nitrate in a solution of 80% deionised water and 20% ethanol. The particles were fabricated as detailed in section 4.2.4 and sprayed directly onto a TEM grid for 3 min. In the case of self-assembly, 500 µg/ml of CMC was incubated for 1 h with 125 µg/ml of silver nitrate in deionised water. The particles were bulk assembled in solution, and the solution dropped onto a TEM grid and left to dry in ambient conditions.

3.6.4 Zeta Potential

Particle charge was measured by zeta potential (Zetasizer Nano ZS, Malvern), which is a measure of the charge that develops at the interface between a sample and the liquid it is suspended in. When a particle in is solution, an electric double layer is formed on the particles surface. The surface charge attracts ions of the opposite charge which are tightly bound to the surface - the Stern layer, and this layer in turn attracts ions which are more loosely bound - the diffuse layer. The zeta potential is a measure of charge taken at the slipping plane which lies at the boundary between the diffuse layer and the bulk suspending liquid.

To measure the zeta potential, the suspended sample is placed in a zeta cell (Figure). A charge is applied across the cell and the motion of the particles is detected by a laser, as with particle sizing. Based upon the particle velocity under an applied electric field of known strength the zeta potential of the particles can be calculated.

Zeta potential requires samples to be suspended in an ionic solution. Electrosprayed samples were sprayed into 1 mL of 10 mM NaCl (sodium chloride) for 30 min to achieve a weight concentration of 60 µg/mL, above the 10 µg/mL minimum recommended by the instrument manufacturer. Self-assembled particles

were assembled in deionized water for a weight concentration of 350 µg/mL. 0.1 mL of this solution was added to 0.9 mL 10 mM NaCl to give a final weight concentration of 50 µg/mL.

Chapter Four

Particle Characterisation

4.1 Introduction

Self-assembly is a process by which molecules can form organised structures through interactions based upon their inherent characteristics such as charge or hydrophobicity, rather than being 'built' through external guidance. It is a commonly used method for creating core-shell structure polymer capsules[88, 89, 104, 149]. Although coaxial electrospray in principle allows the structuring of two phases into a core-shell particle, a comparison with bulk-assembled complexes may allow us to see whether any interaction takes place between the core and shell polymer during the electrospray process.

In this chapter, bulk-assembled complexes are produced at varying pH as the encapsulated (CMC) and encapsulating polymer (PDMAEMA) are weak polyelectrolytes displaying pH-responsive behaviours[150-155]. Hence characterisation of the resulting particles would allow to determine the impact of pH-associated changes in the conformation of these electrolytes on the interfacial assembly of the nanomaterials.

Coaxially electrosprayed particles are characterised by their chemical composition, size and structure. In terms of the chemical composition, FTIR

spectroscopy is used to identify the presence of both polymers and estimate their respective ratios.

The mean particle size is assessed by AFM and DLS, particle structure is imaged by TEM and zeta potential measured. These characteristics are then compared with those of particles directly self-assembled from the bulk.

4.2 Materials and Methods

4.2.1 Materials

The polymers used were sodium carboxymethyl cellulose (CMC) and poly[2-dimethylamino)ethyl methacrylate] PDMAEMA. CMC (Mw 90,000) was obtained from Sigma-Aldrich, and PDMAEMA was synthesised by Dr Danyang Li (QMUL). Solvents used were chloroform, dimethylformamide (DMF) and ethanol, all obtained from Sigma-Aldrich and used as received.

4.2.2 CMC Protonation

CMC was dissolved in deionised water to form a 500 µg/mL solution. From this two solutions further were made, one with the pH decreased with hydrochloric acid (HCl) to protonate the CMC, one with the pH increased by sodium hydroxide (NaOH) to deprotonate the CMC.

4.2.3 Fabrication of Bulk-Assembled Complexes

CMC was dissolved in deionised water to form a 500 µg/mL solution and PDMAEMA was dissolved in deionised water to form a 500 µg /mL solution. These

solutions were then mixed in a 1:5 volumetric ratio (CMC:PDMAEMA) and left to incubate for 1 h, forming a suspension of bulk-assembled polyelectrolyte complexes. Appropriate volumes of HCl or NaOH were added to the solutions prior to mixing in order to obtain three solutions at different pH (pH 5, pH 7 and pH 11). The samples were then freeze-dried and the precipitate collected for FTIR analysis.

4.2.4 Fabrication of Electrosprayed Particles

The electrospray apparatus used was as outlined in Fig. 3.1. The inner liquid was formed of CMC dissolved in a mixture of 80% deionised water and 20% ethanol at a concentration of 100 µg/mL. The outer liquid was formed of PDMAEMA dissolved in a mixture of 80% chloroform and 20% DMF at a concentration of 1 mg/mL. The liquids were sprayed separately in single electrospray at the onset voltage for cone-jet mode (5-6 kV) with a suitable extractor voltage (1-1.5 kV). The liquids were also sprayed coaxially in cone-jet mode, with the inner liquid at a flow rate of 0.2 mL/hr and the outer liquid at 0.1 mL/hr. The particle collection was dependent on the method of particle characterisation.

4.2.5 Fourier Transform Infrared Spectroscopy

Attenuated total reflectance Fourier transform infrared (ATR-FTIR) spectroscopy (Tensor 27, Bruker) was used to characterise the molecular structure and composition of the polymers in solid form, freeze-dried residue of bulk-assembled complexes at varying pH, and dry polymer particles from single and coaxial electrospray which were collected on aluminium foil for 20 min and dried in a vacuum oven at 40°C overnight. The liquids for electrospray were prepared as detailed in the

previous chapter (section 3.4) and the flow rates used were 0.2 mL/h for the inner liquid and 0.1 mL/h for the outer liquid.

4.2.6 Dynamic Light Scattering

Dynamic light scattering (DLS) (Zetasizer Nano ZS, Malvern) was used to determine the hydrodynamic diameter and measure the zeta potential of bulk-assembled complexes and electrosprayed particles. Electrosprayed particles were sprayed into grounded deionised water for 30 min and grounded 10 mM NaCl for 30 min for sizing and zeta potential measurements respectively. Bulk-assembled complexes were assembled at pH 7 in deionised water for sizing and in 10 mM NaCl for zeta potential measurements.

4.2.7 Atomic Force Microscopy

AFM (NTegra, Bruker) was used with silicon cantilever probes (RTESP-300, Bruker) which were plasma-treated to render them hydrophilic and prevent particles adhering to them. Electrosprayed particles were collected on silicon wafers for 3 min, and bulk-assembled complexes were generated in deionised water and dropped onto silicon wafers at low concentrations (to prevent aggregation) and left to dry in ambient conditions.

AFM was performed in semi-contact or tapping mode and images were acquired with NOVA software where preliminary image processing was performed to flatten the images. Further image processing was performed in MATLAB. A script was written to threshold images to remove noise caused by surface roughness, identify centroids and give the diameter and maximum peak height of each centroid[146]. The images were then examined by eye to remove any obvious non-rounded shapes that

were likely debris, aggregation or a particle dragged along the wafer. Furthermore, any particles which were only 9 pixels in size were considered too small to be analysed accurately and were therefore discounted.

4.2.8 Transmission Electron Microscopy

TEM (JEOL 2010, JEOL Ltd.) was used to image electrosprayed particles and bulk-assembled complexes. The inner phase was stained with silver ions to provide better contrast against the shell polymer. For electrosprayed particles, to prepare the inner liquid, 100 µg/ml of CMC was incubated for 1 h with 25 µg/ml of silver nitrate in a solution of 80% deionised water and 20% ethanol. The particles were fabricated as detailed in section 4.2.4 and sprayed directly onto a TEM grid for 3 min. In the case of self-assembly, 500 µg/ml of CMC was incubated for 1 h with 125 µg/ml of silver nitrate in deionised water. The particles were bulk assembled in solution as in section 4.2.3, and the solution dropped onto a TEM grid and left to dry in ambient conditions.

4.3 Results and Discussion

4.3.1 Particle Composition

First the composition of the particles was established through FTIR spectra analysis. Individual polymers were examined first to determine which peaks could be used to identify them when combined within bulk-assembled complexes or electrosprayed particles.

4.3.1.1 Single Polymer Analysis

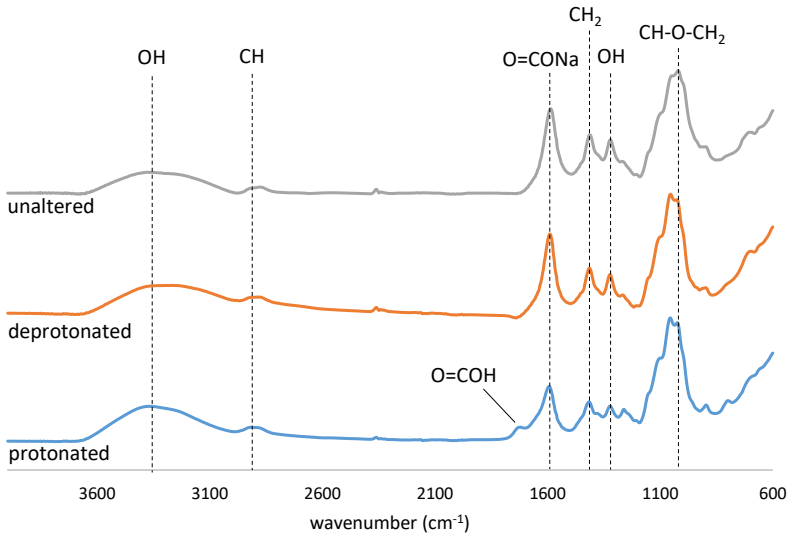

Figure 4.1 Normalised FTIR spectra of solid CMC, freeze-dried deprotonated and protonated CMC samples

FTIR spectra (Fig. 4.1) were taken of freeze-dried residue from solutions of protonated and deprotonated CMC and compared with that of solid CMC. There are two broad peaks and four better resolved peaks that can be identified. From comparison to the literature, the large shallow peak at around 3300 cm^{-1} can be

attributed to –OH stretch[156, 157], the small peak around 2900 cm^{-1} can be attributed to C-H[98, 158], the peak around 1590 cm^{-1} can be attributed to the C=O in the carboxyl group[156, 159], the peak around 1410 cm^{-1} can be attributed to the methyl group ($-CH_2$)[156, 160], the peak around 1310 cm^{-1} can be attributed to –OH[156, 157], and the peak at around 1050 cm^{-1} can be attributed to CH-O-CH_2 stretching[157, 160]. Confirmation of the carbonyl peak at 1590 cm^{-1} can be seen by comparison between the protonated and unaltered CMC spectra. The protonated spectra shows the appearance of a peak at 1718 cm^{-1} and a decrease in the O=CONa peak intensity relative to the other three main peaks. This is in agreement with the reported shifted observed for carboxylic acids and corresponding conjugated bases[159]. During the freeze-drying process protonation is expected due to increase in acidity[161]. However, in the deprotonated spectra a protonated peak at 1718 cm^{-1} cannot be seen, indicating that the degree of protonation is insufficient to be detected.

FTIR spectra were then used to identify unique peaks from each polymer in the bulk-assembled complexes and electrosprayed particles in order to confirm that both the inner and outer polymer were present. First, spectra of the individual

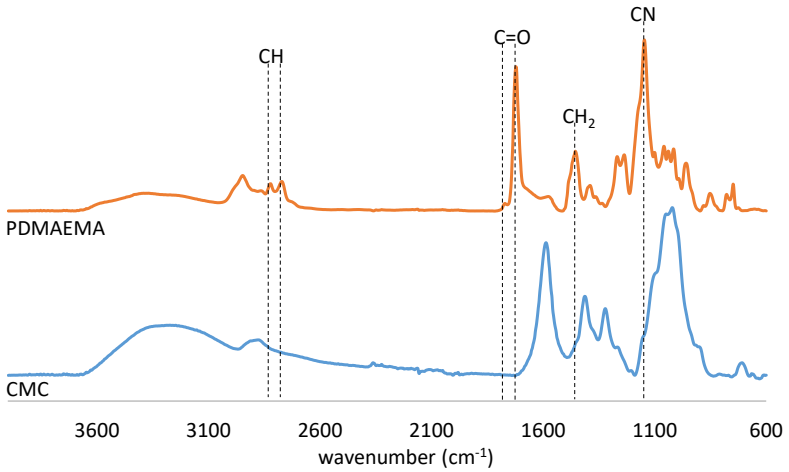

polymers were taken to find unique peaks which could be used to confirm the presence of each polymer from the spectra of particles where both were used (Fig. 4.2).

Figure 4.2 Spectra of PDMAEMA and CMC in solid form

For the PDMAEMA, peaks from the C-H in the amine groups can be seen at 2821 cm^{-1} and 2771 cm^{-1} [162]. The other identifying peaks are at 1772 cm^{-1} and 1722 cm^{-1}, both attributed to C=O of the ester, the peak at 1456cm^{-1} is attributed to the CH_2 group and at 1146 cm^{-1} there is a peak attributed to the C-N group[162-164]. Comparing the normalised spectra for PDMAEMA and CMC, it can be seen that CMC has a strong peak at 1595 cm^{-1} from the carbonyl group, where PDMAEMA has a small background signal and CMC also has a unique peak at 1310 cm^{-1} from the hydroxyl group, where again there is very little signal in the PDMAEMA spectra. Therefore, although the separation of these peaks is not perfectly resolved, these can be regarded as two key peaks to look for when confirming the presence of CMC in electrosprayed particles and bulk-assembled complexes.

4.3.1.2 Deciding the CMC:PDMAEMA Weight Ratio

As FTIR spectra were used to confirm the presence of both polymers in the electrosprayed particles and bulk-assembled complexes, it was important that the weight ratio of polymers used was one that allowed the peaks of both polymers to clearly visible on the same spectra.

Initially a weight ratio of 1:20 of CMC:PDMAEMA was used in the electrospray in the interests of using low flow rates to achieve particles of small diameter. However, from the spectra of the electrosprayed particles it was apparent that the identifying peaks of CMC could not be clearly distinguished from those of

PDMAEMA. The ratio of CMC:PDMAEMA was changed to 1:5 by and in this spectra, the emergence of a peak at 1600 cm^{-1} relating to the carbonyl of the CMC becomes obvious (Fig. 4.3). Therefore, the ratio of 1:5 was kept as the default ratio to use in both electrospray and self-assembly for easy confirmation of CMC presence.

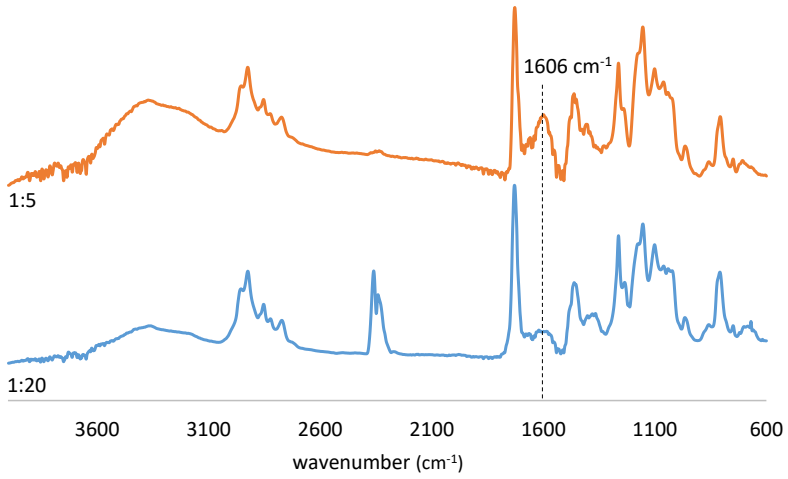

Figure 4.3 FTIR spectra of electrosprayed particles of CMC:PDMAEMA in ratios of 1:5 and 1:20 where samples were allowed to air dry. The peaks around 2300 cm^{-1} can be ignored as they are related to atmospheric carbon dioxide.

The large broad peak that can be seen between 3600 cm^{-1} and 3000 cm^{-1} indicates –OH groups, arising from the presence of water as well as hydroxyl moieties in the CMC structure. To reduce the component due to residual solvent/water, it was decided to dry samples in a vacuum oven (Fig. 4.4). A reduction in the large OH peak around 3300 cm^{-1} can be seen suggesting the removal of water and also new strong peaks at around 1260 cm^{-1} and 810 cm^{-1} can clearly be seen, neither of which can be seen in the spectra for the individual polymers in solid state (Fig. 4.2).

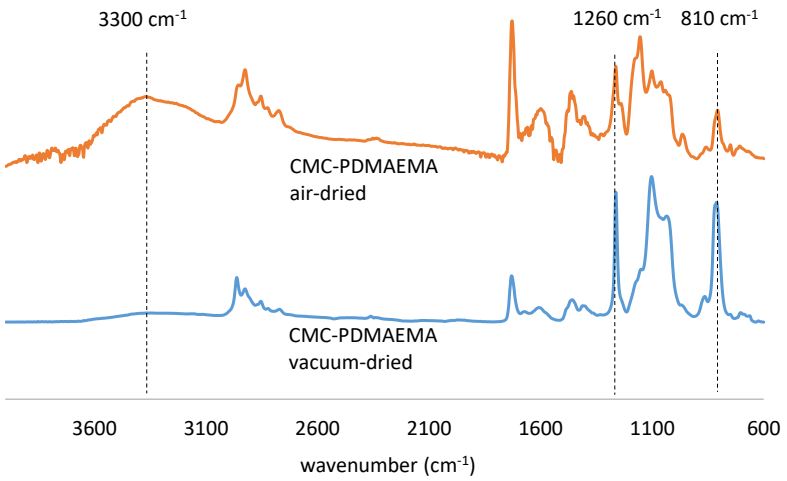

Figure 4.4 FTIR spectra comparison of electrosprayed particles following air-drying at ambient conditions and vacuum-drying overnight

These new peaks could result from residual higher boiling point solvents introduced in the electrospray system that are not completely removed through drying in the vacuum oven. Looking at spectra for the individual solvents, both chloroform and DMF show a sharp peak at ~1250 cm^{-1}, and chloroform also shows a very strong, broad peak between 700-800 cm^{-1} [165, 166]. For the inner liquid, ethanol shows a distinct peak around 800 cm^{-1} and another around 1270 cm^{-1} [167]. Chloroform is known to remain in polymeric microspheres even after vacuum-drying[168-170] and so it is possible the peaks are from residual chloroform.

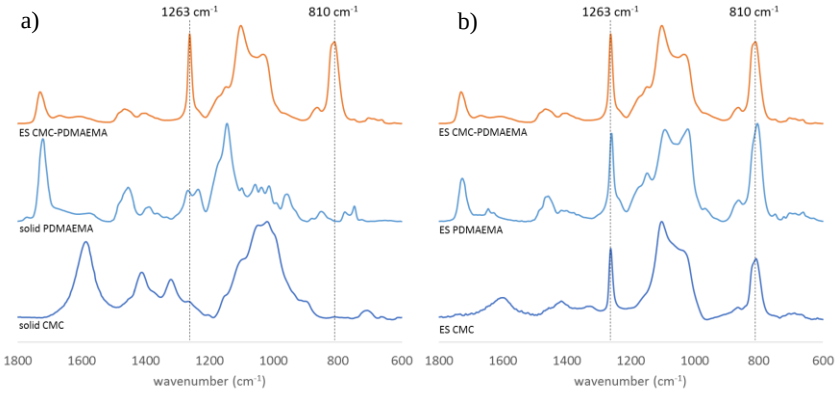

Figure 4.5 FTIR spectra comparison of electrosprayed (ES) CMC-PDMAEMA with a) solid polymers and b) single electrosprayed polymers

A comparison between the spectra of the coaxially electrosprayed CMC-PDMAEMA, the single-sprayed polymers and polymers in solid state reveals that the appearance of the sharp peaks at 1263 cm^{-1} and 810 cm^{-1} only occurs with single electrosprayed polymers (Fig. 4.5b) as these peaks are not present in the spectra of the individual solid polymers (Fig. 4.5a). Therefore, for comparison with coaxially electrosprayed particles, it was decided that the spectra of single electrosprayed polymers should be used as opposed to the spectra of solid polymers.

4.3.1.3 Self-Assembly with Varying pH

As pH-responsive polymers are being used, bulk-assembled complexes were made at varying pH conditions in order to establish the effect that pH has on particle size and composition. PDMAEMA and CMC were dissolved in aqueous phase at different pH (pH 5, pH 7 and pH 11) and then mixed to form bulk-assembled complexes in a 1:5 (CMC:PDMAEMA) weight ratio, as established previously (Fig. 4.3), to allow for the confirmation of CMC presence via FTIR spectra.

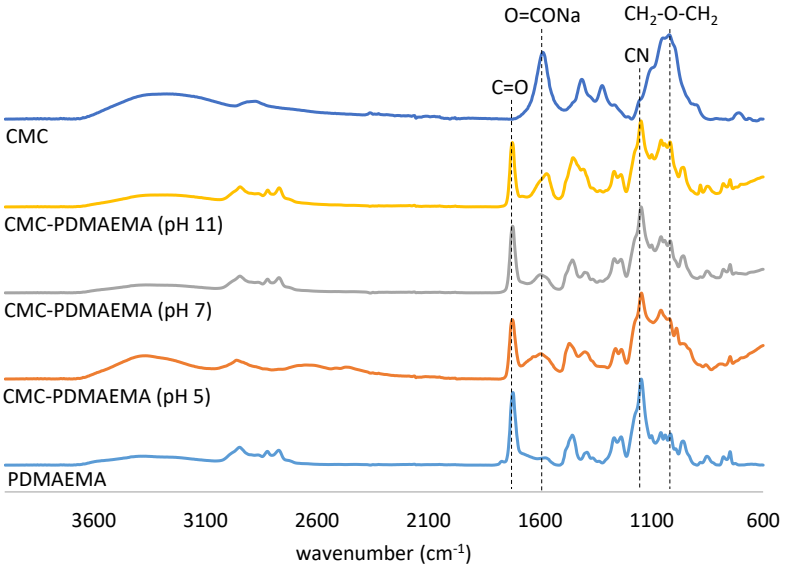

Figure 4.6 FTIR spectra of bulk-assembled complexes of CMC-PDMAEMA prepared in aqueous phase in a 1:5 weight ratio at varying pH (pH 5 in orange, pH7 in grey, pH 11 in yellow) shown with the spectra of the solid individual polymers for comparison (PDMAEMA light blue, CMC dark blue). In all three cases, the peak around 1600 cm^{-1} (carbonyl of CMC) can be seen signifying the presence of CMC.

In all pH conditions, it is possible to see the presence of CMC confirmed by the appearance of the carbonyl peak at around 1600 cm^{-1} (Fig. 4.6). At pH 11, a shift to a lower wavenumber can be seen in the 1600 cm^{-1} peak indicating deprotonation of the carbonyl group. This indicates that the CMC at this pH may be more swollen than at the other pH conditions due to electrostatic repulsion between the deprotonated groups.

Next the complexes are sized to give further insight into the effect that the different pH conditions have on polymer interaction during bulk-assembly.

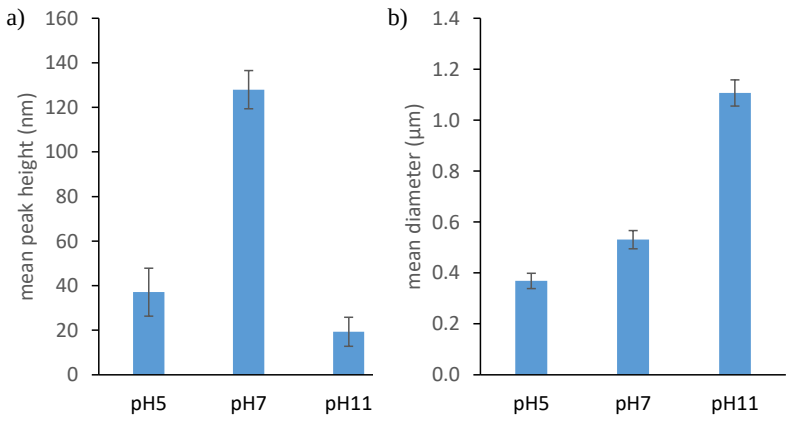

Figure 4.7 Comparison across a range of pH for bulk-assembled complexes showing a) mean peak height and b) mean diameter obtained via AFM (shown with standard error) (n= 27, 43 and 24 for pH 5, 7 and 11 respectively)

The mean peaks heights for bulk-assembled complexes seem to show pH 7 gives the largest particles (Fig. 4.7). Although the lateral diameter measured through AFM cannot be used as a measure of actual particle diameter[146, 147], it can be seen that the trend in diameter with pH is markedly different. This may indicate particle instability during the drying process or perhaps important changes in the mechanical properties and hydrophobicity of the resulting complexes, assembled at different pH. In self-assembled polyelectrolyte multilayer films, it has been seen that altering the pH can affect the film thickness and stiffness[171-173].

~~Complexes assembled at high pH are also expected to be more hydrophobic,~~ . Additionally, as the water evaporates during sample drying process, the pH of the remaining solution will be increasing leading to an increase in protonation and the pH at which the sample is finally dried cannot be known for certain. In any case, it can be concluded that AFM

is not a suitable method for measuring bulk-assembled complex size as the stability of the dried complex is unknown. Therefore DLS was used to examine bulk-assembled complex size (Table 4.1). These results show that pH 11 gives by far the largest sized complexes, over 1 μm in diameter, which could arise from the relatively hydrophobic nature of PDMAEMA at this pH and the aggregation of several complexes. pH 5 gives the next smallest complexes with a diameter of 214.1 nm, and pH 7 gives the smallest complexes with a diameter of 165.9 nm, perhaps due to the stronger electrostatic charge on both polymers at this pH. The PdI (polydispersity index) of pH 7 is also lower than that of pH 5 (0.44 and 0.39 respectively).

pH	Mean diameter (nm)	Std. Dev.	PdI	Std. Dev.
5	214.1	26.0	0.444	0.025
7	165.9	6.864	0.392	0.015
11	1364	30.66	0.474	0.372

Table 4.1 Comparison of hydrodynamic diameter and polydispersity index across different pH for bulk-assembled CMC-PDMAEMA complexes

The change in complex size with pH, can be attributed to a change in behaviour of CMC and PDMAEMA; they are both pH-responsive polymers and as such will release or accept protons depending on the pH of their environment. CMC is a carboxylic acid with a pKa value between 4 and 5[174, 175] , is most negative at pH 7 and above[150, 151], and undergoes swelling at high pH[176, 177]. This is due to the deprotonation of the carboxylic acid groups (as seen in Fig. 4.5), leading to electrostatic repulsion between these groups and so an increase in the size of the CMC.

PDMAEMA is a cationic polymer with a pK_a value between 7 and 8[178, 179] and undergoes swelling at low pH. PDMAEMA contains a tertiary amine group that is protonated at low pH and so the increase in electrostatic repulsion between these protonated groups leads to swelling. With this in mind, the size increase at pH 11 could be attributed to CMC swelling and the size increase at pH 5 could be attributed to a combination of PDMAEMA swelling and reduced negative charge of the CMC.

It can be concluded that the greater negative charge of the CMC at pH7 is promoting a stronger interaction with the cationic PDMAEMA (at this pH), which leads to a smaller mean particle size and less polydispersity. Lin et al. formed bulk-assembled complexes of PDMAEMA with DNA and saw a mean size of 230 nm at pH 7 and 115 nm at pH 5[180]. This was determined to be due to the stronger positive charge of PDMAEMA at lower pH[181]. DNA also has a lower pKa than CMC and so is more negatively charged than CMC at lower pH 5[182]. Stolnik et al.[181] looked at bulk-assembled complexes of DMAEMA and plasmid DNA (pDNA) and were able to achieve complex sizes of around 100 nm at a variety of pH (pH 4-8), but the optimum pH for the smallest size complex was dependent on the ratio of DMAEMA to pDNA. When the ratio of DMAEMA to pDNA was higher, a lower pH (4-6) was more favourable for producing smaller complexes and when the ratio was lower, a higher pH (7) was better. The ratio of polymers in Table 4.1 is 1:5 CMC:PDMAEMA which indicates that a lower pH is better, but the optimum pH is not as low as that as used with pDNA due to the higher pKa of CMC.

The use of pH 7 also helps to strike a balance between the swelling of both polymers which again helps to reduce the size. It therefore follows that, while the degree of polymer interaction that takes place during electrospray is not known at this

point, it is prudent to have the CMC, i.e. the inner liquid, at pH 7 to reduce CMC swelling and give a greater negative charge.

4.3.1.4 CMC Content of Electrosprayed Particles

A comparison of peak ratios between CMC-PDMAEMA electrosprayed particles and bulk-assembled complexes showed a similar trend in ratios between peaks and therefore a calibration curve was made to try to quantify the proportion of CMC present in the electrosprayed particles.

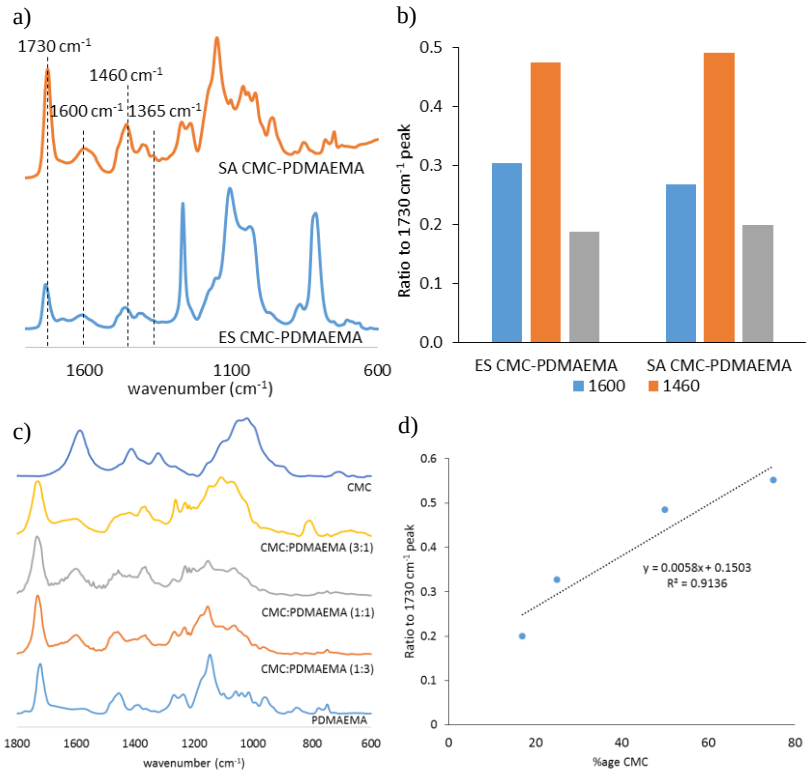

Figure 4.8 a) FTIR spectra comparison of identifiable peaks from electrosprayed particles (inner flow rate 0.2mL/h, outer flow rate 0.1 mL/h) and bulk-assembled complexes of CMC-PDMAEMA with a polymer weight ratio of 1:5 (CMC:PDMAEMA) in both cases, b)

corresponding ratios to the 1730 cm^{-1} peak, c) comparison of FTIR spectra from bulk-assembled CMC-PDMAEMA complexes in various ratios (denoted in brackets), and d) calibration curve of ratios of 1365 cm^{-1} to 1730 cm^{-1} peak relative to CMC percentage.

The calibration curve was made by comparing peak ratios over three different bulk-assembled complexes of CMC-PDMAEMA at pH 7 (prepared in ratios of 1:5 (spectra shown in Fig. 4.6), 1:3, 1:1 and 3:1 (Fig. 4.8c).

The 1730 cm^{-1} peak was used as the standard peak for comparison as there is no contribution from CMC around that wavenumber. The peak at 1365 cm^{-1} was selected for comparison as it is a peak that has been identified where little contribution is expected from PDMAEMA (Fig. 4.78b). The three ratios were used to form a calibration curve of peak ratio vs CMC percentage in particle (Fig. 4.8d). The R^2 value (0.91) shows a good linear correlation, and the calibration curve gives the 1703:1365 cm^{-1} peak ratio as being 0.25, while the actual peak ratio from the electrosprayed sample is 0.19. This shows that the ratio of polymers is more or less preserved in the particles following electrospray which indicates that the phase composition in electrosprayed droplets is comparable to that of the feed. This could be attributed to the use of DMF, with a high boiling point, in the outer liquid to encourage miscibility[144] so the polymer does not gather at the outer interface between the outer liquid and air.

4.3.2 Particle Sizing

While bulk-assembled complexes are made through electrostatic interaction between the two polymers, the process of particle production in coaxial electrospray is not only dependent upon the interaction between the polymers to form particles, as it is driven by the charged liquids carrying the polymers and solvent evaporation.

Therefore it could be expected that there is a difference between the characteristics of particles made by these two methods.

First the sizes of particle produced by the two methods were compared.

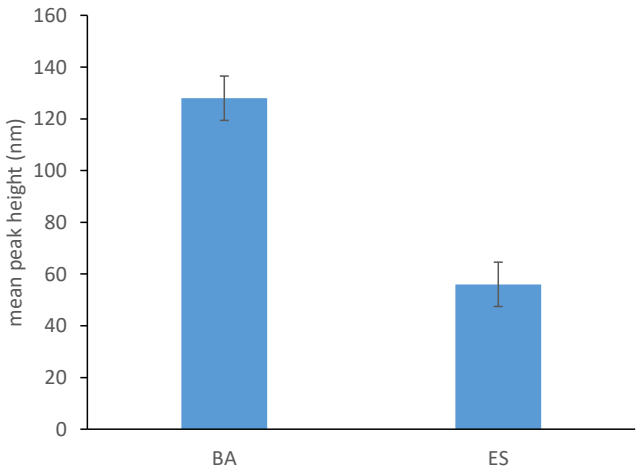

Figure 4.9 Comparison of the mean diameter, obtained through AFM, of bulk-assembled complexes (BA, n=54) and electrosprayed CMC-PDMAEMA particles (ES, n=78) (shown with standard error)

The mean peak height of bulk-assembled complexes and electrosprayed partilces of CMC-PDMAEMA were analysed by AFM and DLS. For AFM, the mean heights were 128 nm and 56 nm for the bulk-assembled complexes and electrosprayed particles respectively (Fig. 4.9), and for DLS the hydrodynamic diameter was 165.9 nm (PdI 0.392) and 117.4 nm (PdI 0.373) for the bulk-assembled complexes and electrosprayed particles respectively (Table 4.2).

Assembly Method	Z-average	Std. Dev.	PdI	Std. Dev.
Bulk-assembly	165.9	6.86	0.392	0.015
Electrospray	117.3	17.94	0.373	0.064

Table 4.2 Comparison of hydrodynamic diameter and polydispersity index (PdI) of bulk-assembled complexes and electrosprayed particles of CMC-PDMAEMA with standard deviation

The AFM data shows the electrosprayed particles to be smaller than the bulk-assembled complexes, but it has already been seen in the previous AFM data (Fig. 4.7), that this method is unreliable when sizing bulk-assembled complexes. The DLS data showed the electrosprayed particles to be smaller than the bulk-assembled complexes, average sizes of 117.3 nm and 165.9 nm respectively. This suggests that the electrosprayed particles would be small enough to successfully enter cells[9, 10].

Wu et al. were able to transfect murine cells (NIH 3T3) with coaxially electrosprayed particles of PEI and pDNA that were around 250 nm in diameter and saw better transfection than bulk-assembled complexes prepared in the same ratios[16]. Looking at the electrospray conditions used, it can be seen that they used higher flow rates (6 mL/h for both inner and outer liquids) which led to a higher polymer throughput – 223.2 µg/h compared to 120 µg/h as used here to form CMC-PDMAEMA particles. In other words, while the scaling laws dictate that the particle size scales with flow rate, the rate of polymer throughput is also an important consideration when electrospraying polymeric particles.

4.3.3 Zeta Potential

Next the zeta potential of bulk-assembled complexes and electrosprayed particles were compared to give an insight into their respective polymer structures.

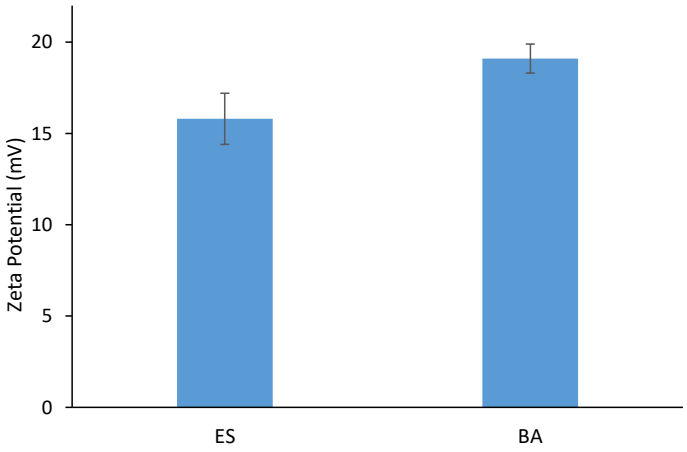

Figure 4.10 Comparison between the mean zeta potential of CMC-PDMAEMA electrosprayed particles (ES) and bulk-assembled complexes (BA) (shown with standard deviation)

The mean zeta potential of electrosprayed particles and bulk-assembled complexes of CMC-PDMAEMA were measured through DLS and were found to be 15.8 mV and 19.1 mV respectively (Fig. 4.10). This confirms the abundance of PDMAEMA with respect to CMC, and suggest that a PDMAEMA shell is observed in both cases due to CMC's negative charge at pH 7[150, 151]. This is expected from the bulk-assembled complexes due to the way in which the particles are formed by electrostatic interaction and the larger quantity of PDMAEMA compared to CMC. The positive charge on the electrosprayed particles is further confirmation that both polymers are being sprayed and suggests that the particles could be uptaken by cells through endocytosis[9]. Lo et al.[183] saw a similar zeta potential for bulk-assembled DNA-PDMAEMA complexes in the same 1:5 ratio (22.4 mV ± 0.8) which implies that these electrosprayed CMC-PDMAEMA particles present a reasonable model for DNA-PDMAEMA if looking at cell uptake based on zeta potential alone.

4.3.4 Particle and Complex Structure

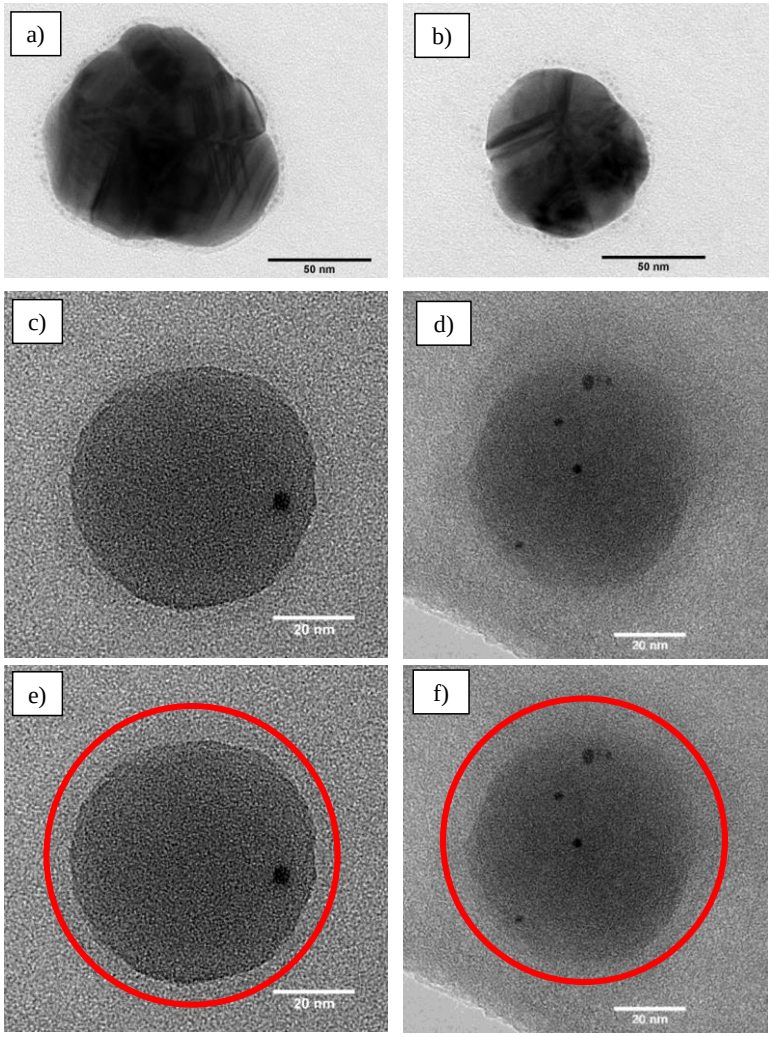

Figure 4.11 TEM images a) & b) show examples of bulk-assembled complexes of CMC-PDMAEMA, c) & d) show electrosprayed CMC-PDMAEMA particles. The dark spots are assumed to be aggregations of silver which were used to stain the CMC to give a greater contrast with respect to neutral or cationic phases such as PDMAEMA. The outlines of outer shells are highlighted in e) & f).

The TEM images of the bulk-assembled complexes (Fig. 4.11a & b), show a core-shell structure but the spotty nature of the shell suggests a relatively inhomogeneous coating. The images of the electrosprayed particle (Fig. 4.11c & d) showed that the particles produced by electrospray do indeed have a core-shell structure. Measurements taken of the shell width gave mean averages of 4 nm (Fig 4.11e) and 7 nm (Fig 4.11f). However, due to time contraints not many particles could be imaged. For a more comprehensive look at particle structure, imaging many particles would help to give an idea of the proportion of particles that show good core-shell structure and poor core-shell structure.

A clear difference is that the contrast between core and shell is far better in the bulk-assembled complexes. This suggests that there is a higher density of CMC than in the electrosprayed particles. This could be due the electrosprayed particles being softer than the bulk-assembled complexes and so flattening as they impact the TEM grid. A more detailed look at the size and deformation of particles following dry collection is carried out in the next chapter.

4.4 Conclusion

From the FTIR spectra of individual polymers, unique peaks with which the presence of both polymers within the produced particles were identified, allowing confirmation of the presence of both polymers in the bulk-assembled complexes and coaxially electrosprayed particles.

From the DLS data of bulk-assembled complexes, it can be seen that while complexation can occur over a range of pH, pH 7 produces the smallest complexes. This change in size is related to CMC swelling at high pH and PDMAEMA swelling

at low pH, CMC being more negatively charged at pH 7 than lower pH values and PDMAEMA being positively charged below pH 7. This also highlighted a difference between CMC and DNA; DNA has a low pKa and is therefore also to produce small complexes at lower pH values than possible with CMC.

The degree of electrostatic interaction between the polymers during particle formation in electrospray is not known, so the extent of the effect of CMC's negative charge on particle size cannot quantified, but it is still advantageous to lessen CMC swelling. Therefore the inner liquid for electrospray was prepared at pH 7.

A calibration curve made through peak ratios from the FTIR spectra of bulk-assembled complexes in different polymer ratios showed that the polymer ratio in which the liquids are supplied by syringe pump is preserved to a very similar degree in the final particles following the electrospray process.

DLS data on particle size shows that the electrospray method produces slightly smaller particles on average and with a slightly smaller PdI. The TEM images show that electrosprayed particles have a core-shell structure and this is backed up by the zeta potential of electrosprayed particles having a positive charge indicating that PDMAEMA is on the outside of the particles. However, the electrosprayed particles appear to be flattened, due to the lower CMC density indicated by the lower core-shell contrast compared to bulk-assembled complexes.

Overall, for CMC-PDMAEMA it would appear that electrospray is able to produce particles that are smaller than those produced through self-assembly, have the desired core-shell structure to protect negatively charged payloads such as DNA and a positive charge which can facilitate efficient cell uptake.

Chapter Five

Effect of Polymer Structure on Electrosprayed Particles

5.1 Introduction

In self-assembly, amphiphilic block copolymers can be used for the encapsulation based upon electrostatic interaction[184, 185]. Having looked at encapsulation with PDMAEMA in the previous chapter, a block copolymer PLA-PDMAEMA will now be used to provide a further point of comparison between self-assembled and electrosprayed particles. PLA-PDMAEMA has been used before by Qian et al.[129] to encapsulate doxorubicin through self-assembly and also by Babikova et al.[186] to encapsulate curcumin but based upon the hydrophobicity of PLA rather than electrostatic interaction with the drug to be encapsulated.

Secondly, the use of sodium hyaluronate (HA) as a DNA substitute will be assessed and compared to CMC. Like CMC, HA has a carboxyl group and low pKa[187] giving it a negative charge at pH 7 which gives it similar properties to DNA. It is also far more cost-effective than DNA to use in large quantities and is therefore another good potential candidate for a DNA model.

5.2 Materials and Methods

5.2.1 Materials

Sodium hyaluronate (HA) (Mw 10,000) was obtained from Lifecore Biomedical. CMC (Mw 90,000) was obtain from Sigma Aldrich and CMC (Mw 250,000) was obtained from Aqualon. PDMAEMA and PLA-PDMAEMA were both synthesised at QMUL by Dr Danyang Li and Dr Zi Zhang respectively. Chloroform, DMF and ethanol were all obtained from Sigma Aldrich.

5.2.2 Fabrication of Self-assembled Particles

CMC, HA, PDMAEMA and PLA-PDMAEMA were each dissolved in deionised water to form 500 µg/mL solutions. These were mixed in 1:5 ratios (CMC:PDMAEMA, CMC:PLA-PDMAEMA, HA:PDMAEMA or HA-PLA-PDMAEMA) and left to incubate for 1 h forming a suspension of self-assembled particles. Appropriate volumes of HCl or NaOH were added to the solutions prior to mixing in order to obtain three solutions at different pH (pH 5, pH 7 and pH 11). The samples were then freeze-dried and the precipitate collected for FTIR analysis.

5.2.3 Fabrication of Electrosprayed Particles

The electrospray apparatus used was as outlined in Fig. 3.1. The inner liquid was formed of CMC or HA dissolved in a mixture of 80% deionised water and 20% ethanol at a concentration of 100 µg/mL or 100 ng/mL. The outer liquid was formed of PDMAEMA or PLA-PDMAEMA dissolved in a mixture of 80% chloroform and 20% DMF at a concentration of 1 mg/mL. The liquids were sprayed separately in single electrospray at the onset voltage for cone-jet mode (applied voltage to needle

at 5-6 kV relative to ground) with a suitable extractor voltage (1-1.5 kV relative to ground) and collected on aluminium foil. The liquids were also sprayed together, the inner liquid at a flow rate of 0.2 mL/hr and the outer liquid at 0.1 mL/hr in coaxial cone-jet mode. The collection method was dependent on the method of particle analysis.

5.2.4 Fourier Transform Infrared Spectroscopy

ATR-FTIR spectroscopy (Tensor 27, Bruker) was used to obtain absorption spectra of the polymers in solid form, freeze-dried residue of self-assembled particles at varying pH, and dry polymer particles from single and coaxial electrospray which were collected on aluminium foil and dried in a vacuum oven at 40°C overnight.

5.2.5 Dynamic Light Scattering

DLS (Zetasizer Nano ZS, Malvern) was used to size and measure the zeta potential of self-assembled and electrosprayed particles. Electrosprayed particles were sprayed into grounded deionised water for 30 min and grounded 10mM NaCl for 30 min for sizing and zeta potential measurements respectively. Self-assembled particles were assembled at pH 7 in deionised water for sizing and in NaCl 10mM for zeta potential measurements.

5.3.6 Atomic Force Microscopy

AFM (NTegra, Bruker) was used with RTESP-300 aFM probes (Bruker) which were plasma-treated to render them hydrophobic and prevent particles adhering to them. Electrosprayed particles were collected on silicon wafer for 3 min, and self-

assembled particles were made in deionised water which was dropped onto silicon wafer and left to dry in ambient conditions.

AFM was performed in semi-contact or tapping mode and images were acquired with NOVA software where preliminary image processing was performed to flatten the images. Further image processing was performed in MATLAB. A script was written to threshold images to remove noise caused by surface roughness, identify centroids and give the diameter and maximum peak height of each centroid. The images were then examined by eye to remove any obvious non-rounded shapes that were likely debris, aggregation or a particle dragged along the wafer. Furthermore, any particles which were only 9 pixels in size were considered too small to be analysed accurately and were therefore discounted.

5.3.7 Transmission Electron Microscopy

TEM (JEOL 2010, JEOL Ltd.) was used to image electrosprayed and self-assembled particles with a 200kV beam. The inner phase was stained with silver ions to provide better contrast against the shell polymer. For electrosprayed particles, to prepare the inner liquid, 100 µg/ml of CMC was incubated for 1 h with 25 µg/ml of silver nitrate in a solution of 80% deionised water and 20% ethanol. The particles were fabricated as detailed in section 4.2.4 and sprayed directly onto a TEM grid for 3 min. In the case of self-assembly, 500 µg/ml of CMC was incubated for 1 h with 125 µg/ml of silver nitrate in deionised water. The particles were bulk assembled in solution as in section 4.2.3, and the solution dropped onto a TEM grid and left to dry in ambient conditions.

5.3 Results and Discussion

5.3.1 Impact of the molecular weight and concentration of CMC

First the impact of the molecular weight of CMC on particle size was examined by comparing the sizes of electrosprayed particles using higher molecular weight CMC (Mw 250,000) with the lower molecular weight CMC (Mw 90,000) that has been used so far. This is an important parameter to consider as the molecular weight of therapeutic DNA can vary greatly[188]. However, when using the Mw 250,000 CMC it was found to be difficult to maintain a stable cone-jet at the same concentration (100 ug/mL) that was used for Mw 90,000 CMC. This was thought to be due to the needle being blocked by the polymer and so the different molecular weights were compared at a lower concentration of 100 ng/mL while keeping the same flow rates as used previously (inner, 0.2 mL/h and outer 0.1 mL/h).

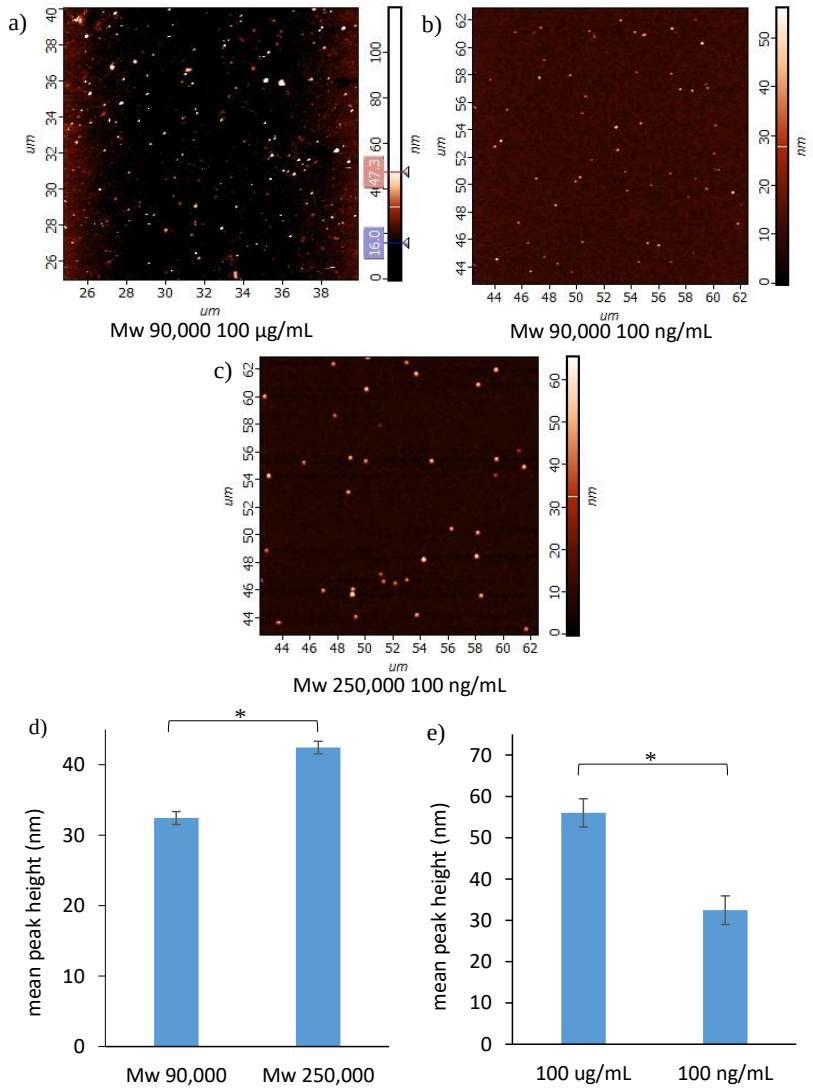

*Figure 5.1 AFM data from electrosprayed CMC-PDMAEMA particles. AFM images using a) Mw 90,000 CMC at 100 µg/mL, b) Mw 90,000 CMC at 100 ng/mL, c) Mw 250,000 at 100 ng/mL, and comparison of mean particles sizes with d) using different molecular weights of CMC (Mw 250,000, n = 96 and Mw 90,000, n = 112) at 100 µg/mL and e) Mw 90,000 CMC at different concentrations (100 µg/mL, n = 78 and 100 ng/mL, n = 112) (shown with standard error). In both d) and e), * indicates a significant difference between the two conditions for $p<0.05$ (unpaired t-test).*

AFM was used to compare the sizes of electrosprayed CMC-PDMAEMA particles with different molecular weights (Mw 90,000 and Mw 250,000) and concentrations (100 µg/mL and 100 ng/mL) of CMC. From the AFM images (Fig. 5.1 a,b & c), it can be seen that the particles have not collapsed as a concave particle would appear as a ring, rather than the bright points seen here.

Mw 90,000 and Mw 250,000 CMC gave mean particle diameters of 42 nm and 32 nm respectively (Fig. 5.1d). A t-test showed a significant difference between these particle sizes for $p<0.05$. Fink et al. examined self-assembly polyplexes with different molecular weights of DNA and also saw an increase in mean diameter with DNA molecular weight[188].

Different concentrations were also compared for Mw 90,000 CMC and the mean particle sizes were 67 nm and 32 nm for concentrations of 100 µg/mL and 100 ng/mL respectively (Fig. 5.1e). Overall, this suggests that when controlling for particle size when using DNA, the molecular weight must be taken into account, and as well as the flow rate, it is possible to control particle size by polymer concentration

5.3.2 Impact of Using Block Copolymer as the Shell Polymer

5.3.2.1 FTIR

First the FTIR of the PLA-PDMAEMA was compared with CMC in order to determine which peaks could be used to identify the presence of both polymers in electrosprayed particles.

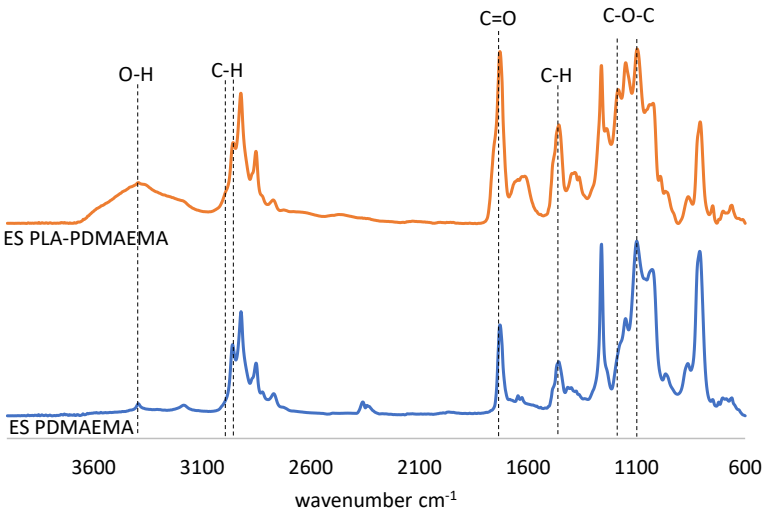

Figure 5.2 Comparison of FTIR spectra of single electrosprayed PDMAEMA and PLA-PDMAEMA

The peaks of electrosprayed PDMAEMA were identified in the previous chapter, and through comparison with the PLA-PDMAEMA spectra (Fig. 5.2) the contributions of PLA to the block copolymer can be seen through the appearance of new peaks and changes in peak ratios.

The broad peak at around 3300 cm^{-1} is attributed to the O-H group[189]. There are two peaks from the C-H group, the peaks at 2994 cm^{-1} appears as a shoulder, and the peak at 2932 cm^{-1} overlaps with a PDMAEMA peak[190, 191]. The peak at 1724 cm^{-1} can be attributed to the C=O group[189, 190], the peak at 1454 cm^{-1} can be attributed to the C-H group[192], and the peaks at 1174 cm^{-1} and 1088 cm^{-1} can both be attributed to the C-O-C group[189, 190, 193]. There is the additional appearance of a broad peak around 1650 cm^{-1} which is not identified, but it is present in other FTIR spectra of PLA in the

literature[191, 194]. However, this new peak overlaps with the 1600 cm^{-1} peak used to identify CMC presence in particles and so a new strategy must be found.

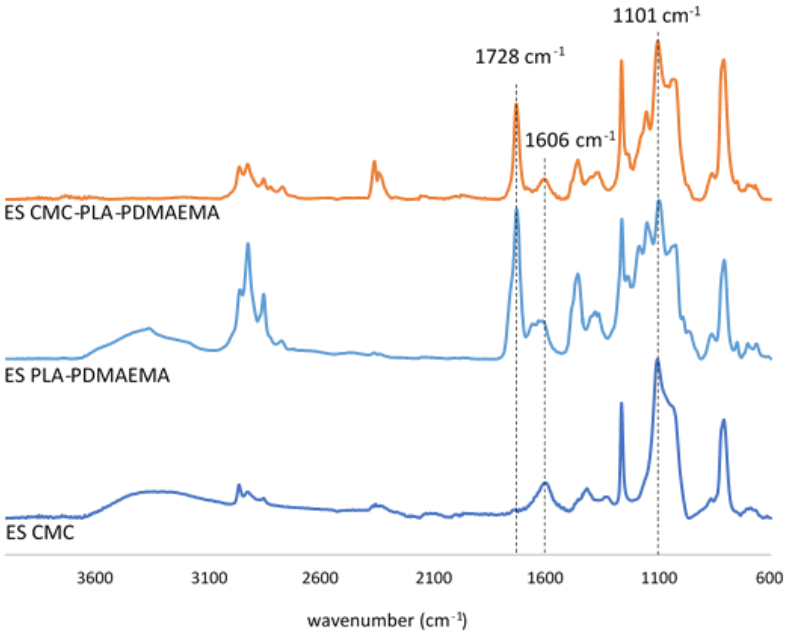

Figure 5.3 FTIR spectra of coaxially electrosprayed CMC-PLA-PDMAEMA particles compared with the single electrospray individual polymers (all samples vacuum-dried)

The FTIR spectra of coaxially electrosprayed CMC-PLA-PDMAEMA particles were compared with the single electrosprayed individual polymers in roder to confirm the presence of CMC. As with the electrosprayed CMC-PDMAEMA spectra (Fig. 5.3), there are again strong, sharp peaks visible at 1263 cm^{-1} and 810 cm^{-1}. However, the peak at 1728 cm^{-1} from the C=O in the ester is unique to PLA-PDMAEMA, and the ratios of other peaks to it can be taken from the CMC-PLA-PDMAEMA spectra and compared to the ratio in the PLA-PDMAEMA spectra. A change in ratio would indicate a contribution to the peak from CMC. Looking at ratio of the 1101 cm^{-1} peak from C-O-C of the oxygen bridge to the 1728 cm^{-1} peak, an increase can be seen from 1.06 in the PLA-PDMAEMA spectra to 1.68 in the CMC-

PLA-PDMAEMA spectra, indicating a contribution from the CMC and therefore confirming its presence in the particles.

5.3.2.2 Sizing

pH	Mean diameter (nm)	Std. Dev.	PdI	Std. Dev.
5	1018	167	1.000	0.000
7	111	2.38	0.200	0.019
11	371	39.8	0.382	0.042

Table 5.1 Varying pH of bulk-assembled CMC-PLA-PDMAEMA particles measured by DLS

Next, the mean diameters of bulk-assembled CMC-PLA-PDMAEMA complexes produced at different pH conditions were analysed by DLS (Table 5.1). PLA is also a pH responsive polymer and so it is important to determine if its addition to the system has had any effect on the pH at which the PLA-PDMAEMA is best able to condense CMC.

Complexes produced at pH 5 have an extremely high mean diameter, polydispersity index (PdI) and standard deviations, indicating the presence of aggregates. This is in strong contrast to the CMC-PDMAEMA self-assembled particles which had a mean diameter of 214 nm. As discussed in the previous chapter, CMC and PDMAEMA are expected to be slightly negative[174, 175] and positive[178, 179] respectively at this pH value. PLA is a polyacid like CMC and has a pKa value of 3.86[195] making it negatively charged at pH 5. At this pH, swelling is expected from PDMAEMA and so there would be a lower density of PLA in the corona of the particle. The hydrophobicity of PLA[196, 197] may have encouraged aggregation of particles, leading to the high diameter and PdI.

Particles produced at pH 7 and pH 11 show lower PdI, and as with CMC-PDMAEMA, pH 7 gives the lowest mean diameter of 111 nm with a PdI of 0.200. pH 11 is above the pKa of both CMC and PLA so both polymers are will experience swelling[198, 199]. While with CMC-PDMAEMA, pH 11 gave the largest particles most likely due to aggregation because of PDMAEMA's hydrophobicity, when using PLA-PDMAEMA, the PLA in the corona will prevent this aggregation.

However, as seen with CMC-PDMAEMA, complexes bulk -assembled at pH 7 give the lowest mean diameter and PdI, as it is gives the best balance between polymer swelling and polymer charge strength allowing for a strong interaction between CMC and the PDMAEMA of PLA-PDMAEMA and therefore CMC prepared at pH 7 was used for electrospray with PLA-PDMAEMA.

PLA-PDMAEMA has been used to complex with other molecules at pH 7 and shown similar size micelles being formed. Babikova et al.[186] used PLA-PDMAEMA to complex with curcumin and formed particles with a mean diameter between 76 nm and 165 nm (measure by DLS) depending on the ratio of PLA to PDMAEMA in the copolymer. Star-branched PLA-PDMAEMA has also been used by Qian et al.[129] as a gene vector and when loaded with DNA, was found to have a mean diameter between 65.0 nm and 93.2 nm (measured by DLS) depending on the number of PDMAEMA branches. While these diameters are similar however, the method of drug/DNA loading is different. Both methods rely upon the PLA-PDMAEMA self-assembling into micelles in aqueous phase, based upon the hydrophobicity of PLA. The micelles formed are therefore the reverse of what is produced here – PDMAEMA in the core with a PLA corona. The curcumin is trapped within the micelle as it forms, and the DNA adsorbed onto the PDMAEMA corona of the micelles. Despite this difference,

it seems that the mean diameter produced where PDMAEMA complexes with the payload, is comparable in scale to instances where the PLA is in the core.

Next, the sizes (determined by AFM) of electrosprayed CMC-PDMAEMA and CMC-PLA-PDMAEMA particles were compared to examine the ability of a block copolymer to condense CMC when using electrospray.

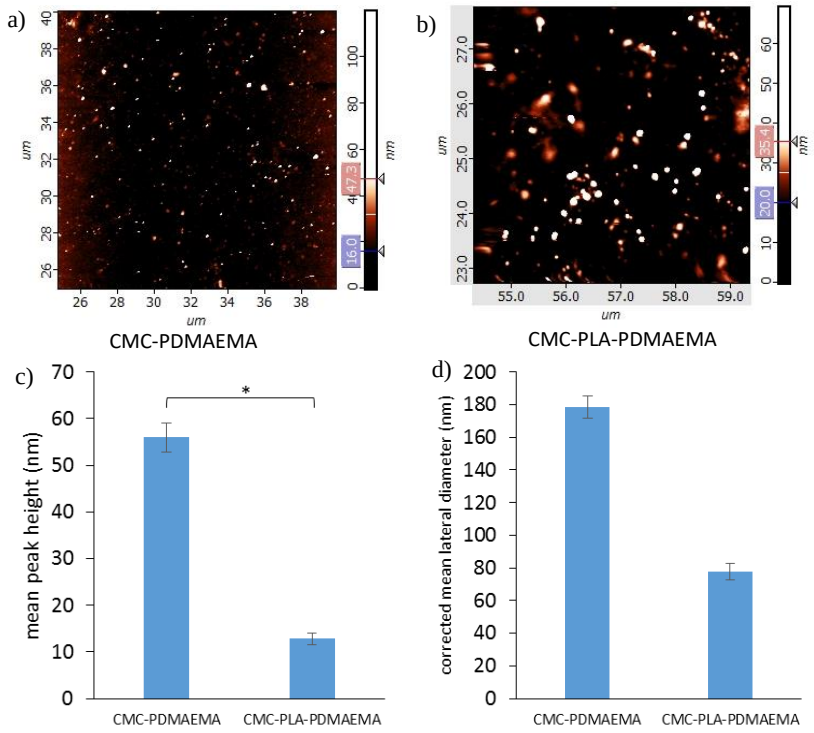

*Figure 5.4 AFM images of electrosprayed a) CMC-PDMAEMA particles, b) CMC-PLA-PDMAEMA particles, c) a comparison of the mean peak heights of CMC-PDMAEMA and CMC-PLA-PDMAEMA and d) a comparison of lateral diameter with a correction factor given by Yang et al.[147]. For c), * indicates significant difference for $p<0.05$ (unpaired t-test). Both c) & d) are shown with standard error.*

The AFM analysis of electrosprayed CMC-PDMAEMA and CMC-PLA-PDMAEMA particles show the mean diameter of the CMC-PLA-PDMAEMA particles to be significantly smaller than that of the CMC-PDMAEMA particles for $p<0.05$ (Fig. 5.4 c), and from the AFM images it can again be seen that the particles have not collapsed and become concave. Bulk-assembled particles were not examined by AFM due to the unknown stability of the dried complex, as described in section 4.3.1.3.

A difference in sizes between the two measuring methods is expected as AFM analyses a dry particle which may be flattened slightly by impact, and DLS analyses the hydrodynamic diameter of a wet particle which will experience some polymer swelling.

In the previous chapter, comparing the TEM images of bulk-assembled complexes and electrosprayed particles of CMC-PDMAEMA, and seeing the apparent lower density of CMC in the electrosprayed particles suggested that they had flattened. Although the lateral diameter measured by AFM is known to be inaccurate due to the tip geometry, using an average correction factor determined by Yang et al.[147], it is possible to get an idea for whether the particles have maintained a spherical shape or not. The corrected mean lateral diameters for CMC-PDMAEMA and CMC-PLA-PDMAEMA (Fig. 5.4d) are 178 nm and 78 nm respectively. When compared to the mean peak heights, it can be seen that the corrected lateral diameters are much larger still – 3.2 times larger for CMC-PDMAEMA and 6 times larger for CMC-PLA-PDMAEMA. This confirms that the particles are indeed flattening when landing on the silicon wafer substrate. However, if the particles are considered as spheres with flattened bases, with the mean peak as height and the corrected mean lateral diameter

as diameter, then the CMC-PDMAEMA particles are still one order of magnitude larger than the CMC-PLA-PDMAEMA particles in terms of volume.

It is known that in order to form the shell, the outer polymer is required to diffuse throughout the solvent of the droplet[13]. It therefore follows that there must be a difference in some aspect of shell formation between PDMAEMA and PLA-PDMAEMA, as all other electrospray conditions are unaltered. PDMAEMA has a positive charge, whereas PLA-PDMAEMA will have both a positive charge from the PDMAEMA and a negative charge from the PLA. During particle formation, the outer polymer must diffuse through the solvent around the droplet and sufficient chain entanglement must take place before the solvent evaporates for the shell to form[13, 200]. It is therefore possible that as the polymers diffuse through the solvent around a droplet, PDMAEMA molecules will be more spread out from each other due to electrostatic repulsion, and PLA-PDMAEMA molecules will be more packed together due to electrostatic attraction. This could lead to greater polymer entanglement in the PLA-PDMAEMA shell and hence the decrease in particle size as the solvent evaporates.

Particle	Mean diameter (nm)	Std. dev.	PdI	Std. dev.
CMC-PDMAEMA	117	17.94	0.373	0.064
CMC-PLA-PDMAEMA	106	10.34	0.355	0.039

Table 5.2 Comparison of DLS sizing between electrosprayed CMC-PDMAEMA and CMC-PLA-PDMAEMA

It was seen with AFM analysis that CMC-PLA-PDMAEMA particles were smaller than CMC-PDMAEMA particles and this is also seen with DLS sizing (Table

5.2), but the standard deviation suggests that the spread of particles sizes overlap and does not show much of a difference between the types of particle compared to the AFM data (Fig. 5.4).

Particles sizes obtained via DLS are expected to be larger than those obtained via AFM as firstly DLS samples are wet particles which may experience a degree of polymer swelling while AFM samples are dry particles which may have flattened slightly upon impact[201], as was seen to be the case. Additionally, DLS measures the hydrodynamic diameter of the particles, which is based upon particle diffusion and is therefore an indirect measurement of the physical particle size.

5.3.2.3 Zeta Potential

Next the zeta potential was examined and compared with that of CMC-PDMAEMA bulk-assembled complexes and electrosprayed particles to see the effect of the additional PLA in the shell.

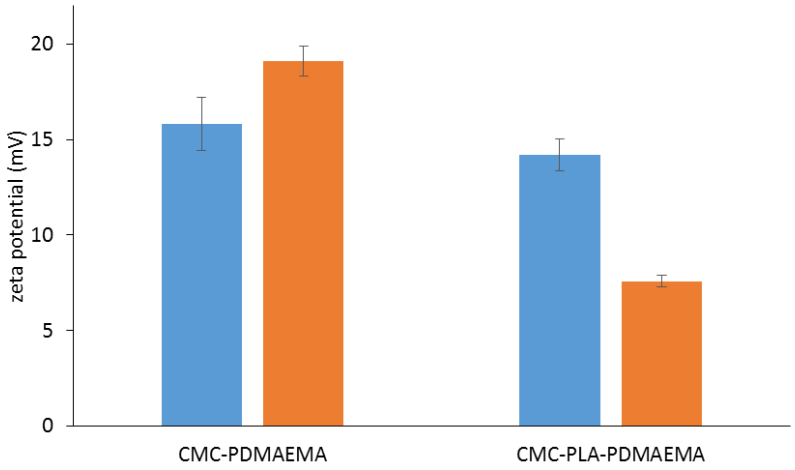

Figure 5.5 Zeta potential comparison of electrosprayed (blue) and self-assembled (orange) CMC-PDMAEMA and CMC-PLA-PDMAEMA particles (shown with standard deviation)

Looking at the zeta potential (Fig. 5.5) of CMC-PDMAEMA and CMC-PLA-PDMAEMA it can be seen that there is a distinct decrease from +19.1 mV to +7.58 mV for the self-assembled particles. In contrast, the electrosprayed particles see only a modest decrease from +15.8 mV to +14.2 mV.

The lower zeta potential seen with PLA-PDMAEMA in the self-assembled particles can be taken to indicate that the corona is rich in PLA as PLA has a negative zeta potential around pH 7[202, 203]. This indicates a radial alignment of the PLA-PDMAEMA molecules with the PDMAEMA oriented towards the core, complexing with the CMC. Similar structures have been seen with electrostatic self-assembly using other cationic block copolymers by Pippa et al. when encapsulating insulin[184] and by Pispas et al. when encapsulating lysozyme[185].

By contrast the zeta potentials for CMC-PDMAEMA and CMC-PLA-PDMAEMA show very little change, showing that the structure of the electrosprayed

particles differ from the self-assembled particles. It suggests that the shell is not as PLA rich as with the self-assembled particles i.e. no radial alignment of polymer molecules and therefore it can be concluded that any degree of electrostatic interaction that occurred between the core and shell polymer is negligible.

5.3.3 Comparing the use of HA and CMC

First the FTIR spectra of HA was examined to determine which peaks could be used to identify HA and so confirm its presence in electrosprayed particles.

5.3.3.1 FTIR

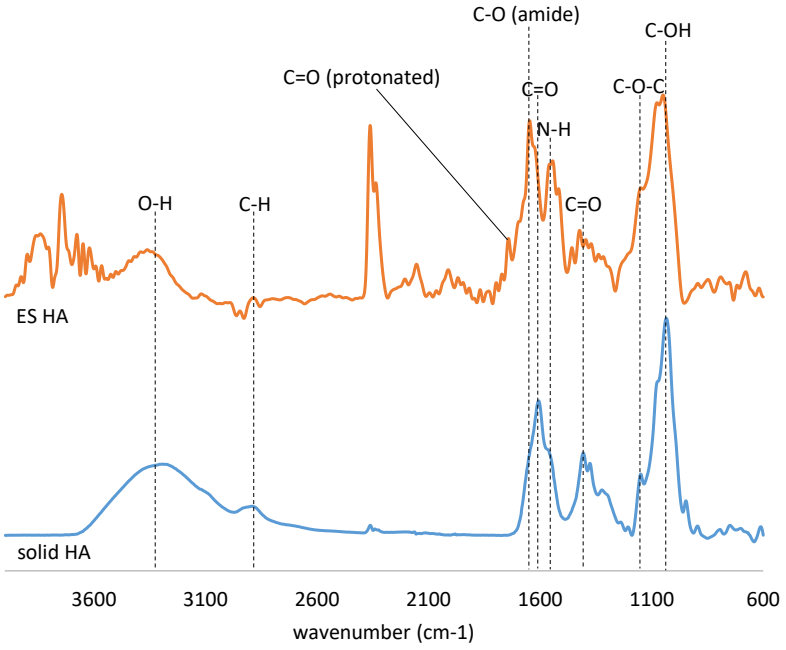

Figure 5.6 FTIR spectra comparison of solid HA and single electrosprayed HA showing the emergence of additional peaks following the electrospray process which may be due to protonation

From the solid HA FTIR spectra (Fig. 5.6), there are five well-resolved peaks that can be seen: a broad peak around 3294 cm^{-1} from the O-H group, a peak at 2893 cm^{-1} from the C-H group, a peak at 1606 cm^{-1} from the C=O asymmetric stretch, a peak at 1405 cm^{-1} from the C=O symmetric stretch, and a peak at 1034 cm^{-1} from the

C-O stretch[204-206]. Additionally there is a slight shoulder at 1650 cm^{-1} from the C-O group of the amide, a shoulder at 1560 cm^{-1} that is attributed to the N-H from the amide group and a small peak at 1149 cm^{-1} from the C-O-C oxygen bridge[206].

The electrosprayed HA spectra shares the same general shape but the emergence of additional peaks is clear. The first main difference is a new peak at 1741 cm^{-1} which can be attributed to the asymmetric stretch of the protonated form of the C=O group seen at 1606 cm^{-1} [206]. This protonation leads to a reduction in intensity of the unprotonated peak, which sees both the C-O amide and N-H shoulders in the solid HA spectra, become clear peaks in the electrosprayed spectra.

The appearance of the protonated peak seems to be evidence that the HA is undergoing protonation during the electrospray process. Protonation driven by electric fields has been seen by others[207, 208]. Sugihara et al. saw that for a monolayer of a carboxylic acid, a positive applied voltage shifted the pKa upwards[209]. However, the same protonation of the C=O from the carboxylate group is not seen with electrosprayed CMC.

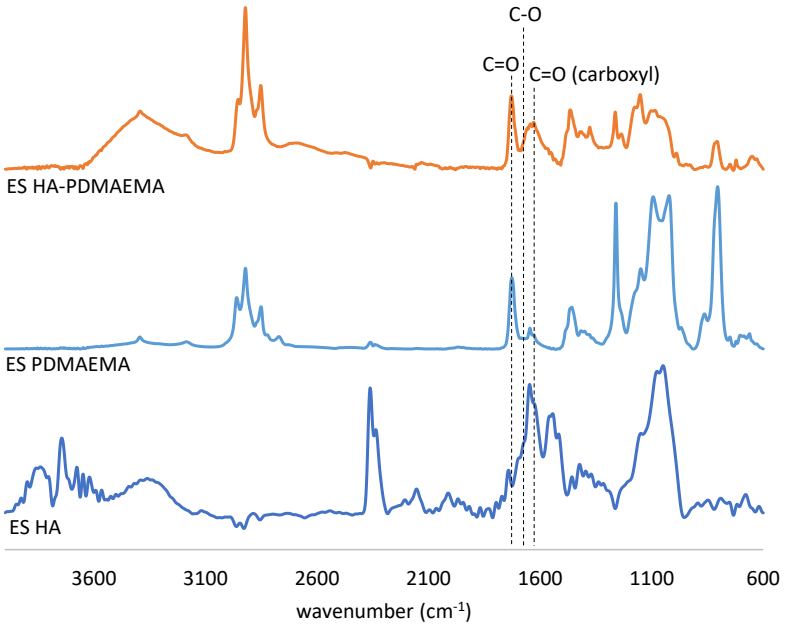

Figure 5.7 FTIR spectra of electrosprayed HA-PDMAEMA compared with single electrosprayed PDMAEMA and HA

In the FTIR spectra of HA-PDMAEMA (Fig. 5.7), a broad peak from the C=O of the carboxyl group in HA can be seen at 1629 cm^{-1}, with a slight shoulder from the C-O in the amide group at 1654 cm^{-1}. Its ratio to the peak at 1737 cm^{-1} from the C=O of PDMAEMA indicates the presence of both polymers in the coaxially electrosprayed particles.

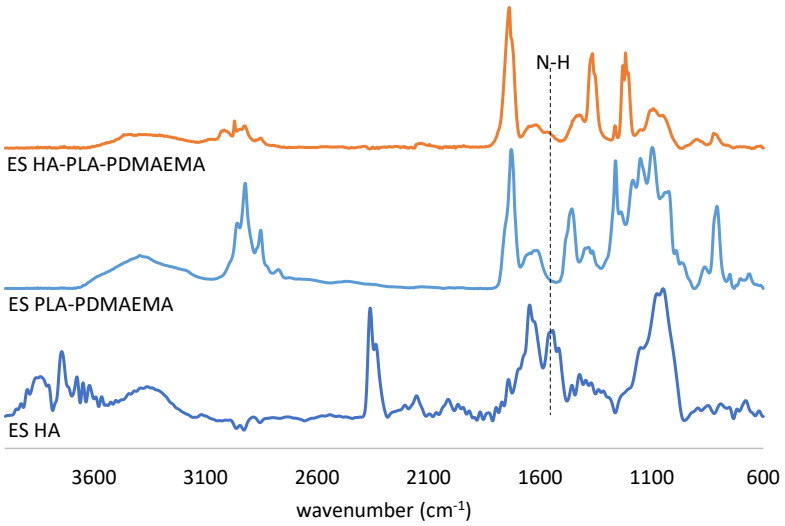

Figure 5.8 FTIR spectra of electrosprayed HA-PLA-PDMAEMA compared with single electrosprayed PLA-PDMAEMA and HA

Next, the FTIR spectra of HA-PLA-PDMAEMA was assessed to check for the presence of both polymers in the electrosprayed particles (Fig. 5.8). As determined from the CMC-PLA-PDMAEMA spectra, when using PLA-PDMAEMA, it is not possible to look at the C=O peak from the carboxyl group to find evidence of HA presence in the electrosprayed particles. However, the appearance of a peak around 1560 cm^{-1} has no contribution from the PDMAEMA spectra and can be attributed to the peak from N-H in HA[206], thereby confirming the presence of HA in the particles.

5.3.3.2 Sizing

Particle	Mean diameter (nm)	Std. dev.	PdI	Std. dev.
HA-PDMAEMA	218.3	2.20	0.295	0.028
HA-PLA-PDMAEMA	431.4	28.33	0.337	0.048
CMC-PDMAEMA	165.3	4.84	0.283	0.120
CMC-PLA-PDMAEMA	110.6	2.38	0.200	0.019

Table 5.3 Comparison of mean diameter (from DLS) of particles bulk-assembled at pH 7

First the sizes of self-assembled particles were assessed via DLS (Table 5.3). It can be seen that while there was a decrease in mean diameter and PdI when changing from using PDMAEMA to PLA-PDMAEMA with CMC. However, the opposite result is seen when using HA; using PLA-PDMAEMA almost doubles the mean diameter and there is additionally an increase in the mean diameter standard deviation and PdI.

The pKa of HA is 3.0[187] and so at pH 7 it is expected to be strongly negatively charged[210] and complex with the positively charged PDMAEMA. This is evidenced by the low PdI, similar to that of CMC-PDMAEMA. This may be related to difference swelling properties of CMC and HA; at pH 7, HA shows a much higher swelling ratio than CMC which would lead to a larger particle size[211, 212]. When using the block copolymer, the larger particle size and high standard deviation of HA-PLA-PDMAEMA suggests that aggregation is occurring. As the HA-PDMAEMA particle are already larger, it is possible that this has led to a less dense PLA corona, allowing attraction between the PLA and PDMAEMA in different particles.

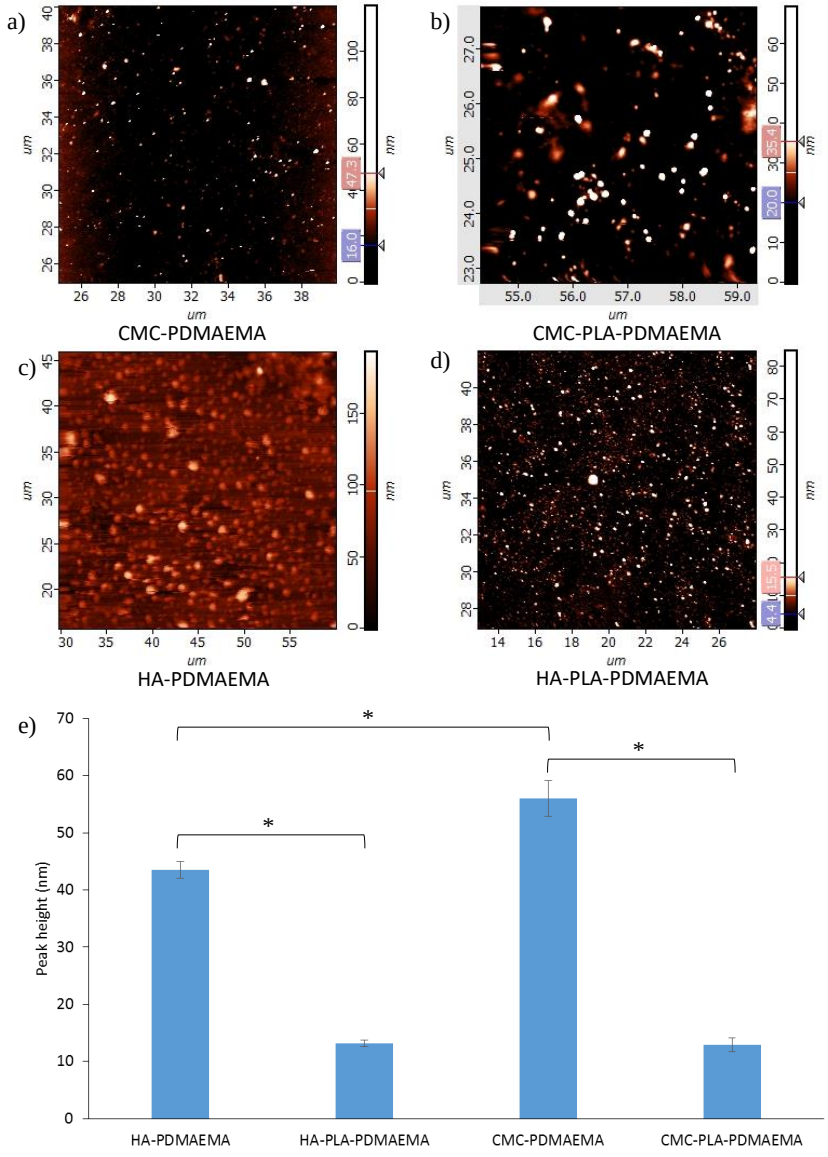

*Figure 5.9 AFM images of electrosprayed particles a) CMC-PDMAEMA, b) CMC-PLA-PDMAEMA, c) HA-PDMAEMA, d) HA-PLA-PDMAEMA, and a comparison of mean peak heights obtained via AFM (HA-PDMAEMA n = 291, HA-PLA-PDMAEMA n = 170, CMC-PDMAEMA n = 78, CMC-PLA-PDMAEMA n = 81) (shown with standard error). * indicates a significant difference for $p<0.05$ (unpaired t-test).*

The mean peak height of electrosprayed particles was obtained via AFM (Fig. 5.9). Unlike the self-assembled particles, the electrosprayed particles with HA show the same trend as the CMC particles – a decrease in size when changing from PDMAEMA to PLA-PDMAEMA in the shell. This suggests that there is perhaps a problem with the stability of the self-assembled HA particles in aqueous phase.

Particle	Mean peak height (nm)	Corrected mean lateral diameter (nm)	Aspect ratio	Partial Sphere Volume (nm^3)
HA-PDMAEMA	43.5	597	13.7	1.6×10^6
HA-PLA-PDMAEMA	13.2	225	17.1	5.9×10^4
CMC-PDMAEMA	56.0	178	3.2	6.9×10^5
CMC-PLA-PDMAEMA	12.9	78	6.1	1.8×10^4

Table 5.4 Comparing sizes from AFM data of electrosprayed particles with all core-shell combinations

Again, the lateral diameters obtained via AFM can also be considered to give an idea of how flattened the particles are (Table 5.4). Comparing the HA and CMC particles it is clear that although from the mean peak heights the particles appear similar, the aspect ratio shows that the HA particles are most likely far softer. Additionally, from the partial sphere volume it can be seen that the HA particles are larger than the CMC particles.

The smaller size of the PLA-PDMAEMA particles in both cases implies that the chain entanglement may be occurring faster than with PDMAEMA alone, as discussed in section 5.3.2. This may be due to electrostatic interaction between the negative PLA and positive PDMAEMA, compared to the positively-charged

PDMAEMA alone for which electrostatic repulsion may have led to lower degree of chain entanglement and so a larger shell formed as solvent evaporation took place.

Looking at the DLS sizing of electrosprayed particles with HA (Table 5.5), it is clear from the large diameters and standard deviation that the particles are not stable in aqueous phase and are aggregating.

Particle	Mean diameter (nm)	Std. dev.	PdI	Std. dev.
HA-PDMAEMA	532	51.77	0.553	0.046
HA-PLA-PDMAEMA	1598	654.9	0.912	0.152

Table 5.5 Comparison of mean diameter (from DLS) of electrosprayed HA-PDAMEMA and HA-PLA-PDMAEMA particles

In all cases for electrosprayed particles, it can be seen that there is a problem with maintaining morphology during dry collection and wet collection, particularly for the HA particles. Methods employed by others to preserve morphology and prevent aggregation have included spraying into an emulsion to coat the particles to give more stability[12], and performing electrospray in an air-flow chamber with the particles collected in a filter[213]. It is also possible to increase the polymer concentration in the shell to give a thicker and potentially stronger shell. However, the shell polymer concentration can only be increased so much as beyond a certain point, fibre formation is seen[50]. Increasing the outer polymer concentration also affects the particle size[214] and so it would be better to explore other avenues for preventing particle deformation first.

5.3.3.3 Zeta Potential

Next the zeta potential of bulk-assembled complexes and electrosprayed particles was compared for all polymer combinations to give an insight into the shell structure.

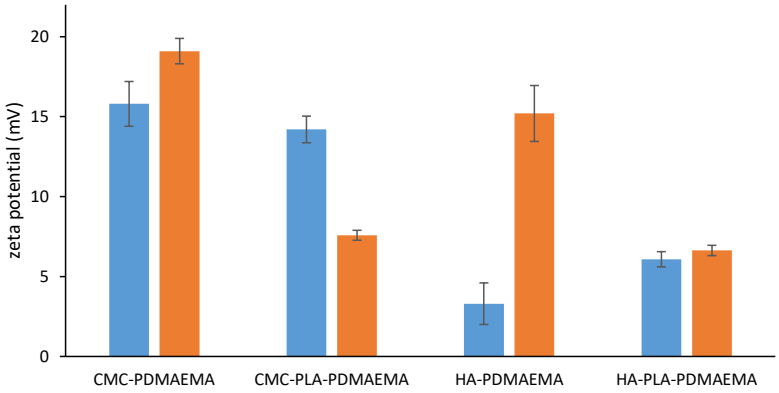

Figure 5.10 Comparison of zeta potential across different polymer combinations prepared with electrospray (blue) and self-assembly (orange) (shown with standard deviation)

Fig. 5.10 shows the variation in zeta potential across the different combinations of inner and outer polymer produced by both electrospray and self-assembly methods. For the self-assembly method, the same trend can be seen for both CMC and HA particles – there is a decrease in zeta potential when changing the outer shell polymer from PDMAEMA to PLA-PDMAEMA. This suggests that the interaction between the inner and outer polymers does not vary between the CMC and HA.

For the electrospray method, there is a very slight decrease with the CMC particles, but the HA particles show no such trend. This suggests that the particles are not stable and it is clear from the particle sizing by DLS (Table 5.4), that the particles

have aggregated. The low zeta potential of the HA samples compared to the CMC samples suggests that the HA has indeed escaped from the particles and the mixture of HA and PDMAEMA or PLA-PDMAEMA aggregates gives an overall low zeta potential.

5.3.3.4 TEM

All polymer combinations of bulk-assembled complexes and electrosprayed particles were examined by TEM and compared to check for core-shell structure.

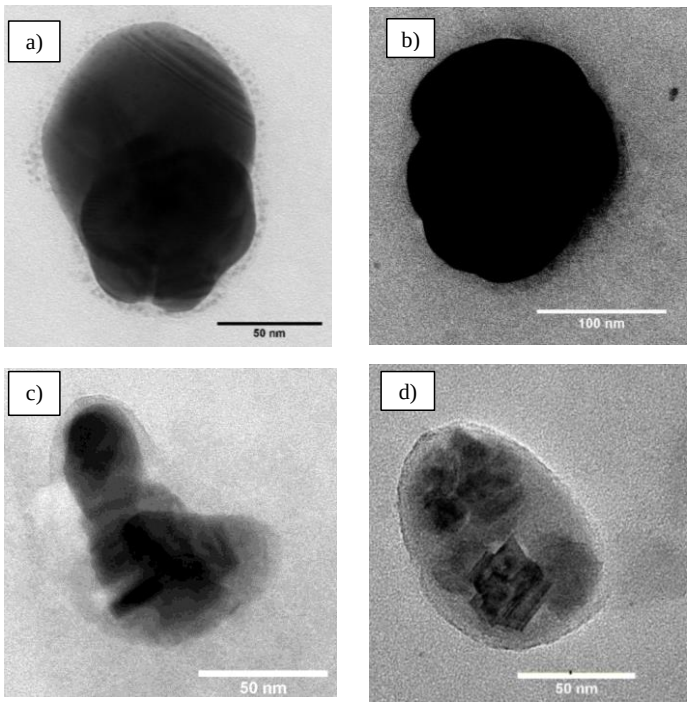

Figure 5.11 TEM images of bulk-assembled complexes a) CMC-PDMAEMA, b) CMC-PLA-PDMAEMA, c) HA-PDMAEMA and d) HA-PLA-PDMAEMA

From the TEM images in Fig. 5.11, it is clear that there is a difference between CMC and HA bulk-assembled complexes. While a core-shell structure can be seen in all cases, the cores of the CMC complexes show much higher density than the HA, and within the HA it seems that individual blocks can be seen. Basta et al. saw complexation of CMC with silver giving rise to both rounded and angular complexes depending on the source of CMC[215]. It is possible that what is being seen here is the encapsulation of CMC-silver and HA-silver complexes. This suggests that the staining method should be revised in order to prevent this complexation.

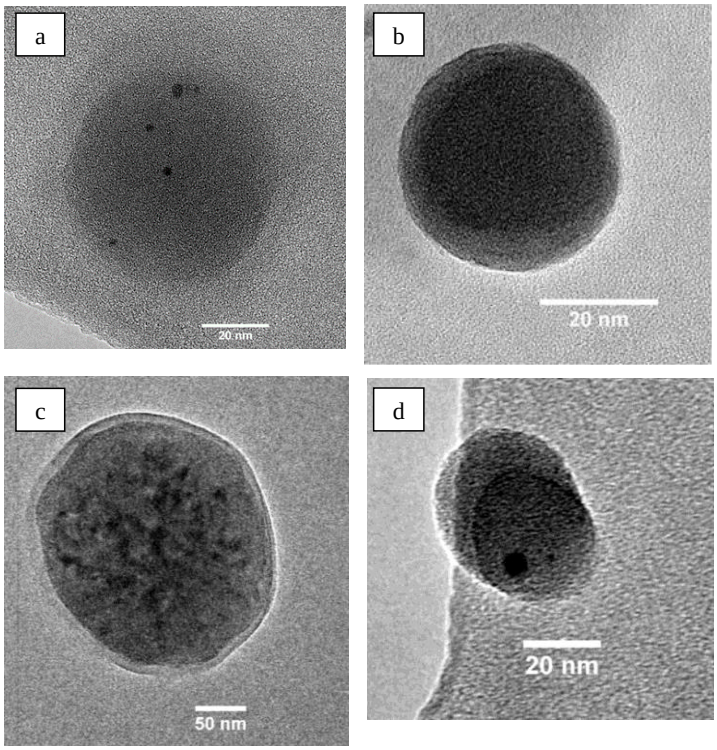

Figure 5.12 TEM images of electrosprayed particles a) CMC- PDMAEMA, b) CMC-PLA-PDMAEMA, c) HA-PDMAEMA and d) HA-PLA-PDMAEMA

From the electrosprayed TEM images (Fig. 5.12), it is clear that while all three particles appear to have a core-shell structure, they all have a different appearance. However, the CMC-PLA-PDMAEMA particle is similar in appearance to coaxially electrosprayed particles by Shams et al.[116] and the HA-PDMAEMA and HA-PLA-PDMAEMA particles are similar to coaxially electrosprayed particles by Lee et al.[57].

As seen from the AFM data, the particles with a PLA-PDMAEMA shell are smaller than those with a PDMAEMA shell. Although only single particles are shown here, the diameters are not as large as the mean corrected lateral diameters seen with AFM and so it seems that the shape of the particles is better preserved with the TEM grids. This may be related to the difference in softness between the silicon wafer and the lacey carbon of the TEM grids.

Comparing the bulk-assembled complexes with the electrosprayed particles, it is clear that the structures seen within the core in the bulk-assembled complexes are not present. It is possible that as the bulk-assembly solution is left to dry on the TEM grids, that additional complexation and aggregation is occurring during this time.

5.4 Conclusion

Due to their different mechanisms of synthesis, bulk-assembled complexes and electrosprayed particles can display different properties. In self-assembly, size can be controlled through the pH the particles are assembled in due to the effects on the charge of the polymers and polymer swelling. The clear decrease in zeta potential when going from PDMAEMA to PLA-PDMAEMA shows that there is an organisation to the outer shell that is not present in the electrosprayed particles which see only a slight zeta potential decrease. This suggests that while in self-assembly, arranging the orientation of a shell polymer so that a functionalised group is gathered

mainly on the outer surface can be achieved, they will be more evenly distributed throughout the whole shell in electrospray, and polymer charge has negligible effect on interaction between polymers during electrospray compared to self-assembly. Therefore functionalisation should occur after the particles have been produced, for example by an additional coating or a using a triaxial needle: inner liquid – core, middle liquid – shell, outer liquid – additional functionalisation.

From the particle sizing, it seems that PLA-PDMAEMA is able to produce smaller particles in electrospray with both CMC and HA, but the particles containing HA are larger than their CMC counterparts. The ability of the PLA-PDMAEMA to condense the core polymer is thought to be due to a tighter shell formation due to electrostatic interaction between the PLA-PDMAEMA molecules themselves due to the positively charged PDMAEMA and negatively charged PLA blocks. The larger size of the HA particles is thought to be due to the higher swelling ratio of HA compared to CMC.

There is however, an issue with the electrospray particle collection affecting the particle morphology. Flattening of the particles was seen during dry collection with electrospray for AFM and to a lesser degree for TEM which makes it difficult to size the dry particles. In wet collection, for zeta sizing and zeta potential measurements, the CMC particles were seen to be more stable than the HA particles which showed a high degree of aggregation. Methods employed by others to preserve morphology and prevent aggregation have included spraying into an emulsion to coat the particles to give more stability[12], and performing electrospray in an air-flow chamber with the particles collected in a filter[213]. The employment of similar methods may allow for better characterisation and comparison with the bulk-assembled

complexes; while the electrosprayed CMC particles appear to be smaller than the equivalent bulk-assembled complexes, they also have a slightly higher PdI which may be related to instability or aggregation.

In the case of using CMC and HA as substitutes for DNA, CMC appears to be the better choice as it displays better stability in aqueous phase and produced smaller particles, on a similar scale to viruses, in wet and dry conditions, most likely due to the lower swelling ratio of CMC.

Chapter Six

Conclusions and Future Work

6.1 Conclusions

This study has compared the abilities of a block copolymer (PLA-PDMAEMA) and homopolymer (PDMAEMA) to condense long-chain polymers (CMC and HA) when forming core-shell particles through coaxial electrospray, with an interest to proposing CMC and HA as polymers that can be used as cost-effective models for DNA. Looking at a common chemical supplier (Sigma-Aldrich), CMC and HA are available in the greatest range of molecular weights compared to other polymers negative at neutral pH such as PAA, PAM or PMAA. Additionally, CMC is far cheaper; 100 g can be purchased for less than £50 unlike PAA, PAM and PMAA which can only be bought in milligrams or tens of grams and are considerably more expensive per gram. Additionally electrosprayed particles and bulk-assembled complexes of the same inner and outer polymer weight ratios have been characterised and compared.

The core-shell structure has been confirmed for all particle types, although the zeta potential shows that the structure of the core varies between electrosprayed particles and bulk-assembled complexes. The reduction in zeta potential between PDMAEMA and PLA-PDMAEMA shells of the complexes indicates that when using the block copolymer, the PDMAEMA block is oriented towards the core giving a PLA rich corona. In contrast very little zeta potential reduction is seen with the

electrosprayed particles suggesting that this radial orientation is not present. However, with both methods, it seemed PLA-PDMAEMA was able to produce smaller complexes and particles albeit by different methods. It is proposed that for the electrosprayed particles, electrostatic interaction between the PLA-PDMAEMA molecules as they diffuse through the solvent shell leads to a tighter shell structure and so a smaller final particle, compared to the PDMAEMA alone. However, this difference in the shell structures between electrospray and self-assembly means that while in self-assembly, multi-block polymers can be radially oriented around the core to form structured complexes (e.g. core -> protective shell -> functionalised group), in electrospray one would expect the functionalised group to appear evenly distributed throughout the shell, rather than gathered on the surface. Achieving functionalisation on electrosprayed particles may require a higher concentration of the functionalised group, use of triaxial needles or coating the particles during wet collection.

Particle sizing indicates that the electrosprayed particles containing CMC are on the nanoscale (~100 nm), similar to bulk-assembled complex sizes and are also similar in size DNA and PDMAEMA complexes seen in the literature. However, problems were seen with electrosprayed particle deformation during dry collection. This suggests that the electrosprayed particles are relatively soft and an alternate collection method to spraying directly onto a hard substrate would help better preserve the particle morphology. Evidence supporting this can be seen in the reduction of particle diameter between the AFM data (particles sprayed onto silicon wafer) and the TEM data (particles sprayed onto lacey carbon film). Additionally the HA particles appeared highly unstable in aqueous phase as a high degree of aggregation was seen. It is possible that this is related to HA's high swelling ratio and therefore CMC seems to the better candidate for a cost-effective model for DNA. It is able to produce

electrosprayed particles with a similar zeta potential to bulk-assembled polymer encapsulated DNA particles seen in the literature which suggests that it may show comparative cell transfection abilities.

6.2 Future work

This study has indicated that 1) during electrospray, use of a block copolymer in the outer liquid leads to the creation of a smaller particle than the use of a homopolymer, and 2) CMC may be a suitable model for DNA as it is able to produce particles through electrospray that have a similar zeta potential to bulk-assembled DNA polymer capsules and therefore also display similar transfection ability. The next step would be to compare electrosprayed CMC particles with DNA with both PDMAEMA and PLA-PDMAEMA in order to directly compare their behaviour and evaluate how similar they are. However, further work is also required to create a particle that is robust enough to withstand deformation during dry collection and achieve a more in depth characterisation of the particle structure.

The deformation of electrosprayed particles during dry collection makes it difficult to measure the size of dried particles accurately and also the softness of the shell suggests that there is some way to go before these particles are comparable in strength to viral vectors. It would be worthwhile exploring other collection methods such as using softer collection substrates or coating particles during wet collection to add strength to the shell. Alternatively increasing the thickness of the shell could also improve strength although the degree to which this can be done is limited due to fibre production as the polymer weight percentage increases.

During TEM imaging, Energy Dispersive Spectroscopy could be used to look further into the structure of the particles and complexes, and provide additional information as to whether any mixing of the two polymer phases has occurred.

Finally an assessment of the ability of bulk-assembled complexes and electrosprayed particles to transfect cells compared to viral vectors would be beneficial. With the goal of producing a non-viral vector, it is important that it has comparable transfection ability to viral vectors.

7. References

1. Ho, C.S. et al. Electrospray ionisation mass spectrometry: principles and clinical applications. *The Clinical biochemist. Reviews* **24**, 3-12 (2003).
2. Gamero-Castano, M. & Hruby, V. Electrospray as a Source of Nanoparticles for Efficient Colloid Thrusters. *J Propul Power* **17**, 977-987 (2001).
3. Jaworek, A. et al. Electrospray Nanocoating of Microfibres. *Solid State Phenomena* **140**, 127-132 (2008).
4. Bock, N., Dargaville, T.R. & Woodruff, M.A. Electrospraying of polymers with therapeutic molecules: State of the art. *Prog Polym Sci* **37**, 1510-1551 (2012).
5. Ganan-Calvo, A.M., Davila, J. & Barrero, A. Current and droplet size in the electrospraying of liquids. Scaling laws. *J Aerosol Sci* **28**, 249-275 (1997).
6. Ganan-Calvo, A.M., Rebollo-Munoz, N. & Montanero, J.M. The minimum or natural rate of flow and droplet size ejected by Taylor cone-jets: physical symmetries and scaling laws. *New J Phys* **15** (2013).
7. Gomez, A., Bingham, D., Juan, L.d. & Tang, K. Production of protein nanoparticles by electrospray drying, Vol. 29. (1998).
8. Shang, L., Nienhaus, K. & Nienhaus, G.U. Engineered nanoparticles interacting with cells: size matters. *J Nanobiotechnol* **12** (2014).
9. He, C.B., Hu, Y.P., Yin, L.C., Tang, C. & Yin, C.H. Effects of particle size and surface charge on cellular uptake and biodistribution of polymeric nanoparticles. *Biomaterials* **31**, 3657-3666 (2010).
10. Xu, A.R. et al. A physical model for the size-dependent cellular uptake of nanoparticles modified with cationic surfactants. *International Journal of Nanomedicine* **7**, 3547-3554 (2012).
11. Chakraborty, S., Liao, I.C., Adler, A. & Leong, K.W. Electrohydrodynamics: A facile technique to fabricate drug delivery systems. *Adv Drug Deliver Rev* **61**, 1043-1054 (2009).

12. Almería, B., Fahmy, T.M. & Gomez, A. A multiplexed electrospray process for single-step synthesis of stabilized polymer particles for drug delivery. *Journal of Controlled Release* **154**, 203-210 (2011).

13. Almeria, B., Deng, W.W., Fahmy, T.M. & Gomez, A. Controlling the morphology of electrospray-generated PLGA microparticles for drug delivery. *J Colloid Interf Sci* **343**, 125-133 (2010).

14. Chen, D.R., Wendt, C.H. & Pui, D.Y.H. A novel approach for introducing bio-materials into cells. *Journal of Nanoparticle Research* **2**, 133-139 (2000).

15. Boda, S.K., Li, X. & Xie, J. Electrospraying an enabling technology for pharmaceutical and biomedical applications: A review. *J Aerosol Sci* **125**, 164-181 (2018).

16. Wu, Y., Fei, Z.Z., Lee, L.J. & Wyslouzil, B.E. Coaxial Electrohydrodynamic Spraying of Plasmid DNA/Polyethylenimine (PEI) Polyplexes for Enhanced Nonviral Gene Delivery. *Biotechnology and Bioengineering* **105**, 834-841 (2010).

17. Cloupeau, M. & Prunetfoch, B. Electrostatic Spraying of Liquids in Cone-Jet Mode. *J Electrostat* **22**, 135-159 (1989).

18. Jaworek, A. & Krupa, A. Classification of the modes of EHD spraying. *J Aerosol Sci* **30**, 873-893 (1999).

19. Marginean, I., Kelly, R.T., Page, J.S., Tang, K. & Smith, R.D. Electrospray characteristic curves: In pursuit of improved performance in the nanoflow regime. *Analytical Chemistry* **79**, 8030-8036 (2007).

20. Marginean, I., Parvin, L., Heffernan, L. & Vertes, A. Flexing the electrified meniscus: The birth of a jet in electrosprays. *Analytical Chemistry* **76**, 4202-4207 (2004).

21. Taylor, G. Disintegration of Water Drops in an Electric Field, Vol. 280. (1964).

22. Higuera, F.J. Flow rate and electric current emitted by a Taylor cone. *J Fluid Mech* **484**, 303-327 (2003).

23. de la Mora, J.F. The fluid dynamics of Taylor cones. *Annu Rev Fluid Mech* **39**, 217-243 (2007).

24. Hartman, R.P.A., Brunner, D.J., Camelot, D.M.A., Marijnissen, J.C.M. & Scarlett, B. Jet break-up in electrohydrodynamic atomization in the cone-jet mode. *J Aerosol Sci* **31**, 65-95 (2000).

25. Huebner, A.L. & Chu, H.N. INSTABILITY AND BREAKUP OF CHARGED LIQUID JETS. *J Fluid Mech* **49**, 361-& (1971).

26. Li, F., Yin, X.-Y. & Yin, X.-Z. Axisymmetric and non-axisymmetric instability of an electrified viscous coaxial jet. *J Fluid Mech* **632**, 199-225 (2009).

27. Hartman, R.P.A., Brunner, D.J., Camelot, D.M.A., Marijnissen, J.C.M. & Scarlett, B. Electrohydrodynamic atomization in the cone-jet mode physical modeling of the liquid cone and jet. *J Aerosol Sci* **30**, 823-849 (1999).

28. Rayleigh, L. XX. On the equilibrium of liquid conducting masses charged with electricity. *Philosophical Magazine Series 5* **14**, 184-186 (1882).

29. De la mora, J.F. & Loscertales, I.G. The Current Emitted by Highly Conducting Taylor Cones. *J Fluid Mech* **260**, 155-184 (1994).

30. Yao, J., Lim, L.K., Xie, J.W., Hua, J.S. & Wang, C.H. Characterization of electrospraying process for polymeric particle fabrication. *J Aerosol Sci* **39**, 987-1002 (2008).

31. Ganan-Calvo, A.M. & Montanero, J.M. Revision of capillary cone-jet physics: Electrospray and flow focusing. *Physical Review E* **79** (2009).

32. Ganan-Calvo, A.M., Lopez-Herrera, J.M., Herrada, M.A., Ramos, A. & Montanero, J.M. Review on the physics of electrospray: From electrokinetics to the operating conditions of single and coaxial Taylor cone-jets, and AC electrospray. *J Aerosol Sci* **125**, 32-56 (2018).

33. Park, I., Hong, W.S., Kim, S.B. & Kim, S.S. Experimental investigations on characteristics of stable water electrospray in air without discharge. *Physical Review E* **95** (2017).

34. Chen, D.R. & Pui, D.Y.H. Experimental investigation of scaling laws for electrospraying: Dielectric constant effect. *Aerosol Sci Tech* **27**, 367-380 (1997).

35. Scheideler, W.J. & Chen, C.H. The minimum flow rate scaling of Taylor cone-jets issued from a nozzle. *Applied Physics Letters* **104** (2014).

36. Yamashita, M. & Fenn, J.B. Negative-Ion Production with the Electrospray Ion-Source. *J Phys Chem-Us* **88**, 4671-4675 (1984).

37. Ryan, C.N., Smith, K.L. & Stark, J.P.W. The flow rate sensitivity to voltage across four electrospray modes. *Applied Physics Letters* **104** (2014).

38. Hwang, Y.K., Jeong, U. & Cho, E.C. Production of uniform-sized polymer core-shell microcapsules by coaxial electrospraying. *Langmuir* **24**, 2446-2451 (2008).

39. Lopez-Herrera, J.M., Barrero, A., Lopez, A., Loscertales, I.G. & Marquez, M. Coaxial jets generated from electrified Taylor cones. Scaling laws. *J Aerosol Sci* **34**, 535-552 (2003).

40. Mei, F. & Chen, D.-R. Investigation of compound jet electrospray: Particle encapsulation. *Physics of Fluids* **19**, 103303 (2007).

41. Ciach, T. Microencapsulation of drugs by electro-hydro-dynamic atomization. *International Journal of Pharmaceutics* **324**, 51-55 (2006).

42. Valo, H. et al. Electrospray Encapsulation of Hydrophilic and Hydrophobic Drugs in Poly(L-lactic acid) Nanoparticles. *Small* **5**, 1791-1798 (2009).

43. Zhang, S. et al. Coaxial Electrospray Formulations for Improving Oral Absorption of a Poorly Water-Soluble Drug. *Molecular Pharmaceutics* **8**, 807-813 (2011).

44. Rezvanpour, A., Attia, A.B.E. & Wang, C.-H. Enhancement of Particle Collection Efficiency in Electrohydrodynamic Atomization Process for Pharmaceutical Particle Fabrication. *Ind Eng Chem Res* **49**, 12620-12631 (2010).

45. Zamani, M., Prabhakaran, M.P., Thian, E.S. & Ramakrishna, S. Protein encapsulated core-shell structured particles prepared by coaxial electrospraying: Investigation on material and processing variables. *International Journal of Pharmaceutics* **473**, 134-143 (2014).

46. Ho, H. & Lee, J. PEG/PLA Core/Shell Particles from Coaxial Electrohydrodynamic Spray Drying. *Macromolecular Research* **19**, 815-821 (2011).

47. Jing, Y., Zhu, Y., Yang, X., Shen, J. & Li, C. Ultrasound-Triggered Smart Drug Release from Multifunctional Core-Shell Capsules One-Step Fabricated by Coaxial Electrospray Method. *Langmuir* **27**, 1175-1180 (2011).

48. Park, C.H. & Lee, J. Electrosprayed Polymer Particles: Effect of the Solvent Properties. *J. Appl. Polym. Sci.* **114**, 430-437 (2009).

49. Wu, Y. et al. Coaxial Electrohydrodynamic Spraying: A Novel One-Step Technique To Prepare Oligodeoxynucleotide Encapsulated Lipoplex Nanoparticles. *Molecular Pharmaceutics* **6**, 1371-1379 (2009).

50. Wang, Y. et al. Controlled release behaviour of protein-loaded microparticles prepared via coaxial or emulsion electrospray. *Journal of Microencapsulation* **30**, 490-497 (2013).

51. Xie, J.W., Ng, W.J., Lee, L.Y. & Wang, C.H. Encapsulation of protein drugs in biodegradable microparticles by co-axial electrospray. *J Colloid Interf Sci* **317**, 469-476 (2008).

52. Enayati, M., Ahmad, Z., Stride, E. & Edirisinghe, M. One-step electrohydrodynamic production of drug-loaded micro- and nanoparticles. *Journal of the Royal Society Interface* **7**, 667-675 (2010).

53. Guan, Y.P. et al. Preparation of ALA-loaded PLGA nanoparticles and its application in PDT treatment. *Journal of Chemical Technology and Biotechnology* **91**, 1128-1135 (2016).

54. Hao, S.L., Wang, B.C., Wang, Y.Z. & Xu, Y.Q. Enteric-coated sustained-release nanoparticles by coaxial electrospray: preparation, characterization, and in vitro evaluation. *Journal of Nanoparticle Research* **16**, 11 (2014).

55. Yuan, S. et al. Coaxial Electrospray of Curcumin-Loaded Microparticles for Sustained Drug Release. *Plos One* **10** (2015).

56. Cao, Y., Wang, B.C., Wang, Y.Z. & Lou, D.S. Polymer-controlled core-shell nanoparticles: a novel strategy for sequential drug release. *Rsc Advances* **4**, 30430-30439 (2014).

57. Lee, Y.H., Mei, F., Bai, M.Y., Zhao, S. & Chen, D.R. Release profile characteristics of biodegradable-polymer-coated drug particles fabricated by dual-capillary electrospray. *Journal of Controlled Release* **145**, 58-65 (2010).

58. Reardon, P.J.T. et al. Electrohydrodynamic fabrication of core-shell PLGA nanoparticles with controlled release of cisplatin for enhanced cancer treatment. *International Journal of Nanomedicine* **12**, 3913-3926 (2017).

59. Xu, Q.X. et al. Coaxial electrohydrodynamic atomization process for production of polymeric composite microspheres. *Chemical Engineering Science* **104**, 330-346 (2013).

60. Kavadiya, S. & Biswas, P. Electrospray deposition of biomolecules: Applications, challenges, and recommendations. *J Aerosol Sci* **125**, 182-207 (2018).

61. Akita, H. et al. A neutral lipid envelope-type nanoparticle composed of a pH-activated and vitamin E-scaffold lipid-like material as a platform for a gene carrier targeting renal cell carcinoma. *Journal of Controlled Release* **200**, 97-105 (2015).

62. Xu, C.-F., Liu, Y., Shen, S., Zhu, Y.-H. & Wang, J. Targeting glucose uptake with siRNA-based nanomedicine for cancer therapy. *Biomaterials* **51**, 1-11 (2015).

63. Silva, A.K.A. et al. Combining magnetic nanoparticles with cell derived microvesicles for drug loading and targeting. *Nanomedicine: Nanotechnology, Biology and Medicine* **11**, 645-655 (2015).

64. Zhang, Y. et al. Targeted delivery of human VEGF gene via complexes of magnetic nanoparticle-adenoviral vectors enhanced cardiac regeneration. *Plos One* **7**, e39490-e39490 (2012).

65. Bietenbeck, M., Florian, A., Faber, C., Sechtem, U. & Yilmaz, A. Remote magnetic targeting of iron oxide nanoparticles for cardiovascular diagnosis and therapeutic drug delivery: where are we now? *International journal of nanomedicine* **11**, 3191-3203 (2016).

66. Medicine, J.o.G., Vol. 2017 Vectors Used in Gene Therapy Clinical Trials Worldwide (John Wiley and Sons Ltd, 2017).

67. , Vol. 2017 (Journal of Gene Medicine, 2017).

68. Zaiss, A.K. et al. Complement is an essential component of the immune response to adeno-associated virus vectors. *J Virol* **82**, 2727-2740 (2008).

69. Appledorn, D.M. et al. Adenovirus vector-induced innate inflammatory mediators, MAPK signaling, as well as adaptive immune responses are dependent upon both TLR2 and TLR9 in vivo. *J Immunol* **181**, 2134-2144 (2008).

70. Zhu, J., Huang, X. & Yang, Y. Innate immune response to adenoviral vectors is mediated by both Toll-like receptor-dependent and -independent pathways. *J Virol* **81**, 3170-3180 (2007).

71. Mingozzi, F. et al. CD8+ T-cell responses to adeno-associated virus capsid in humans. *Nat Med* **13**, 419 (2007).

72. Gahery-Segard, H. et al. Immune response to recombinant capsid proteins of adenovirus in humans: Antifiber and anti-penton base antibodies have a synergistic effect on neutralizing activity. *J Virol* **72**, 2388-2397 (1998).

73. Zhu, J.G., Huang, X.P. & Yang, Y.P. Type IIFN signaling on both B and CD4 T cells is required for protective antibody response to adenovirus. *J Immunol* **178**, 3505-3510 (2007).

74. Raper, S.E. et al. Fatal systemic inflammatory response syndrome in a ornithine transcarbamylase deficient patient following adenoviral gene transfer. *Mol Genet Metab* **80**, 148-158 (2003).

75. Hacein-Bey-Abina, S. et al. Insertional oncogenesis in 4 patients after retrovirus-mediated gene therapy of SCID-X1. *J Clin Invest* **118**, 3132-3142 (2008).

76. Braun, C.J. et al. Gene Therapy for Wiskott-Aldrich Syndrome-Long-Term Efficacy and Genotoxicity. *Sci Transl Med* **6** (2014).

77. Dicks, M.D.J. et al. The relative magnitude of transgene-specific adaptive immune responses induced by human and chimpanzee adenovirus vectors differs between laboratory animals and a target species. *Vaccine* **33**, 1121-1128 (2015).

78. Manno, C.S. et al. Successful transduction of liver in hemophilia by AAV-Factor IX and limitations imposed by the host immune response. *Nat Med* **12**, 342 (2006).

79. Li, H. et al. Capsid-specific T-cell Responses to Natural Infections With Adeno-associated Viruses in Humans Differ From Those of Nonhuman Primates. *Molecular Therapy* **19**, 2021-2030 (2011).

80. Lundstrom, K. Viral Vectors in Gene Therapy. *Diseases* **6**, 42 (2018).

81. Kawabata, K., Takakura, Y. & Hashida, M. The Fate of Plasmid DNA after Intravenous-Injection in Mice - Involvement of Scavenger Receptors in Its Hepatic-Uptake. *Pharm Res* **12**, 825-830 (1995).

82. Pinyon, J.L. et al. Close-Field Electroporation Gene Delivery Using the Cochlear Implant Electrode Array Enhances the Bionic Ear. *Sci Transl Med* **6** (2014).

83. Gao, D. et al. Ultrasound-Triggered Phase-Transition Cationic Nanodroplets for Enhanced Gene Delivery. *ACS Appl. Mater. Interfaces* **7**, 13524-13537 (2015).

84. Mislick, K.A. & Baldeschwieler, J.D. Evidence for the role of proteoglycans in cation-mediated gene transfer. *P Natl Acad Sci USA* **93**, 12349-12354 (1996).

85. Liao, J.F. et al. Self-Assembly DNA Polyplex Vaccine inside Dissolving Microneedles for High-Potency Intradermal Vaccination. *Theranostics* **7**, 2593-2605 (2017).

86. Uchida, S. et al. Combination of chondroitin sulfate and polyplex micelles from Poly(ethylene glycol)-poly{N '-[N-(2-aminoethyl)-2-aminoethyl]aspartamide} block copolymer for prolonged in vivo gene transfection with reduced toxicity. *Journal of Controlled Release* **155**, 296-302 (2011).

87. Howard, K.A. et al. Formulation of a microparticle carrier for oral polyplex-based DNA vaccines. *Bba-Gen Subjects* **1674**, 149-157 (2004).

88. Zhang, X.F. et al. PEGylated poly(amine-co-ester) micelles as biodegradable non-viral gene vectors with enhanced stability, reduced toxicity and higher in vivo transfection efficacy. *J Mater Chem B* **2**, 4034-4044 (2014).

89. Dhande, Y.K. et al. N-Acetylgalactosamine Block-co-Polycations Form Stable Polyplexes with Plasmids and Promote Liver-Targeted Delivery. *Biomacromolecules* **17**, 830-840 (2016).

90. Ganas, C. et al. Biodegradable capsules as non-viral vectors for in vitro delivery of PEI/siRNA polyplexes for efficient gene silencing. *Journal of Controlled Release* **196**, 132-138 (2014).

91. Li, L.H., Puhl, S., Meinel, L. & Germershaus, O. Silk fibroin layer-by-layer microcapsules for localized gene delivery. *Biomaterials* **35**, 7929-7939 (2014).

92. Bishop, C.J., Tzeng, S.Y. & Green, J.J. Degradable polymer-coated gold nanoparticles for co-delivery of DNA and siRNA. *Acta Biomater* **11**, 393-403 (2015).

93. Arya, N., Chakraborty, S., Dube, N. & Katti, D.S. Electrospraying: A Facile Technique for Synthesis of Chitosan-Based Micro/Nanospheres for Drug Delivery Applications. *J. Biomed. Mater. Res. Part B* **88B**, 17-31 (2009).

94. Esselin, N. et al. Potentialities of the Poly(Aminoethyl Methacrylate) p(AMA) as Gelatin-Like Polymer in Complex Coacervation. **06**, 147-160 (2016).

95. Pavot, V. et al. Encapsulation of Nod1 and Nod2 receptor ligands into poly(lactic acid) nanoparticles potentiates their immune properties. *Journal of Controlled Release* **167**, 60-67 (2013).

96. Saini, V. et al. Humoral and cell-mediated immune-responses after administration of a single-shot recombinant hepatitis B surface antigen vaccine formulated with cationic poly(l-lactide) microspheres. *J Drug Target* **18**, 212-222 (2010).

97. Han, F.Y., Thurecht, K.J., Whittaker, A.K. & Smith, M.T. Bioerodable PLGA-Based Microparticles for Producing Sustained-Release Drug Formulations and Strategies for Improving Drug Loading. *Front Pharmacol* **7** (2016).

98. Freiberg, S. & Zhu, X. Polymer microspheres for controlled drug release. *International Journal of Pharmaceutics* **282**, 1-18 (2004).

99. Liu, H., Slamovich, E.B. & Webster, T.J. Less harmful acidic degradation of poly(lactic-co-glycolic acid) bone tissue engineering scaffolds through titania nanoparticle addition. *International Journal of Nanomedicine* **1**, 541-545 (2006).

100. Sivakumar, S.M. & Sukumaran, N. Induction of Immune Response of Hepatitis B Vaccine Using Polyester Polymer as an Adjuvant. *Vaccine* (2008).

101. Ataman-Onal, Y. et al. Surfactant-free anionic PLA nanoparticles coated with HIV-1 p24 protein induced enhanced cellular and humoral immune responses in various animal models. *Journal of Controlled Release* **112**, 175-185 (2006).

102. Bansal, V., Kumar, M., Dalela, M., Brahmne, H.G. & Singh, H. Evaluation of synergistic effect of biodegradable polymeric nanoparticles and aluminum based adjuvant for improving vaccine efficacy. *International Journal of Pharmaceutics* **471**, 377-384 (2014).

103. Zhang, W.F. et al. Immunopotentiator-Loaded Polymeric Microparticles as Robust Adjuvant to Improve Vaccine Efficacy. *Pharm Res* **32**, 2837-2850 (2015).

104. Zhang, X., Duan, Y.J., Wang, D.F. & Bian, F.L. Preparation of arginine modified PEI-conjugated chitosan copolymer for DNA delivery. *Carbohyd Polym* **122**, 53-59 (2015).

105. Jiang, D.H. & Salem, A.K. Optimized dextran-polyethylenimine conjugates are efficient non-viral vectors with reduced cytotoxicity when used in serum containing environments. *International Journal of Pharmaceutics* **427**, 71-79 (2012).

106. Jokerst, J.V., Lobovkina, T., Zare, R.N. & Gambhir, S.S. Nanoparticle PEGylation for imaging and therapy. *Nanomedicine-Uk* **6**, 715-728 (2011).

107. Qie, Y.Q. et al. Surface modification of nanoparticles enables selective evasion of phagocytic clearance by distinct macrophage phenotypes (vol 6, 26269, 2016). *Sci Rep-Uk* **6** (2016).

108. Davies, L.A. et al. Electrohydrodynamic comminution: A novel technique for the aerosolisation of plasmid DNA. *Pharm Res* **22**, 1294-1304 (2005).

109. Parodi, A. et al. Enabling cytoplasmic delivery and organelle targeting by surface modification of nanocarriers. *Nanomedicine-Uk* **10**, 1923-1940 (2015).

110. Benjaminsen, R.V., Mattebjerg, M.A., Henriksen, J.R., Moghimi, S.M. & Andresen, T.L. The possible "proton sponge " effect of polyethylenimine (PEI) does not include change in lysosomal pH. *Molecular therapy : the journal of the American Society of Gene Therapy* **21**, 149-157 (2013).

111. Li, Z., Mak, S.Y., Sauret, A. & Shum, H.C. Syringe-pump-induced fluctuation in all-aqueous microfluidic system implications for flow rate accuracy. *Lab on a Chip* **14**, 744-749 (2014).

112. Kim, W. & Kim, S.S. Synthesis of biodegradable triple-layered capsules using a triaxial electrospray method. *Polymer* **52**, 3325-3336 (2011).

113. Ghayempour, S. & Mortazavi, S.M. Fabrication of micro-nanocapsules by a new electrospraying method using coaxial jets and examination of effective parameters on their production. *J Electrostat* **71**, 717-727 (2013).

114. Hao, S.L. et al. Formulation of porous poly(lactic-co-glycolic acid) microparticles by electrospray deposition method for controlled drug release. *Materials Science & Engineering C-Materials for Biological Applications* **39**, 113-119 (2014).

115. Zarchi, A.A.K. et al. Development and optimization of N-Acetylcysteine-loaded poly (lactic-co-glycolic acid) nanoparticles by electrospray. *Int. J. Biol. Macromol.* **72**, 764-770 (2015).

116. Shams, T., Parhizkar, M., Illangakoon, U.E., Orlu, M. & Edirisinghe, M. Core/shell microencapsulation of indomethacin/paracetamol by co-axial electrohydrodynamic atomization. *Materials & Design* **136**, 204-213 (2017).

117. Parhizkar, M. et al. Electrohydrodynamic encapsulation of cisplatin in poly (lactic-co-glycolic acid) nanoparticles for controlled drug delivery. *Nanomed-Nanotechnol* **12**, 1919-1929 (2016).

118. Xie, J. & Wang, C.-H. Encapsulation of proteins in biodegradable polymeric microparticles using electrospray in the Taylor Cone-Jet mode. *Biotechnology and Bioengineering* **97**, 1278-1290 (2007).

119. Liu, H. et al. Double-layered hyaluronic acid/stearic acid-modified polyethyleneimine nanoparticles encapsulating (-)-gossypol: a nanocarrier for chiral anticancer drugs. *J Mater Chem B* **2**, 5238-5248 (2014).

120. Gasket, Q.C., Vol. 2018 (http://www.quickcutgasket.com; 2018).

121. Wang, K. in Viscoelasticity - From Theory to Biological Applications. (ed. J.D. Vicente) 77-96 (IntechOpen, 2012).

122. Tang, K.Q. & Gomez, A. Monodisperse electrosprays of low electric conductivity liquids in the cone-jet mode. *J Colloid Interf Sci* **184**, 500-511 (1996).

123. Chen, X.P., Jia, L.B., Yin, X.Z., Cheng, J.S. & Lu, J. Spraying modes in coaxial jet electrospray with outer driving liquid. *Physics of Fluids* **17** (2005).

124. Chang, M.W., Stride, E. & Edirisinghe, M. A New Method for the Preparation of Monoporous Hollow Microspheres. *Langmuir* **26**, 5115-5121 (2010).

125. Sofokleous, P., Lau, W.K., Edirisinghe, M. & Stride, E. The effect of needle tip displacement in co-axial electrohydrodynamic processing. *Rsc Advances* **6**, 75258-75268 (2016).

126. Merck (2019).

127. Merck, Vol. 2019 (Merck; 2019).

128. Merck, Vol. 2019 (2019).

129. Qian, X.M. et al. Star-branched amphiphilic PLA-b-PDMAEMA copolymers for co-delivery of miR-21 inhibitor and doxorubicin to treat glioma. *Biomaterials* **35**, 2322-2335 (2014).

130. Munier, S., I, M., Delair, T., Verrier, B. & Ataman-Onal, Y. Cationic PLA nanoparticles for DNA delivery: Comparison of three surface polycations for DNA binding, protection and transfection properties. *Colloid Surface B* **43**, 163-173 (2005).

131. Guo, S.T. et al. Amphiphilic and biodegradable methoxy polyethylene glycol-block-(polycaprolactone-graft-poly(2-(dimethylamino)ethyl methacrylate)) as an effective gene carrier. *Biomaterials* **32**, 879-889 (2011).

132. Liu, C.K., Dou, Q.Q., Liow, S.S., Kumar, J.N. & Loh, X.J. Cationic Micelles Based on Polyhedral Oligomeric Silsesquioxanes for Enhanced Gene Transfection. *Aust J Chem* **69**, 363-371 (2016).

133. Lin, D.S. et al. Structural contributions of blocked or grafted poly(2-dimethylaminoethyl methacrylate) on PEGylated polycaprolactone nanoparticles in siRNA delivery. *Biomaterials* **32**, 8730-8742 (2011).

134. Zheng, X. et al. Structural impact of graft and block copolymers based on poly(N-vinylpyrrolidone) and poly(2-dimethylaminoethyl methacrylate) in gene delivery. *J Mater Chem B* **3**, 4027-4035 (2015).

135. Cherng, J.Y., vandeWetering, P., Talsma, H., Crommelin, D.J.A. & Hennink, W.E. Effect of size and serum proteins on transfection efficiency of poly((2-dimethylamino)ethyl methacrylate)-plasmid nanoparticles. *Pharm Res* **13**, 1038-1042 (1996).

136. Loh, X.J., Ong, S.J., Tung, Y.T. & Choo, H.T. Co-delivery of drug and DNA from cationic dual-responsive micelles derived from poly(DMAEMA-co-PPGMA). *Materials Science & Engineering C-Materials for Biological Applications* **33**, 4545-4550 (2013).

137. Isik, T., Demir, M.M., Aydogan, C., Ciftci, M. & Yagci, Y. Hydrophobic Coatings from Photochemically Prepared Hydrophilic Polymethacrylates via Electrospraying. *J Polym Sci Pol Chem* **55**, 1338-1344 (2017).

138. Vert, M., Li, S.M., Spenlehauer, G. & Guerin, P. Bioresorbability and Biocompatibility of Aliphatic Polyesters. *J Mater Sci-Mater M* **3**, 432-446 (1992).

139. Okamoto, M. & John, B. Synthetic biopolymer nanocomposites for tissue engineering scaffolds. *Prog Polym Sci* **38**, 1487-1503 (2013).

140. Lu, J., Hou, R., Yang, Z.L. & Tang, Z.H. Development and characterization of drug-loaded biodegradable PLA microcarriers prepared by the electrospraying technique. *Int J Mol Med* **36**, 249-254 (2015).

141. Xu, Y.X. & Hanna, M.A. Morphological and structural properties of two-phase coaxial jet electrosprayed BSA-PLA capsules. *Journal of Microencapsulation* **25**, 469-477 (2008).

142. Li, J.L. & Tok, A. Electrospraying of water in the cone-jet mode in air at atmospheric pressure. *Int J Mass Spectrom* **272**, 199-203 (2008).

143. Yao, S.L. et al. Drug-nanoencapsulated PLGA microspheres prepared by emulsion electrospray with controlled release behavior. *Regen Biomater* **3**, 309-317 (2016).

144. Yu, J.H., Fridrikh, S.V. & Rutledge, G.C. Production of Submicrometer Diameter Fibers by Two-Fluid Electrospinning. *Adv Mater* **16**, 1562-1566 (2004).

145. Misra, N.N., Sullivan, C. & Cullen, P.J. Process Analytical Technology (PAT) and Multivariate Methods for Downstream Processes. *Current Biochemical Engineering* **2**, 4-16 (2015).

146. Delvallée, A., Feltin, N., Ducourtieux, S., Trabelsi, M. & Hochepied, J.-F. Comparison of nanoparticle diameter measurements by Atomic Force Microscopy and Scanning Electron Microscopy. *International Congress of Metrology*, 06007 (2013).

147. Yang, D.Q., Xiong, Y.Q., Guo, Y., Da, D.A. & Lu, W.G. Sizes correction on AFM images of nanometer spherical particles. *J Mater Sci* **36**, 263-267 (2001).

148. Ali, M., Vol. Comparative Study on Structural and some Physical Properties of ZnO Thin Films Prepared by Pulsed Laser Deposition (PLD) (Suez University, 2015).

149. Bai, J., Beyer, S., Yein, T.S. & Trau, D. Self-Assembly of Polyamines as a Facile Approach to Fabricate Permeability Tunable Polymeric Shells for Biomolecular Encapsulation. *ACS Appl. Mater. Interfaces* **3**, 1665-1674 (2011).

150. Cai, T. et al. Effect of hydrolysis degree of hydrolyzed polyacrylamide grafted carboxymethyl cellulose on dye removal efficiency. *Cellulose* **20**, 2605-2614 (2013).

151. Duhoranimana, E. et al. Effect of sodium carboxymethyl cellulose on complex coacervates formation with gelatin: Coacervates characterization, stabilization and formation mechanism. *Food Hydrocolloid* **69**, 111-120 (2017).

152. Chen, N., Tong, Z., Yang, W. & Brennan, A.B. Biocomposites with tunable properties from poly(lactic acid)-based copolymers and carboxymethyl cellulose via ionic assembly. *Carbohyd Polym* **128**, 122-129 (2015).

153. Krishnamoorthy, M. et al. Solution Conformation of Polymer Brushes Determines Their Interactions with DNA and Transfection Efficiency. *Biomacromolecules* **18**, 4121-4132 (2017).

154. Tangeysh, B., Fryd, M., Ilies, M.A. & Wayland, B.B. Palladium metal nanoparticle size control through ion paired structures of [PdCl4](2-) with protonated PDMAEMA. *Chem Commun* **48**, 8955-8957 (2012).

155. Niskanen, J. et al. Thermoresponsiveness of PDMAEMA. Electrostatic and Stereochemical Effects. *Macromolecules* **46**, 2331-2340 (2013).

156. Xing, R.M. et al. Superparamagnetic magnetite nanocrystal clusters as potential magnetic carriers for the delivery of platinum anticancer drugs. *J Mater Chem* **21**, 11142-11149 (2011).

157. Nadagouda, M.N. & Varma, R.S. Synthesis of thermally stable carboxymethyl cellulose/metal biodegradable nanocomposites for potential biological applications. *Biomacromolecules* **8**, 2762-2767 (2007).

158. Lin, X.Y. et al. Synthesis, characterization and electrospinning of new thermoplastic carboxymethyl cellulose (TCMC). *Chem Eng J* **215**, 709-720 (2013).

159. Kalliola, S. et al. The pH sensitive properties of carboxymethyl chitosan nanoparticles cross-linked with calcium ions. *Colloid Surface B* **153**, 229-236 (2017).

160. Li, Y., Zeng, Q., Gentle, I.R. & Wang, D.W. Carboxymethyl cellulose binders enable high-rate capability of sulfurized polyacrylonitrile cathodes for Li-S batteries. *J Mater Chem A* **5**, 5460-5465 (2017).

161. Wu C, S.S., Varshney D, Shalaev E in Lyophilized Biologics and Vaccines (Springer, 2015).

162. Mao, J., Ji, X.L. & Bo, S.Q. Synthesis and pH/Temperature-Responsive Behavior of PLLA-b-PDMAEMA Block Polyelectrolytes Prepared via ROP and ATRP. *Macromol Chem Phys* **212**, 744-752 (2011).

163. Bonkovoski, L.C. et al. Polyelectrolyte complexes of poly[(2-dimethylamino) ethyl methacrylate]/chondroitin sulfate obtained at different pHs: I. Preparation, characterization, cytotoxicity and controlled release of chondroitin sulfate. *International Journal of Pharmaceutics* **477**, 197-207 (2014).

164. Yu, H.P., Fu, Y.C., Li, G. & Liu, Y.X. Antimicrobial surfaces of quaternized poly[(2-dimethyl amino)ethyl methacrylate] grafted on wood via ARGET ATRP. *Holzforschung* **67**, 455-461 (2013).

165. Coblentz Society, I. (National Institute of Standards and Technology, NIST Chemistry WebBook.

166. Coblentz Society, I. (National Institute of Standards and Technology, NIST Chemistry WebBook.

167. Coblentz Society, I. (National Institute of Standards and Technology, NIST Chemistry WebBook.

168. Mumper, R.J. & Jay, M. Poly(L-lactic Acid) Microspheres Containing Neutron-Activatable Holmium-165: A Study of the Physical Characteristics of Microspheres Before and After Irradiation in a Nuclear Reactor. *Pharm Res* **9**, 149-154 (1992).

169. Koegler, W.S., Patrick, C., Cima, M.J. & Griffith, L.G. Carbon dioxide extraction of residual chloroform from biodegradable polymers. *J Biomed Mater Res* **63**, 567-576 (2002).

170. Zielhuis, S.W. et al. Removal of chloroform from biodegradable therapeutic microspheres by radiolysis. *International Journal of Pharmaceutics* **315**, 67-74 (2006).

171. Silva, J.M. et al. pH Responsiveness of Multilayered Films and Membranes Made of Polysaccharides. *Langmuir* **31**, 11318-11328 (2015).

172. Thompson, M.T., Berg, M.C., Tobias, I.S., Rubner, M.F. & Van Vliet, K.J. Tuning compliance of nanoscale polyelectrolyte multilayers to modulate cell adhesion. *Biomaterials* **26**, 6836-6845 (2005).

173. Han, U., Seo, Y. & Hong, J. Effect of pH on the structure and drug release profiles of layer-by-layer assembled films containing polyelectrolyte, micelles, and graphene oxide. *Sci Rep* **6**, 24158 (2016).

174. Bhattacharyya, R. & Ray, S.K. Kinetic and Equilibrium Modeling for Adsorption of Textile Dyes in Aqueous Solutions by Carboxymethyl Cellulose/Poly(acrylamide-co-hydroxyethy methacrylate) Semi-interpenetrating Network Hydrogel. *Polym Eng Sci* **53**, 2439-2453 (2013).

175. Cerchiara, T. et al. Microparticles based on chitosan/carboxymethylcellulose polyelectrolyte complexes for colon delivery of vancomycin. *Carbohyd Polym* **143**, 124-130 (2016).

176. Akar, E., Altinisik, A. & Seki, Y. Preparation of pH- and ionic-strength responsive biodegradable fumaric acid crosslinked carboxymethyl cellulose. *Carbohyd Polym* **90**, 1634-1641 (2012).

177. Lohani, A., Singh, G., Bhattacharya, S.S., Hegde, R.R. & Verma, A. Tailored-interpenetrating polymer network beads of kappa-carrageenan and sodium carboxymethyl cellulose for controlled drug delivery. *J Drug Deliv Sci Tec* **31**, 53-64 (2016).

178. van de Wetering, P. et al. A Mechanistic Study of the Hydrolytic Stability of Poly(2-(dimethylamino)ethyl methacrylate). *Macromolecules* **31**, 8063-8068 (1998).

179. Bütün, V., Armes, S.P. & Billingham, N.C. Synthesis and aqueous solution properties of near-monodisperse tertiary amine methacrylate homopolymers and diblock copolymers. *Polymer* **42**, 5993-6008 (2001).

180. Lin, S. et al. An Acid-Labile Block Copolymer of PDMAEMA and PEG as Potential Carrier for Intelligent Gene Delivery Systems. *Biomacromolecules* **9**, 109-115 (2008).

181. Rungsardthong, U. et al. Effect of Polymer Ionization on the Interaction with DNA in Nonviral Gene Delivery Systems. *Biomacromolecules* **4**, 683-690 (2003).

182. Yetgin, S. & Balkose, D. Calf thymus DNA characterization and its adsorption on different silica surfaces. *RSC Advances* **5**, 57950-57959 (2015).

183. Lo, C.-W., Chang, Y., Lee, J.-L., Tsai, W.-B. & Chen, W.-S. Tertiary-Amine Functionalized Polyplexes Enhanced Cellular Uptake and Prolonged Gene Expression. *Plos One* **9**, e97627 (2014).

184. Pippa, N., Karayianni, M., Pispas, S. & Demetzos, C. Complexation of cationic-neutral block polyelectrolyte with insulin and in vitro release studies. *International Journal of Pharmaceutics* **491**, 136-143 (2015).

185. Pispas, S. Complexes of lysozyme with sodium (sulfamate-carboxylate)isoprene/ethylene oxide double hydrophilic block copolymers. *Journal of Polymer Science Part A: Polymer Chemistry* **45**, 509-520 (2007).

186. Babikova, D. et al. Functional block copolymer nanocarriers for anticancer drug delivery. *Rsc Advances* **6**, 84634-84644 (2016).

187. Liao, Y.H., Jones, S.A., Forbes, B., Martin, G.P. & Brown, M.B. Hyaluronan: Pharmaceutical characterization and drug delivery. *Drug Deliv* **12**, 327-342 (2005).

188. Fink, T.L. et al. Plasmid size up to 20 kbp does not limit effective in vivo lung gene transfer using compacted DNA nanoparticles. *Gene Ther* **13**, 1048-1051 (2006).

189. Mofokeng, J.P., Luyt, A.S., Tábi, T. & Kovács, J. Comparison of injection moulded, natural fibre-reinforced composites with PP and PLA as matrices. *Journal of Thermoplastic Composite Materials* **25**, 927-948 (2011).

190. Chieng, B.W., Ibrahim, N.A., Then, Y.Y. & Loo, Y.Y. Epoxidized Vegetable Oils Plasticized Poly(lactic acid) Biocomposites: Mechanical, Thermal and Morphology Properties. *Molecules* **19**, 16024-16038 (2014).

191. Katiyar, V. & Nanavati, H. Ring-opening polymerization of L-lactide using N-heterocyclic molecules: mechanistic, kinetics and DFT studies. *Polym Chem-Uk* **1**, 1491-1500 (2010).

192. Zhu, L.-J., Liu, F., Yu, X.-M., Gao, A.-L. & Xue, L.-X. Surface zwitterionization of hemocompatible poly(lactic acid) membranes for hemodiafiltration. *J Membrane Sci* **475**, 469-479 (2015).

193. Christie, R.J., Nishiyama, N. & Kataoka, K. Minireview: Delivering the Code: Polyplex Carriers for Deoxyribonucleic Acid and Ribonucleic Acid Interference Therapies. *Endocrinology* **151**, 466-473 (2010).

194. Ghasemi, S., Behrooz, R. & Ghasemi, I. Investigating the properties of maleated poly(lactic acid) and its effect on poly(lactic acid)/cellulose nanofiber composites. *J Polym Eng* **38**, 391-398 (2018).

195. Eyal, A.M. & Canari, R. pH Dependence of Carboxylic and Mineral Acid Extraction by Amine-Based Extractants: Effects of pKa, Amine Basicity, and Diluent Properties. *Ind Eng Chem Res* **34**, 1789-1798 (1995).

196. Chaiwong, C., Rachtanapun, P., Wongchaiya, P., Auras, R. & Boonyawan, D. Effect of plasma treatment on hydrophobicity and barrier property of polylactic acid. *Surf Coat Tech* **204**, 2933-2939 (2010).

197. Lee, S.H. & Yeo, S.Y. Improvement of Hydrophilicity of Polylactic Acid (PLA) Fabrics by Means of a Proteolytic Enzyme from Bacillus licheniformis. *Fiber Polym* **17**, 1154-1161 (2016).

198. Proikakis, C.S., Mamouzelos, N.J., Tarantili, P.A. & Andreopoulos, A.G. Swelling and hydrolytic degradation of poly(D,L-lactic acid) in aqueous solutions. *Polym Degrad Stabil* **91**, 614-619 (2006).

199. Barbucci, R., Magnani, A. & Consumi, M. Swelling behavior of carboxymethylcellulose hydrogels in relation to cross-linking, pH, and charge density. *Macromolecules* **33**, 7475-7480 (2000).

200. Festag, R. et al. Effects of molecular entanglements during electrospray of high molecular weight polymers. *J Am Soc Mass Spectr* **9**, 299-304 (1998).

201. Hanton, S.D. et al. Investigations of electrospray sample deposition for polymer MALDI mass spectrometry. *J Am Soc Mass Spectr* **15**, 168-179 (2004).

202. Guo, H.L. et al. A GO@PLA@ HA Composite Microcapsule: Its Preparation and Multistage and Controlled Drug Release. *Eur J Inorg Chem*, 3312-3321 (2017).

203. Zheng, S.S. et al. Evaluation of optimum conditions for pachyman encapsulated in poly(D,L-lactic acid) nanospheres by response surface

methodology and results of a related in vitro study. *International Journal of Nanomedicine* **11**, 4891-4904 (2016).

204. Fischer, R.L., McCoy, M.G. & Grant, S.A. Electrospinning collagen and hyaluronic acid nanofiber meshes. *J Mater Sci-Mater M* **23**, 1645-1654 (2012).

205. Jiang, B.P. et al. Water-soluble hyaluronic acid-hybridized polyaniline nanoparticles for effectively targeted photothermal therapy. *J Mater Chem B* **3**, 3767-3776 (2015).

206. Gilli, R., Kacurakova, M., Mathlouthi, M., Navarini, L. & Paoletti, S. Ftir Studies of Sodium Hyaluronate and Its Oligomers in the Amorphous Solid-Phase and in Aqueous-Solution. *Carbohyd Res* **263**, 315-326 (1994).

207. Burgess, I., Seivewright, B. & Lennox, R.B. Electric Field Driven Protonation/Deprotonation of Self-Assembled Monolayers of Acid-Terminated Thiols. *Langmuir* **22**, 4420-4428 (2006).

208. Stoodley, P., deBeer, D. & LappinScott, H.M. Influence of electric fields and pH on biofilm structure as related to the bioelectric effect. *Antimicrob Agents Ch* **41**, 1876-1879 (1997).

209. Sugihara, K., Shimazu, K. & Uosaki, K. Electrode Potential Effect on the Surface pKa of a Self-Assembled 15-Mercaptohexadecanoic Acid Monolayer on a Gold/Quartz Crystal Microbalance Electrode. *Langmuir* **16**, 7101-7105 (2000).

210. Gasperini, A.A.M. et al. Association between Cationic Liposomes and Low Molecular Weight Hyaluronic Acid. *Langmuir* **31**, 3308-3317 (2015).

211. Kim, J.-T., Lee, D.-Y., Kim, Y.-H., Lee, I.-K. & Song, Y.-S. Effect of pH on Swelling Property of Hyaluronic Acid Hydrogels for Smart Drug Delivery Systems. *Journal of Sensor Science and Technology* **21**, 256-262 (2012).

212. Liu, P.F., Zhai, M.L., Li, J.Q., Peng, J. & Wu, J.L. Radiation preparation and swelling behavior of sodium carboxymethyl cellulose hydrogels. *Radiat Phys Chem* **63**, 525-528 (2002).

213. Ding, L., Lee, T. & Wang, C.-H. Fabrication of monodispersed Taxol-loaded particles using electrohydrodynamic atomization. *Journal of Controlled Release* **102**, 395-413 (2005).

214. Gao, Y., Zhao, D., Chang, M.W., Ahmad, Z. & Li, J.S. Optimising the shell thickness-to-radius ratio for the fabrication of oil-encapsulated polymeric microspheres. *Chem Eng J* **284**, 963-971 (2016).

215. Basta, A.H., El-Saied, H., Hasanin, M.S. & El-Deftar, M.M. Green carboxymethyl cellulose-silver complex versus cellulose origins in biological activity applications. *Int J Biol Macromol* **107**, 1364-1372 (2018).